In situ observations of reaction and transport phenomena during silicate glass corrosion by fluid-cell Raman spectroscopy

Method development and applications

Dissertation

zur

Erlangung des Doktorgrades (Dr. rer. nat.)

der

Mathematisch-Naturwissenschaftlichen Fakultät

der

Rheinischen Friedrich-Wilhelms-Universität Bonn

vorgelegt von

Lars Dohmen

aus

Duisburg

Bonn 2019

Angefertigt mit Genehmigung der
Mathematisch-Naturwissenschaftlichen Fakultät der Rheinischen
Friedrich-Wilhelms-Universität Bonn

1. Gutachter: **Prof. Dr. Thorsten Geisler-Wierwille**
2. Gutachter: **Prof. Dr. Rudy Konings**

Tag der Promotion: **05.03.2020**

Erscheinungsjahr: **2020**

Abstract

Borosilicate glass is the preferred material for the immobilization of high-level nuclear waste and an important material for various industries. Silicate glasses, however, are prone to corrosion by aqueous solutions, which is reflected by the formation of surface alteration layers (SALs) that are assumed to represent a chemically leached, restructured residual glass. However, there are several inconsistencies with this interpretation such as, for instance, (i) the observation of an atomically sharp interface between the SAL and the underlying glass or (ii) the formation of structural and chemical patterns in the SAL, which both cannot be explained by a diffusion-controlled corrosion mechanism. Experimentally, glass-water reactions are typically investigated under controlled experimental conditions in reaction vessels and by the subsequent, post mortem analysis of (i) the experimental solution after quenching it to room temperature and/or (ii) the solid reaction products after quenching, drying, and mechanical sectioning. Quenching is a crucial shortcoming of such a *post mortem* experimental procedure, since the main corrosion product of silicate glasses is a hydrous amorphous silica gel that undergoes significant chemical and structural changes such as condensation/ polymerization, water loss, and/or cracking during cooling and subsequent drying. Moreover, new samples have to be used for each T-t step and quench phases that may not necessarily be involved in the actual reaction are not easily recognized from *post mortem* analyses. As a matter of fact, a missing component of our current experimental and analytical strategies is the investigation of glass-water reactions at the microscopic to molecular level without disturbing or interrupting them.

In this work, novel confocal hyperspectral Raman experiments to *in situ* study the reaction between two different borosilicate borosilicate glass and alkaline aqueous solutions at 90 °C were performed. Methods are developed to determine the local pH in situ, i.e., space-resolved at the micrometer scale, as well as the local temperature (for experiments in 0.5 M $NaHCO_3$ solution). At the beginning of the reaction, a thin boundary layer at the surface of the glass with higher pH values relative to the bulk solution was observed in several experiments. At this stage the glass dissolved congruently. After the formation of an SAL, an even higher pH within a water-rich interfacial solution located between the SAL and the underlying glass was found. A sudden drop of the reaction rate was observed after the SAL thickness had reached 30 µm. By exchanging the solution with a deuterated bicarbonate solution, the transport of D_2O/OD could be followed through the SAL and it was observed that water transport to and from the interfacial solution was not rate-limiting. The obtained *in situ* data supports an interface-coupled dissolution-reprecipitation model for the formation of the SAL and casts doubts on the validity of published kinetic glass corrosion models.

Contents

CHAPTER 1

Introduction

The stability of silicate glasses in aqueous solution is of enormous importance in many technical applications and subject to scientific research for over a hundred and fifty years (Brewster, 1863; Fowler, 1880). In many countries (e.g., USA, France, United Kingdom, Belgium, and Germany), high level radioactive waste is currently immobilized in borosilicate glass matrices, awaiting permanent storage in a nuclear repository. By 2005 about 9,200 tons of this glass was manufactured worldwide, which enclosed in a multibarrier system, must ensure the retention of radionuclides over a period of 1 million years (Grambow, 2006). After this period of time the radiation of High Level nuclear Waste (HLW) is on the same level as the earth's background radiation and thus not dangerous to mankind anymore. This time span is not accessible by experiments therefore scientist have extrapolate from short term studies or use the observations made on naturally corroded glasses (Macquet and Thomassin, 1992). Due to the system's complexity, taking into account corrosion of the container consist of steel and concrete, as well as the host rock interacting with the corroding solution it remains highly questionable if such an extrapolation can be made. Borosilicate glass is also used for pharmaceutical packaging (e.g. Valor™ from Corning Inc. and FIOLAX® from SCHOTT AG). The vials filled with parenterals sometimes show, after storage for 1-2 years, a phenomenon called delamination (Rupertus et al., 2014). In this case, the glass is attacked by corrosion and nanometer-thick flakes of the detached corrosion product can be visually perceived in the solution.

When a glass comes into contact with water many processes are taking place. Starting with a penetration of protons into the glass structure, breaking of siloxane bonds (Si−O−Si) and the enrichment of the solution with glass components. The most striking feature is the emergence of a Surface Alteration Layer (SAL), which can have a thickness ranging between a few nanometers (Hellmann et al., 2015; Gin et al., 2016) to several millimeters (Verney-Carron et al., 2008; Schalm and Anaf, 2016). Almost over the last century scientist have gone to great lengths to understand the mechanism of the SAL formation and with it the glass corrosion itself. Especially in the light of nuclear waste management a pressing need for proper

modeling arose to predict the glasses performance. A passionate debate evolved in the last few years concentrating on two substantially different models for the corrosion mechanism. Widely accepted is a model based on orthosilicic acid (H_4SiO_4) affinity in solution and a process called interdiffusion (Grambow and Müller, 2001; Frugier et al., 2008; Gin et al., 2016). However, there are several inconsistencies with this model, for example the observation of intriguing pattern formed in the SAL, observed in naturally corroded glasses as well as in experiment (Figure 1.1).

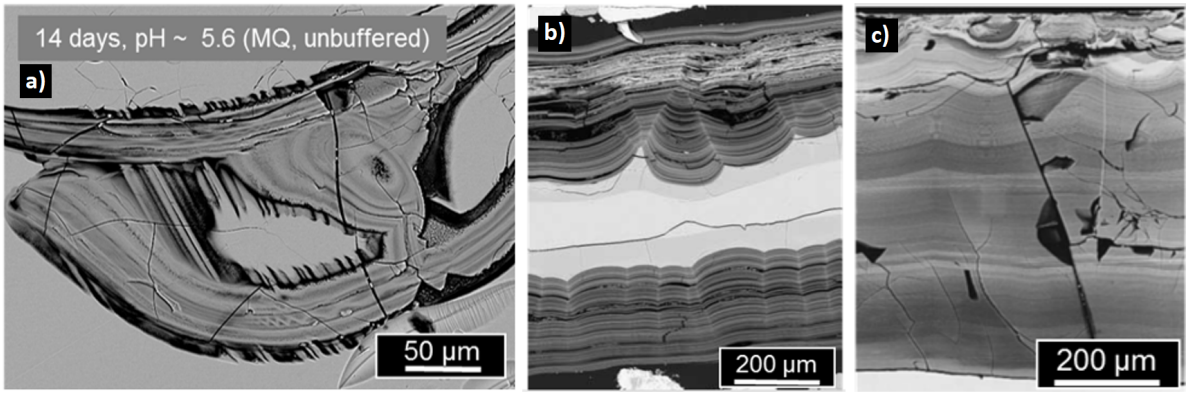

Fig. 1.1.: Generic backscattered electron images of silicate glasses patterned SALs in experiment **(a)** Dohmen et al. (2013) and nature, e.g. **(b)**, Silvestri et al. (2005) and **(c)** Sterpenich and Libourel (2001).

Such a non-linear phenomenon cannot be explained with diffusion controlled process on which the model is based on. The other mechanistic model is proposed by Geisler et al. (2010) and later on by Hellmann et al. (2012) and is transferred from the mechanism controlling the pseudomorphic replacement of minerals by a new mineral in aqueous solution proposed by Putnis (2002). Within this model framework, the glass is replaced by amorphous silica whereby the process of congruent, i.e. stoichiometric, dissolution of the glass and the precipitation of the amorphous silica is coupled in space and time and bound to an interfacial fluid, that moves into the glass. A detailed overview of both models will be given in Section 1.3.

Semantic pitfalls or information lost in translation are a common problem, as many publications are written by non native speakers. To avoid misunderstanding, a glossary for the key-terms used in this work can be found in Section 1.1.

A tremendous challenge glass scientist are facing, is to develop proper *in situ* techniques. Our knowledge about glass corrosion zones is almost exclusively limited to the dried reaction product and the quenched solution, which gives rise to a lot of questions. For example, amorphous silica is strongly influenced by the drying process. It undergoes changes regarding water content, structure and porosity (Iler, 1979). Thus, results of *post mortem* analytical techniques most likely do not reflect the corrosion zone structure during the experiment. Furthermore, conclusions are frequently drawn by analyzing exclusively the solution. At least, solution analysis can be partly conducted *in situ* by the use of Raman spectroscopy. Parruzot et al. (2018),

for instance, recently ran experiments with boron containing glasses. The authors build a reaction cell with a grommet, making it possible to place a fiber in the bulk solution. With a comprehensive calibration it was possible to develop a chemometric model for measuring the boron concentration and the pH of the bulk solution.

Lenting (2018) was the first who conducted a novel kind of *in situ* Raman experiment. In this setup the sample acted as the fluid-cell lid. A polished glass coupon was used with a drilled blind hole in it, leaving a cover of 200 µm thickness. The corrosion was then observed with confocal Raman spectroscopy by measuring through the thin glass cover at the side wall of the blind hole (Figure 1.2).

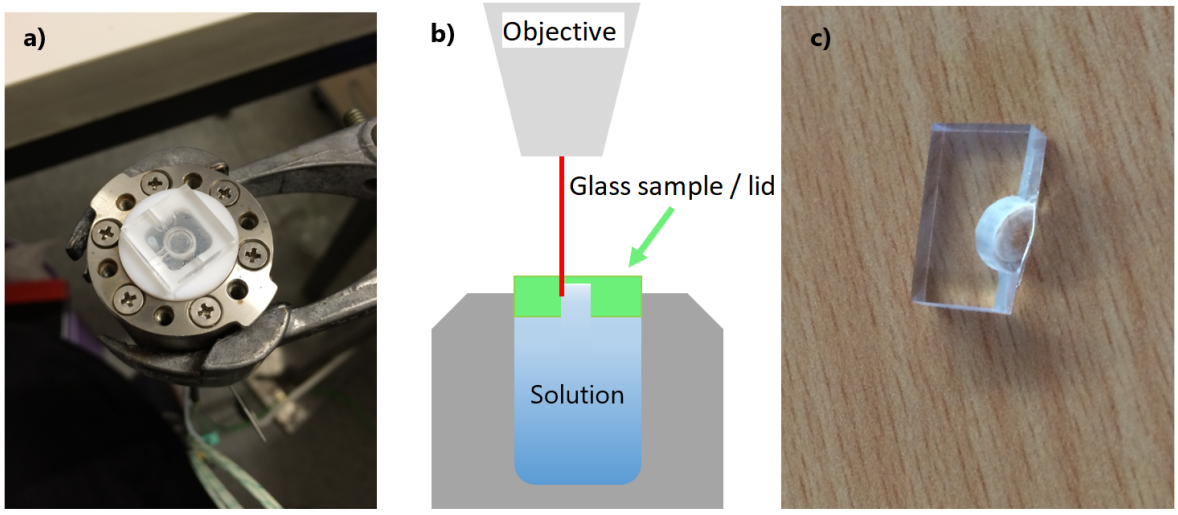

Fig. 1.2.: Fluid-cell setup used by Lenting (2018) where the sample is a glass monolith with a blind hole functioning as the cell's lid at the same time. **(a)**, fluid-cell with sample. **(b)**, sketch of the fluid-cell setup. The measurement position is located on the blind hole's walling. **(c)**, broken sample with the thin coverage of the blind hole visible.

The scope of this work is to further develop the *in situ* Raman method, to evaluate its limitations, and to explore the possible applications. After introducing a glossary of glass corrosion terminology and an introduction to current mechanistic models for glass corrosion the objectives of this work are defined. Eleven *in situ* experiments were conducted and seven are reported in detail. In the methods section a detailed overview is presented about how fluid-cells were designed and constructed as well as about considerations regarding the resolution of the method. After the result section a discussion about the implications of fluid-cell Raman spectroscopy for the study of the corrosion mechanism of simple and more complex borosilicate glasses is given. At last conclusions will be drawn about the potential of *in situ* confocal Raman spectroscopy to investigate the current enigmas of glass corrosion.

1.1. Glossary

In the realm of glass corrosion research with numerous publications written by many non-native speakers it is of crucial importance to be aware of semantic pitfalls. A striking example is the designation of the phase the surface alteration layer is build up. Most authors (Grambow and Müller, 2001; Frugier et al., 2008; Gin et al., 2013b) refer to it as a silica gel and construed it as the outermost region of the glass, where ion exchange took place (e.g. $Na^+ \longleftrightarrow H^+$) followed by *in situ* restructuring of the glass structure that is depleted in network modifiers and some formers such as boron. In an interface coupled dissolution precipitation process it is assumed that a fresh phase precipitates on the glass surface, which is an amorphous network build up by Si bonded to another Si over a bridging oxide or to hydroxyl groups (OH). The chemical term for a silicon atom connected to four hydroxyl groups is orthosilicic acid. If these molecules polymerize in aqueous solution by water release, the condensed phase is called silica gel is considered. Thus, the term can misconceived if the formation of the silica gel is subconsciously included. To avoid this a glossary is given below with terms used in this work and the explanation of their meaning.

Silica gel/ Silica / Amorphous Silica: From solution condensed amorphous SiO_2. It precipitates by agglomeration and polymerization of orthosilicic acid under the release of H_2O.

SAL (Surface Alteration Layer): The amorphous zone of the glass which has changed in any aspect compared to the pristine glass (e.g., structurally or chemically) and which is mainly composed of amorphous SiO_2. Excluded are precipitated crystalline phases on the solution facing surface of the SAL.

Pattern formation: A self organization phenomenon in the SAL. It is divided in multiple lamellae which can differ in pore size or chemical composition (cf. Dohmen et al. 2013).

Secondary phases: All crystalline phases precipitated on the outermost region of the SAL in contact with the solution.

Corrosion zone: The SAL and secondary phases together.

Congruent dissolution: All glass constituents will be found in the solution in the same ratio as they are present in the glass.

ICDP (Interface-Coupled Dissolution Precipitation): A mechanistic model for glass corro-

sion with the hypothesis that the glass dissolves congruently and amorphous silica precipitates at the glass surface. The process is coupled in space and time and thermodynamically driven by the solubility difference between the glass and the amorphous silica. The model was first proposed for glasses by Geisler et al. (2010) and Hellmann et al. (2012) and follows the motion of such a process that has been proposed by Putnis (2002) for mineral replacement reaction.

Interfacial fluid: Water-rich zone (saline solution / suspension) between the SAL and the pristine glass within the framework of an ICDP-process.

Fluid boundary layer: A region within the aqueous solution that is in contact with the glass or the SAL. The pH or ion concentration in this zone may differ significantly compared to the bulk solution.

Interdiffusion (ID) process: Ion exchange between the network modifiers of the glass and protons from the solution that is coupled to simultaneous structural changes.

Depleted gel: An alteration zone that is depleted in network modifiers after a reactive inter-diffusion process has operated, i.e. after the leached zone has recondensed and restructured residual glass skeleton. It is supposed to be a residual glass.

Leaching model: A mechanistic model for glass corrosion based on the work of Grambow and Strachan (1987) and Gin et al. (2016). The underlying hypothesis is that the glass alters by a reactive interdiffusion process leaving behind a depleted zone in the glass that eventually restructures in the solid state forming the SAL.

1.2. Key-observations

To come up with a comprehensive mechanistic model for glass corrosion all observations from experiment and nature should be explainable with it. This section gives a summary of the key-observations made so far.

1.2.1. Patterns

In the most cases naturally corroded glasses have rested either in the ocean, a river, or were weathered in soil, which makes it impossible to probe the solution. Thus, investigating the dried corrosion zones is the only way to make it accessible to scientist. Usually, the samples are examined using electron microscopy and related methods. A frequently observed phenomenon is the formation of patterns in the corrosion zones (Fowler, 1880; Newton, 1971; Macquet and

Thomassin, 1992; Cox and Ford, 1993; Longinelli et al., 2004; Silvestri et al., 2005; Prochazka, 2007; Genga et al., 2008; Sterpenich, 2008; Anaf, 2010; Barbera et al., 2012; Abd-Allah, 2013; Lombardo et al., 2013). The observed pattern can be chemical (cf. Figure 1.3a), structural (cf. Figure 1.3b) or both. If an explanation for the pattern origin is given, most authors attribute the layered SAL to extrinsic changes during corrosion, like periodic changes in pH or temperature. In contrast, Dohmen et al. (2013) considered a self-organizing phenomenon during the SAL formation as the pattern often is observed in experiments that run under static conditions (Anaf, 2010; Geisler et al., 2010). The authors argue that a diffusion-controlled process is not capable to explain pattern formation, whereas it can be modelled based on an ICDP process (Wang et al., 2016).

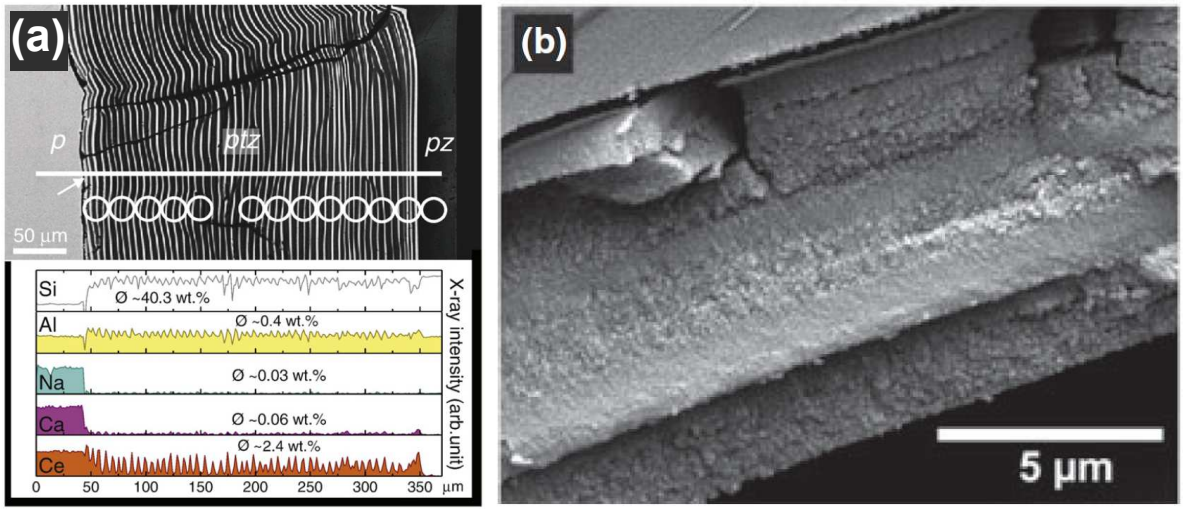

Fig. 1.3.: Chemical and structural pattern, backscattered electrons (BSE) images. **(a)**, pattern observed by Geisler et al. (2010). The chemical pattern is visible in the inset plot. **(b)**, structural pattern observed by Dohmen et al. (2013). The separation of the distinct layers in a patterned zone by spherule/pore size is clearly visible.

1.2.2. Kinetics

Another crucial factor for the application of glasses in various industries are the corrosion rates over time. Three major kinetic regimes for glass corrosion are identified by mainly measuring the soluble glass constituents concentration in solution from which the amount of glass lost per unit of time is calculated. The kinetic regimes are displayed in Figure 1.4. In the first stage, the glass dissolves with the initial reaction rate r_0 representing the forward dissolution rate of the glass. After a certain amount of time, depending on parameters like pH value, temperature, and chemical composition of the glass, a drop in the corrosion rate by several orders of magnitude is observed, running into a comparatively slow residual rate r_r. In some experiments a resumption of the rate is observed (r_2). The reason for that is poorly understood, but may be triggered by precipitation of secondary phases (e.g. zeolites

(Mercado-Depierre et al., 2017)). In Figure 1.4 the evolution of the rate with time is shown. These rate regimes are observed for many glasses, regardless of their chemical composition (Frugier et al., 2005; Utton et al., 2013). In the first stage, the glass dissolves with the initial rate r_0. After a certain amount of time, dependent on the experimental parameter like pH value, temperature and chemical composition of the glass a drop in the corrosion rate by several orders of magnitude is observed, running into the comparatively slow residual rate r_r. In some experiments a resumption of the rate is observed (r_2), which is poorly understood. DIN and ISO norm tests to asses the resistance of glasses in aqueous solution are conducted with glass powders. All these tests do not consider the formation of SALs only forward rates are assumed.

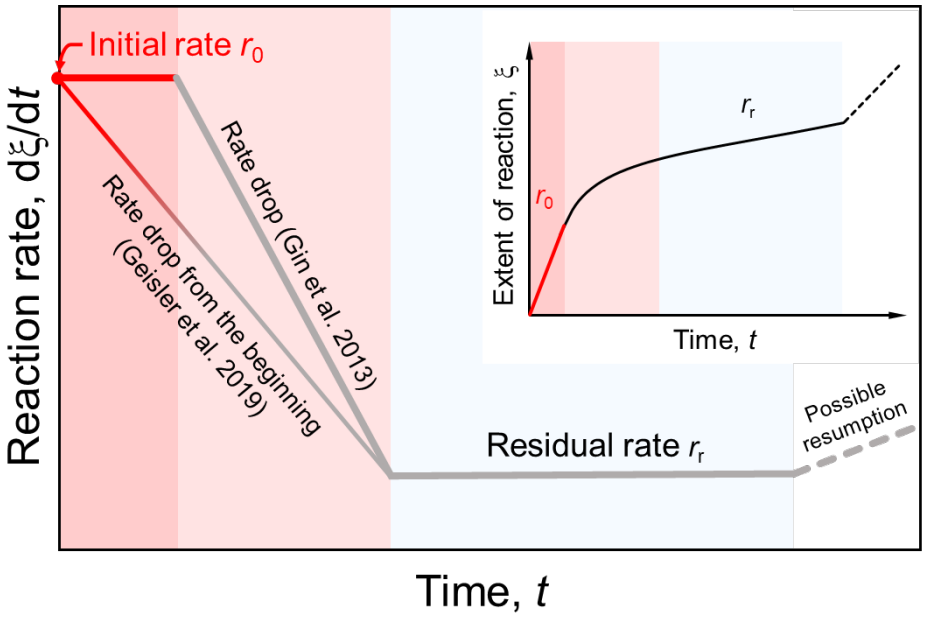

Fig. 1.4.: Rate regimes during glass corrosion modified after Frugier et al. (2008). The first stage of glass corrosion is the initial fast rate, the forward rate r_0 (red). After a certain amount of the rate drops by several order of magnitude (orange). From here on the glass corrosion is very slow or can, in fact, be zero (green). This rate regime is called the residual rate r_r. Sometimes a resumption of the corrosion rate is observed (blue). This stage III regime, labeled r_2, is poorly understood. Most likely it is engendered by precipitation of secondary phases on the outside of the SAL.

1.2.3. Sharp interface

In the recent past a new analytical technique became applicable for glasses. Atom probe tomography (APT) opens new avenues to study glass corrosion. The spacial resolution ranges between 1 and 2 nanometers, which is a bit inferior to transmission electron microscopy (TEM). However, the huge drawback of TEM (or STEM) is that the sample is permeated by the electron beam over its total thickness. Therefore the results are just representing an average, which gives rise to need of a perfect sample preparation. For example, to resolve segregations in the

range of 5-10 nm or to observe a sharp interface, the sample has to be prepared by focused ion beam milling, perfectly perpendicular to it. The result of an APT, on the other hand, is a 3D map of the prepared sample. Moreover, not all elements are possible to map with this techniques. Recent studies by Gin et al. (2013a) and Hellmann et al. (2015) both showed a atomically sharp interface between the SAL and the pristine glass (Figure 1.5).

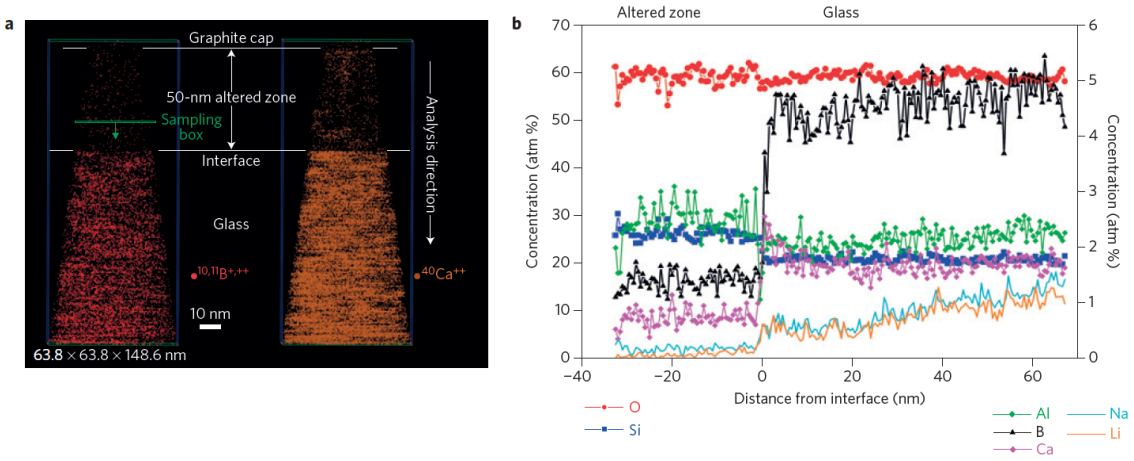

Fig. 1.5.: Atomically sharp interfaces observed with APT. **(a, b)**, APT results from an Internation Standard Glass (ISG) experiment in pure water at 90 °C by Hellmann et al. (2015). The nanometer sharp interface between the pristine glass (**(b)**, on the right) and the corrosion zone is obvious.

1.3. Mechanistic models for glass corrosion

Two mechanistic models for the SAL formation are controversially discussed in the literature. The leaching model establishes the idea of an *in situ* restructuring of residual, leached glass skeleton. Porosity is evoked by breakage of siloxan bonds and the subsequent release of molecular water. In this model, not all Si−O−Si bonds are broken. Contrary to the leaching, the ICDP model was introduced. The hypothesis here is that in the first stage the glass dissolves congruently. Nearby the glass surface a boundary layer is postulated, which can feature completely different physicochemical conditions compared to the bulk solution. In this boundary layer amorphous silica becomes supersaturated an precipitates on the former glass surface. Between the precipitated phase an inward moving fluid boundary layer emerges, which controls the coupled dissolution of the pristine glass and the deposition of silica on the existing SAL.

1.3.1. Leaching model

With the upcoming need to store vitrified nuclear waste in geological repositories scientists start to develop mathematical descriptions based on ideas for mechanistic models. Aagaard and Helgeson (1982) came up with an affinity based rate law for the dissolution of silicate minerals which takes into account the affinity of dissolved species in solution. The bedrock

of this rate law is the transition state theory which implies that reactions can be divided into one or several transition states with associated rates. Thus, the overall rate of a chemical reaction, like glass dissolution, is governed by the slowest intermediate step, the rate limiting step. Following this idea, the process of glass corrosion has to be divided into several steps, like breaking of siloxane bonds, diffusion of protons into the glass network and ion exchange of protons and network modifiers. As there are a vast number of these intermediate steps, especially in complex glasses, the applicability of this theory to model long term glass corrosion is highly questionable.

Grambow and Müller (2001) combined the affinity based rate law with the effect of network hydration by water diffusion and subsequent ion exchange. In this benchmark paper the authors provided a framework to describe glass corrosion under dynamic, as well as static conditions called first order rate law. They assumed that in a geological repository the affinity of glass constituents in solution will be always high, as no saturation occurs. In this case the formation of a porous SAL and the transport of water towards the pristine glass, as well as the protective nature of the SAL against silica transport must become rate limiting. The SAL and its inhibition of silica mass transport towards the solution is reflected by the formation of a second alteration layer between the pristine glass and the SAL which is considered to be a hydrated glass. This layer would be part of the glass phase and should show diffusion profiles for mobile species like boron or sodium. Furthermore, this leached glass zone (the secondary alteration layer) is hindering the diffusion of molecular water into the pristine glass and according to that responsible for the rate drop measured by the release of soluble species into solution. In summary, the authors here hypothesize that the growing SAL more and more becomes a transport barrier for silica species and a following second mechanistic regime of glass corrosion takes place reflected by the formation of a thin leached zone between the SAL and the pristine glass. Note that the authors do not give detailed information about the mechanism which underlays the SAL formation, which is considered to be formed subsequent to the dissolution of the silica network by surface stabilization due to solid/fluid equilibrium.

A comprehensive work by Frugier et al. (2008) gives an overview on current stage of glass corrosion research. Furthermore, the authors establish the GRAAL (Glass Reactivity with Allowance for Alteration Layer) model for modeling SON68 alteration (non-radioactive surrogate for French nuclear waste glass). The GRAAL model considers five basic reaction steps, coupled to observed rate regimes:

- **Stage I - Interdiffusion:** The corrosions process starts with protons diffusing into the pristine glass and a coupled ion exchange with the also positively charged network modifiers. The interdiffusion leaves behind a hydrated glass with anti-correlated sigmoidal concentration profiles. It is to note that the interdiffusion zone is assumed to be very thin and present during the whole corrosion process, always being the first attack to the

pristine glass.

$$\equiv Si{-}O^{-}\ M^{+} + H_3O^{+} \longrightarrow \equiv Si{-}OH + H_2O \tag{1.1}$$

- **Stage II - Initial rate (r_0):** In this stage the hydrolysis of the glass network (network builder) takes place. For example the siloxan bonds (Si−O−Si) are broken by nucleophilic attack of water molecules and silanol bonds (Si−OH) are formed (Equation 1.2).

$$\equiv Si{-}O{-}\equiv Si + H_2O \longrightarrow 2\,\equiv Si{-}OH \tag{1.2}$$

  Eventually, after the breakage of all siloxan bonds of a silicon atom, orthosilicic acid (H_4SiO_4) is released into the solution. The authors state that from this moment on the dissolution of the glass should be congruent, i.e. stoichiometric enrichment of the glass constituents in solution. However, congruent dissolution was not observed for most complex glasses. More rigid bonds, like Si−O−Zr are not prone to hydrolysis. For zirconium bearing glasses a congruent dissolution for all other glass constituents and the formation of zirconium gel on the former glass surface is observed in flow-through experiments with a constantly renewing of the solution (Frugier et al., 2001). Many factors are known to control the initial rate r_0, which are temperature, chemical composition of the glass and the pH value (Grambow, 1984; Advocat et al., 1990).

- **Stage III - Rate drop:** After the saturation of silicon in solution has reached a certain value, a fraction of it recondenses to form an amorphous, porous, hydrated phase commonly referred to as the 'gel' (Frugier et al., 2008). Here the authors state that the 'gel' is recondensed from dissolved silicon in solution. This is confusing, because the authors later describe the formation mechanism of the 'gel' as a residual glass skeleton, which recondenses *in situ*. Regardless the formation mechanism the rate drop can be attributed to (i) the affinity of silica in solution or (ii) a protective effect of the SAL. For the GRAAL model the authors conclude that it is a combination of both.

- **Stage IV - Residual rate (r_r):** In this regime, the rate remains constant or only a slight increase is observed. After the activities of glass constituents in the solution decreases and tends to be in equilibrium, the diffusion of water into the pristine glass becomes predominant. However, an experimental finding is that not only the network modifier cations become more enriched during the residual rate regime, the boron concentration is increasing, as well. Thus, interdiffusion cannot be responsible for the proceeding glass corrosion alone. To take account for that, the authors postulate a mechanism called reactive diffusion, which basically describes a kinetic hindering for the network hydrolysis. Here, most likely, as the rate limiting step the diffusion of molecular water is considered.

- **Stage V - Rate resumption (r_2):** In some cases, despite the type of borosilicate glass, after an extended time the corrosion rate increases significantly. This rate resumption is coupled to a massive precipitation of zeolites for the SON68 glass. It is assumed that for this case the secondary phase engenders major changes in the SAL extinguishing its passivating character.

For the authors the SAL has to be divided in two major zones. One zone is still attached to the pristine glass, even though it has changed regarding chemical composition by hydration, interdiffusion and reactive diffusion. The other zone is named the 'depleted gel' and is a result of the *in situ* recondensation of the residual and leached glass skeleton. An outline of the SAL structuring is given in Figure 1.6. In direct contact to the glass the zone of hydration is visible, the region of sheer water diffusion into the pristine glass. It follows the interdiffusion zone, where ion exchange between protons and network modifier cations takes place. Behind that, larger in dimension, the passivating reactive interface (PRI) is attached. Therein all constituents building up the 'depleted gel' are still present and all mobile elements, including boron, are depleted following typical sigmoidal diffusion profiles. The PRI is assumed to form when the affinity of glass constituents becomes low in the bulk solution. The result of the reactive diffusion is a with respect to mobile elements depleted residual glass skeleton, still connected to the pristine glass. At some point the formation of the gel starts by *in situ* repolymerization/recondensation of this skeleton. Breaking of siloxan and formation of silanol bonds lead to excess of molecular water, which is assumed to be responsible for the emergence of the observed porosity (Ohkubo et al., 2018). This theory of SAL formation during glass corrosion is supported by many authors (Bunker, 1994; Jégou et al., 2000; Grambow and Müller, 2001; Gin et al., 2011; Ma et al., 2017). What exactly the rate drop is attributed to remains open for discussion.

1.3.2. Interface-coupled dissolution precipitation model

The fundamental idea behind the ICDP model is that the congruent dissolution of the glass is coupled in space and time to the precipitation of the amorphous silica at an inward moving reaction front, the interfacial fluid. Such an replacement reaction is volume constant and assumed to control the alteration in many solid-water systems (Putnis, 2002; Putnis and Ruiz-Agudo, 2013; Putnis, 2014), as well as in water-mineral reactions with the SAL consisting of amorphous silica (King et al., 2011; Ruiz-Agudo et al., 2016; Liesegang et al., 2017). Within the model framework, the reaction is driven by the solubility difference of the parent and the product phase. The replacement reaction can be separated into several steps (Figure 1.7a-e):

- **Stage I - Congruent dissolution:** At the beginning of the corrosion process the glass dissolves congruently, i.e. the glass constituents are stoichiometrically released into solution.

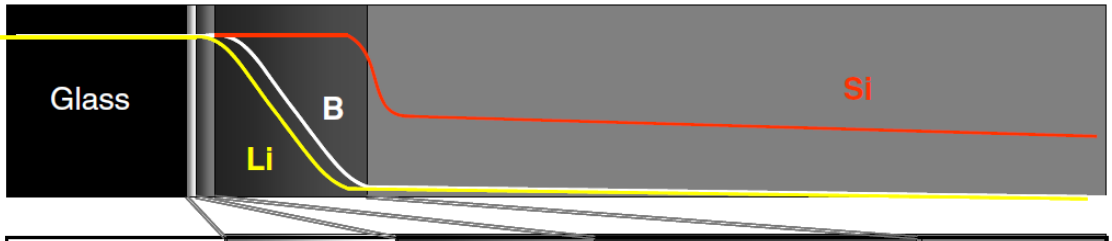

Zone : Glass	–1a– + H_2O	–1b– + H^+ - Li	–1c– + H_2O -Na Li B Mo IRP	–2– **Gel** also depleted in Si-Al-Ca…
Formation mechanism	Water diffusion	Exchange of alkali ions and protons	Reactive diffusion of all elements from solution or from crystallized phases, irrespective of their structural role	Hydrolysis / condensation. Rapid diffusion in pore water
Order of magnitude of possible thickness values "e"	Not observed. <1 nm if it exists	$e_{1b} << e_{1c}$ Approx. 1 nm	e_{1c} 3 to 300 nm $D \sim 1e^{-23}$ $m^2.s^{-1}$	e_2 Inversely proportional to S/V in a closed system
	Hydration	**Alkali interdiffusion**	**PRI**	**Depleted gel**

Fig. 1.6.: Structuring of the SAL on the basis of the leaching model, taken from Frugier et al. (2008). The first three zone are attached to the pristine glass and controlled by hydration, inter-diffusion and reactive diffusion. By *in situ* restructuring/recondensation of a residual, leached glass skeleton the 'depleted gel' is formed.

- **Stage II - Formation of a fluid boundary layer:** Nearby the former glass surface a fluid boundary layer (FBL) forms which becomes gradually enriched in dissolved silicon species. This fluid boundary layer can feature physicochemical conditions different from the bulk solution, e.g. with respect to the pH value.
- **Stage III - Precipitation of amorphous silica:** As soon as the FBL becomes saturated with respect to amorphous silica, the first silica spherules precipitating on the former glass surface. This is the moment where the rate starts to drop.
- **Stage IV - Formation of the SAL:** With proceeding of the corrosion a fluid rich film between the SAL and the pristine glass forms. This interfacial fluid is not in direct contact to the bulk solution and can have physicochemical conditions heavily different from it. The corrosion proceeds by congruent dissolution and precipitation of amorphous silica (on the inner side of the SAL) coupled to the inward moving reaction front.

- **Stage V - Diffusive transport through corrosion zone:** Secondary phases may precipitate on the outer side of the SAL depending on the composition of the fluid boundary layer. With advance of the replacement reaction and growth of the SAL the diffusive transport of dissolved species and water becomes rate limiting and slows down the corrosion rate resulting in r_r.

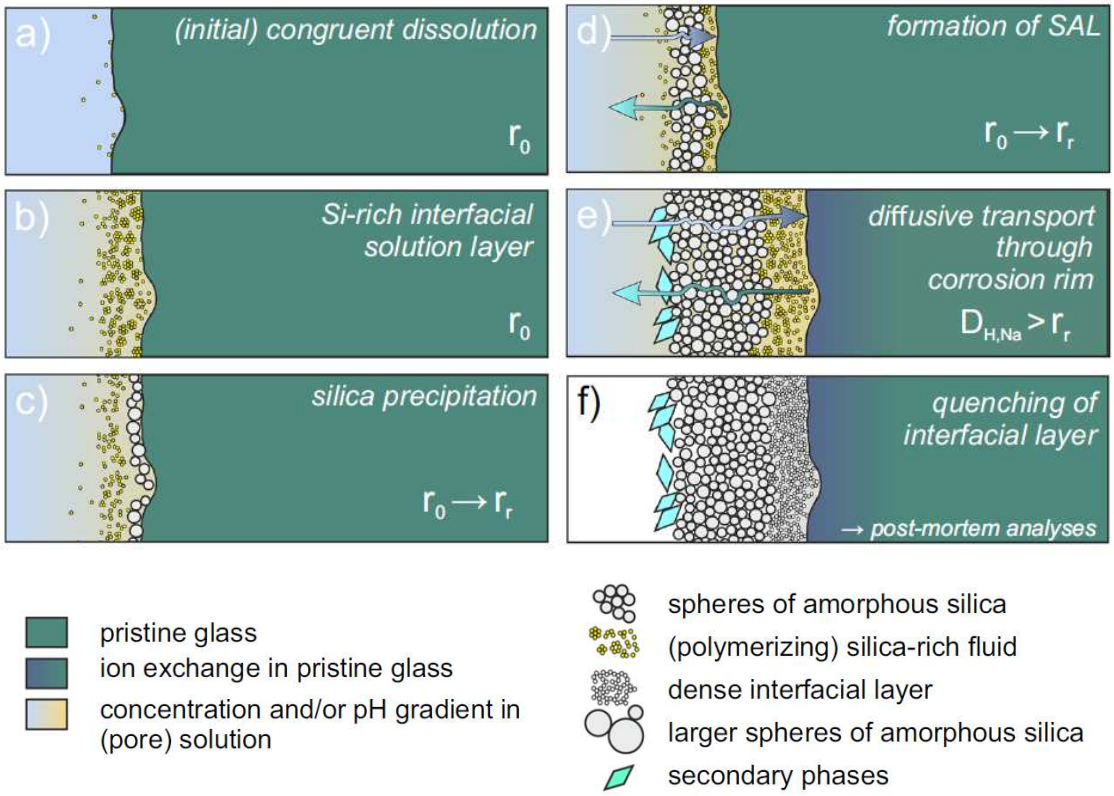

Fig. 1.7.: ICDP model for glass corrosion, modified after Lenting (2018). **(a)**, the glass dissolves congruently. **(b)**, an amorphous silica rich fluid boundary layer forms with physicochemical differing from the bluk solution. **(c)**, precipitation of the first silica spherules an the former glass surface. **(d)**, congruent dissolution proceeds and a fluid film between the pristine glass and the SAL. From this moment on the replacement reaction is operated by the congruent dissolution and coupled precipitation of silica on the inner side of the preexisting SAL. **(e)**, with growth of SAL the rate drops due to the conditions in the interfacial fluid (see main text). Because of the slow velocity of the inward moving reaction front, solid state diffusion starts at this stage forming an interdiffusion ion exchange zone. **(f)**, After quenching the silica rich interfacial fluid forms a dense layer, which is interpreted as the PRI in terms of the leaching model (Frugier et al., 2008).

The authors suggest here that with the rate drop the overall corrosion becomes slower than the interdiffusion and a ion exchange zone can form (blueish zone in pristine glass, Figure 1.7e). From this moment on, the ICDP process has lost control over the element release in the interfacial fluid, which now has been taken over by the ID process. In conclusion, the formation of the ID zone is dependent on the velocity of the inward moving reaction front of the ICDP process, which has to lie beneath the diffusion velocity of protons into the glass at 90 °C ($1.3 \times 10^{-23}\ m^2 s^{-13}$). An ion exchange zone has been found by many other authors,

e.g. by Gin et al. (2017) during other experiments with r_r close to zero, but was interpreted to operate the whole glass corrosion process from the beginning on. Hellmann et al. (2015) conducted atom probe tomography measurements on corroded glass samples. In this study no ID zone was found, only a nanometer-sharp interface between the glass and the SAL. Lenting (2018) suggested that this may be due to the fact that the experiments have been stopped before it has formed.

In many studies a zone was found between the porous SAL and the pristine glass with an ID zone called the PRI (Frugier et al., 2008). This zone has a small pore size (beneath 1 nm) and a relatively high concentration of mobile species compared to the SAL. Lenting (2018) suggest here that it represents the quenched interfacial fluid.

Within the ICDP model framework the rate drop is explained by the complex chemistry and polymerization reactions of amorphous silica. In stage IV of the model, when the transport of dissolved species through the SAL becomes rate limiting, the interfacial fluid becomes enriched with respect the mobile elements. This results in an increase of the pH, which makes it possible to dissolve more silica into the fluid film. Under such conditions amorphous silica forms cyclic tetramer, which may subsequently polymerize to three-dimensional polymer particles (Iler, 1979; Lenting, 2018). It is assumed that in the formed gel pores water becomes increasingly trapped. Eventually this leads to a hindering of mobile species diffusive transport and the observed drop in the corrosion rate.

The elegance of this model lies in the possibility of explaining all the observations made like atomically sharp interfaces, ID zones, the rate drop, and even pattern formation. The latter could be attributed to the complex chemistry of amorphous silica. Like mentioned above, the pore size of precipitated silica depends on many parameter, like pH value or salinity (Iler, 1979). A thinkable scenario would be that with growth of the SAL the physicochemical conditions of the interfacial fluid may change dramatically due to depolymerization reaction. For example the precipitation of silica can be sterically hindered. Slight changes in the interfacial fluid may cause abrupt deposition of a major portion of the dissolved silica with unique pore size and cation content. After that a 'new' interfacial fluid may form and the corrosion proceeds. The possible enrichment of the precipitated silica with respect to one of several present network former cations and the different diffusion velocity of them may now result in fluctuations which are able to produce structural and chemical pattern.

1.4. Objectives

Aim of this work was to address several questions, as well as developing *in situ* hyperspectral Raman spectroscopy as a method for the observation of glass corrosion. Like mentioned above, most of our knowledge about the SALs are derived from methods which are limited to the dried corrosion product. Thus some pressing questions to answer with *in situ* techniques arise, because many conclusions drawn regarding the corrosion mechanism are based on these

results. Some features inherent to an ICDP mechanism should be verified by in situ Raman spectrosocopy, such as (i) the existence of an interfacial fluid and (ii) a fluid boundary layer, which both cannot be observed using post mortem techniques or bulk solution sampling, and (iii) an inferred transport limitation of water through the SAL, which should shed light on the often observed rate drop. Furthermore, in the method section new avenues opened by the Raman *in situ* technique are to work out in detail, which could make fluid-cell Raman spectroscopy to a cutting edge tool for observation of glass corrosion and other fluid-solid reactions:

- **Fluid-cell:** Design and construction of a fluid-cell setup in which samples can be placed easily and no extensive preparation is needed.
- **Corrosion rates:** Following the glass retreat will open a possibility to observe the evolution of corrosion rates with time and a temporal resolution which could only be achieved by bulk experiments with an unbearable effort.
- **pH values:** By using the pH dependence of dissolved carbonate ion speciation it will be tried to calculated the solution pH from the Raman spectra with a high special resolution.
- **Temperature:** The position of Raman bands is dependent on the temperature. Here the idea is to use dissolved carbonate bands to calculate the temperature in solution with an high spatial resolution by use of a appropriate calibration.

CHAPTER 2

Introduction to Raman spectroscopy

The interaction of electromagnetic radiation with atoms and molecules is multifarious. Inner electron transitions, for example, are excited by X-rays. Hereafter only the interactions leading to the oscillation of molecules is considered more closely. The Raman effect is a sheer scattering phenomenon where light is inelastically scattered by molecules.

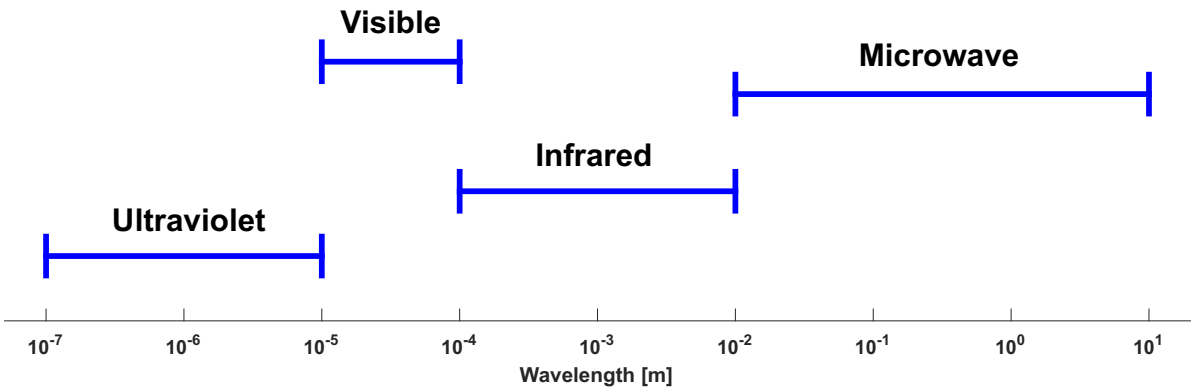

Fig. 2.1.: The electromagnetic spectrum

The electromagnetic spectrum is divided into distinct areas according to the wavelength (Figure 2.1). In the illustrated regions, different interactions with molecules occur, but these are not necessarily limited to the discrete region. A rough assignment can be made:

- **Microwave**: Electromagnetic waves of this energy are absorbed by energy level transitions coupled to electron spin states (EPR spectroscopy). Beside that, rotational spectra of small molecules in the gaseous phase can be observed.
- **Infrared**: In the far infrared, rotations of molecules and molecular groups are excited while electromagnetic radiation in the near infrared is giving rise to molecular vibrations.
- **Visible**: Electron transitions of weakly bound valence electrons. These band spectra

(atomic emission/absorption spectra) are originated from the electron transitions combined with the superimposed rotational and vibrational conditions of the molecule.

- **Ultraviolet**: With ultraviolet photoemission spectroscopy the energy level transition of strongly bound valence electrons can be investigated.

In this section the principles of molecules vibrations are presented which is necessary to understand Raman spectroscopy. For simplification, all explanations and examples refer to diatomic molecules.The literature used for this section is Bethge et al. (2004), Bernath (2005) and Hänsel et al. (2000).

Molecule vibrations can be examined by two techniques. In the case of infrared (IR) spectroscopy light in the wavelength region $0.8 - 1,000$ µm is absorbed by molecules. Vibrations are observed in the near infrared (NIR) and mid infrared (MIR), whereas quantized transitions in rotational energy of molecules are observable in the far infrared (FIR) and the microwave region. With rotational spectroscopy characteristic absorption lines of molecules in the gaseous phase can be measured, if the dipole moment changes with the rotational state. This is not the case for homopolar molecules like N_2 or H_2 that are referred to as infrared inactive. However, these molecules undergo changes in the polarizability, which is the condition for being Raman active. Thus, for many infrared inactive molecules rotational spectra can be obtained via Raman spectroscopy. It is noted that during Raman scattering process molecules are excited in a virtual state from where they fall back to the ground state. If the molecules are directly excited in actual state the Raman intensity rises by several orders of magnitude. This phenomenon is called resonance Raman. In the following, the Raman effect is described in detail and a short overview about molecule vibrations is given.

2.1. Raman effect

In contrast to the absorption of electromagnetic radiation by molecule vibrations, the Raman effect is based on the inelastic scattering of light on molecules. Scattering is defined as interaction of electromagnetic waves with material objects. In the case of visible light, most of the waves are scattered elastically, which means, the re-emitted wave has the same energy. Only a small portion is scattered inelastically, i.e. the scattered light is blue or red shifted. The change in the wave's energy is engendered by the interaction with quasi-particles occurring the elastic field. These phonons are representing an elementary vibrational mode or an excited state in terms of quantum mechanics. The acoustic phonon represents a mode caused by many atoms vibrating in a chain. The scattering of light on these phonons is called Brillouin scattering and the frequency shift lies in the gigahertz range, whereas the frequency shift for the optical phonons is in the terahertz region. These optical phonons are caused by bonded atoms vibrating against each other and are investigated by Raman spectroscopy. Optical and acoustic modes are illustrated schematically in Figure 2.2 by use of the diatomic chain example. In the

scope of this work are the Raman modes to obtain structural information from glasses and corrosion products, as well as from aqueous solutions.

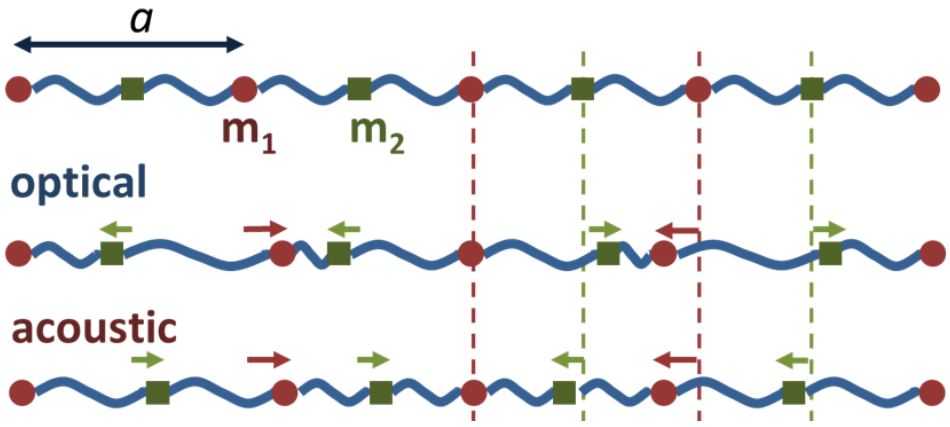

Fig. 2.2.: Optical and acoustic modes. Illustrated is a linear diatomic chain with the masses of the atoms m_1 and m_2. The optical phonon represents a local vibration of the two atoms against each other, whereas during an acoustic wave passing the chain, a larger number of atoms vibrating together in the same direction.

When an electromagnetic wave interacts with molecules, a dipole is induced with a magnitude depending on the band polarizability. The relationship between the induced dipole momentum $\vec{P}$ and the electric field $\vec{E}$ is given by:

$$\vec{P}(t) = \tilde{\alpha}\vec{E}(t) \tag{2.1}$$

With $\tilde{\alpha}$ being the polarizability of the molecule. Considering nonlinear molecules, it becomes evident that $\tilde{\alpha}$ is not a scalar quantity. In this case, the polarizability must depend and the direction of the electric field which can be described mathematically with a 2^{nd} order tensor. Considering an isotropic case with the time dependent electric field of the excitation Laser ($E_0\, cos(\omega_0 t)$) it follows:

$$\vec{P}(t) = \alpha\, E_0\, cos(\omega_0 t) \tag{2.2}$$

The time dependent dipole momentum (Hertzian dipole) emits an electromagnetic wave, which is called Rayleigh scattering. The scattering intensity depends on the squared dipole momentum and the 4^{th} power of the excitation wavelength. Thus, lasers with higher energy will lead to an increase in the scatter Raman light intensity.
The ability of a molecules to vibrate results in a deformation of the bond orbital. Therefore, the polarizability is a function of the normal mode's coordinate q:

$$\alpha = \alpha(q) = \alpha_0 + \left(\frac{\partial \alpha}{\partial q}\right)_0 q \tag{2.3}$$

Considering the time dependence of the normal coordinate during the vibration, which can

be described with the harmonic oscillator ($q(t) = q_0\, cos(\omega_{Os} t)$). By combining the latter with Equation 2.2 and 2.3 it results:

$$P(t) = \left[\alpha_0 + \left(\frac{\partial \alpha}{\partial q}\right)_0 q_0\, cos(\omega_{Os} t)\right] E_0\, cos(\omega_0 t) \tag{2.4}$$

Expansion of the product of the two cosine gives:

$$P(t) = \underbrace{\alpha_0 E_0\, cos(\omega_0 t)}_{Rayleigh} + \underbrace{\frac{1}{2}\left(\frac{\partial \alpha}{\partial q}\right)_0 q_0 E_0\, cos((\omega_0 - \omega_{Os})t)}_{Stokes} + \underbrace{\frac{1}{2}\left(\frac{\partial \alpha}{\partial q}\right)_0 q_0 E_0\, cos((\omega_0 + \omega_{Os})t)}_{Anti-Stokes} \tag{2.5}$$

From the resulting Equation 2.5 it can be taken that additionally to the Rayleigh scattering a portion of the scattered light is red shifted and another portion is shifted to higher energies. These Stokes and anti-Stokes band will have the same shift relative to the excitation wavelength in absolute wavenumbers. A simplified illustration of the resulting spectrum can be found in Figure 2.3.

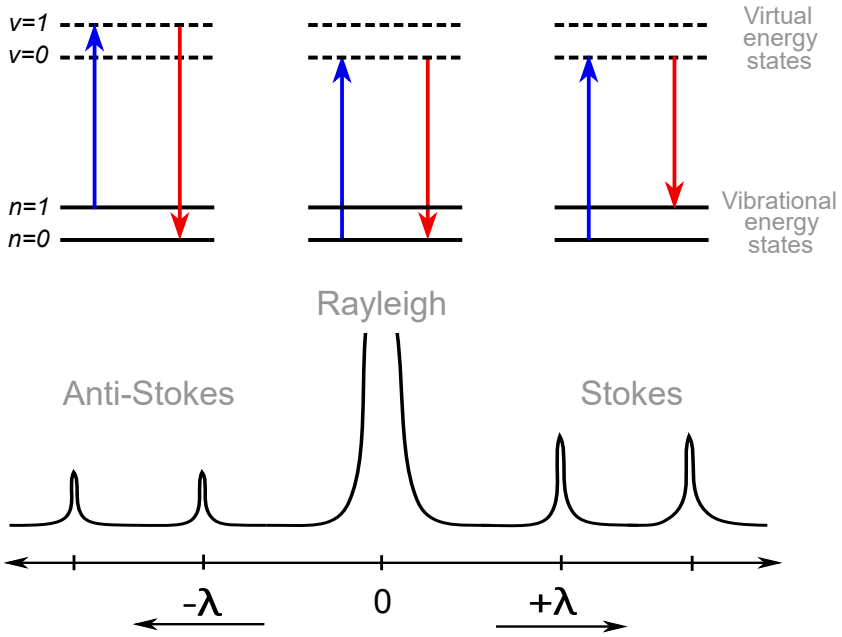

Fig. 2.3.: Sketch of Stokes and anti-Stokes scattering. When light is scattered on a molecule, it changes from a ground vibrational level (n) to an excited state, which is not an actual vibrational energy state (v). From this virtual state the molecule falls back into a vibrational state. If the molecule is already in a higher vibrational state ($n = 1$), which is the case at higher temperatures, it can fall back into a lower vibrational state ($n = 0$). It follows that the emitted electromagnetic wave is blue-shifted, which is called anti-Stokes shift.

2.2. Molecular vibration

Based on the laws of quantum mechanics, energy is quantized. In the following it is described how vibrational energies can be calculated by considering these rules. As an approximation, the vibration of a diatomic molecule can be described with classical mechanical equations. According to Hook's law the restoring force of two masses, which are connected by a spring, is proportional to the displacement (Figure 2.4):

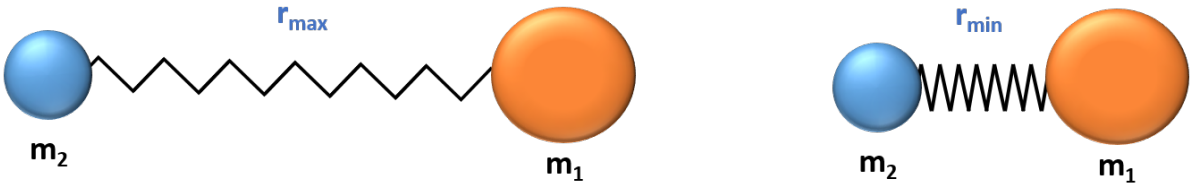

Fig. 2.4.: A diatomic molecule with the masses m_1 and m_2 are vibrating. The maximum and minimum distance between the atoms is marked as r_{max} and r_{min}, respectively. Assuming the bonding as a spring, the vibration can be described with Hook's laws.

$$F = -D(r_{max} - r_{min}) \tag{2.6}$$

D is called the force constant and stands for the bonding strength of the molecule. With the reduced mass the frequency of the vibration is:

$$f = \frac{1}{2\pi}\sqrt{\frac{D}{\mu}} \tag{2.7}$$

Like mentioned above the rules of quantum mechanics need to be considered. The energy of the vibration's frequency E_f with the quantum number v and the Planck constant h is:

$$E_f = \left(v + \frac{1}{2}\right)hf \tag{2.8}$$

It follows that even for the quantum number 0 there needs to be an energy, the so called zero-point energy. A model concept of the quantum theory is the harmonic and disharmonic oscillator. If vibrational states are described with the harmonic oscillator the energy difference between the levels is always hf (Figure 2.5a). The consequence for a Raman band is that every transition between the energy levels have the exact amount of energy which would result in the same frequency shift. Here, changes in energy levels are following the rule $\Delta = \pm 1$. However, an atomic bond cannot be stretched or clinched arbitrarily. If a specific distance between the atoms is reached the bond will break and the atoms will fade away from each other. This process is called dissociation with its respective dissociation energy (d). Considering the shape of the energy function of a molecule changes significantly (Morse potential), vibrational energies can be calculated with:

$$E_f = d\left(1 - e^{-a\Delta r}\right)^2 \tag{2.9}$$

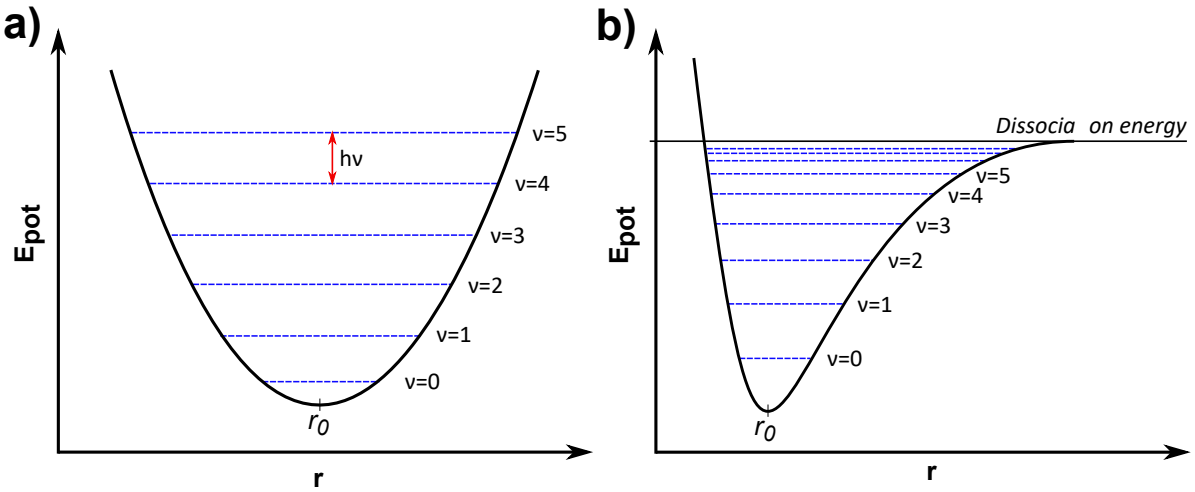

Fig. 2.5.: Energy functions of a harmonic **(a)** and a anharmonic oscillator (Morse potential) **(b)**.

The constant a is unique for every kind of atomic bond and defines the shape of the energy function displayed in Figure 2.5b. In the case of the anharmonic oscillator transitions from the ground state of more than ± 1 are allowed, the overtones. If a molecule is already in an excited state a transition into another excited state is called hot band. Hereby a second band will appear in the Raman spectrum due to the non-equidistant energy levels. Sometimes the band frequency visible in the Raman spectrum is not the result of a single vibrational level transition. If more than one normal mode is excited simultaneously the resulting band is called a combination band and in the case of sum transition it appears at a slightly lower energy of the sum of both fundamental modes. Rotational bands, e.g. for N_2 will appear on the Stokes and anti-Stokes side of the main band as a set of narrow lines.

Vibrational modes are divided into six types depending on the movement direction of the involved atoms relative to each other. The types are explained in the following by using the methylene group as example. When the two H atoms are simultaneously change the bonding length to the carbon atom it is called symmetric stretching (ν_s) in the case of symmetrical and asymmetric stretching (ν_{as}) in the case of asymmetrical length change of the bonds. A schematic drawing of the stretching modes and other vibrations can be found in Figure 2.6. The other fundamental vibrations are labeled with δ, ρ, ω, and τ for bending, rocking, wagging and twisting modes, respectively. Another possible vibration is the out-of-plane vibration. In boron trifluoride, for instance, the B atom can move out of the plane defined by the three F atoms.

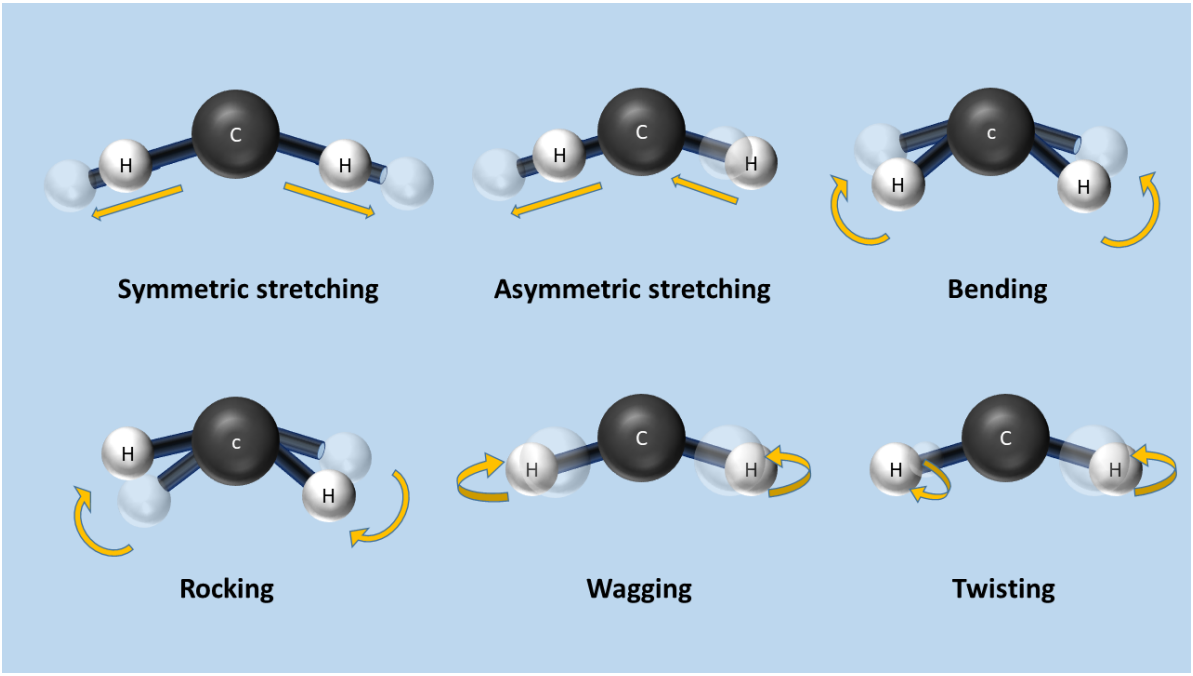

Fig. 2.6.: Sketch of possible molecule vibration. The vibrations are labeled with ν_s and ν_{as} for symmetric and asymmetric stretching, δ for bending and ρ for the rocking mode. For the wagging (ω) and twisting (τ) vibration the hydrogen atoms are moving out of the drawing plane.

CHAPTER 3

Materials and methods

3.1. Glass synthesis and glass monolith preparation

Ternary borosilicate glass was synthesized from SiO_2, B_2O_3, and $NaCO_3$ precursors in a platinum crucible (1,000 ml) at 1,200 °C, casted in a steel mould and cooled to ambient temperature at 1 Kelvin per minute. Since the first glass contained several bubbles, it was crushed, melted again at 1,350 °C, and stirred with a platinum stirrer. After the second melting, the glass was visibly bubble-free and was chemically and physically characterized (Table 3.1). For the hydrothermal experiments, glass coupons with a size of 10.0 x 8.0 x 1.5 mm^3 were cut from the glass block, polished to optical quality by using a 1 µm CeO_2 slurry, and cleaned with ethanol.

At SCHOTT AG (Mitterteich plant site), glass tubes are produced as wrought product for pharmaceutical packaging. During a subsequent hot forming process the tubes are cut, closed on one side and a vial or syringe is formed. The tubes are manufactured by pouring the glass melt on the upper side of a slightly downwards tilted, rotating blowpipe and pulling the slowly solidifying tube away from the pipe on the lower side. To produce a tube with a steady diameter and wall thickness, the blowpipe is equipped with a hole in the middle, to which a constant gas flow is applied. Usually about three meters of glass tubes are produced per second and close monitoring of the process regarding blowpipe rotating speed, gas flow and pulling speed is essential. The AR-GLAS® and the aluminum-borosilicate glass (ABG) tubes (65 mm) used in this study were cut to segments with 10 mm in height and 8 mm in width. The abutting faces were polished to optical quality by use of a 1 µm CeO_2 slurry and cleaned with ethanol. The chemical composition of the glass is given in Table 3.2 in comparison to ternary borosilicate glass (TBG).

In case of *post mortem* analysis, the coupons were rinsed with Milli-Q® and dried in a desiccator for at least a week. Subsequently, the samples were embedded in epoxy resin, cut and polished to optical quality. For microprobe analysis, the bevels were coated with carbon.

Table 3.1.: Chemical and physical properties of the ternary borosilicate glass used for the experiments. Abbreviation: X-ray fluorescence analysis (XRF)

	Value	**Method**	**Norm**
SiO_2	57.9 wt.%	XRF	DIN EN ISO 12677:2011
B_2O_3	22.3 wt.%	XRF	DIN EN ISO 12677:2011
Na_2O	19.7 wt.%	Titration	DIN EN ISO 21078-1:2008
Total	99.9 wt.%		
Thermal expansion coefficient (α)	9.13 x E^{-66}/K		ISO 7991:1987-12
Glass transition temperature (T_g)	559 °C		DIN 7884-8: 1998-02
Density	2.5179 g/cm^3		ASTM C 693: 1993-11

Table 3.2.: Chemical composition of all glasses examined in the study. Oxide quantities are given in weight percent and determined by X-ray fluorescence analysis.

	TBG	**AR-GLAS®**	**ABG**
SiO_2	57.9	69	75
B_2O_3	22.3	1	10.5
Al_2O_3		4	5
Na_2O	19.7	13	7
K_2O		3	
BaO		2	
CaO		5	1.5
MgO		3	

3.2. Solution preparation

The $NaHCO_3$ and TAHM ($C(CH_2OH)_3NH_2$) solutions were prepared with Milli-Q® and p.a.-grade powder from Merck. The powders were weighed in on an analytical balance from Mettler Toledo. Samples from the hydrothermal experiments were centrifuged with 6,000 revolutions per minute for 10 minutes to remove any precipitates, transferred with a pipette to a vial and stabilized using p.a.-grade 2% nitric acid with a dilution factor of 1:10.

3.3. Batch experiments

The hydrothermal experiments were carried out in homemade steel reactors with Teflon® inlays. The inlays had an inner diameter of 12 mm and were 24 mm in height. Before use, the

inlays were stored in analytical-grade concentrated HNO_3 for two hours, rinsed with Milli-Q® and cleaned for 15 minutes in an ultrasonic bath. After renewed rinsing with Milli-Q®, they were dried in a compartment dryer at 40 °C. With a piston operated Eppendorf® pipette, a volume of 2 ml of the respective solution was added to the reactor, which was then tightly closed. The reactors were transferred to the ovens and remained there at 90 °C for a defined period of time (Table 4.2). Afterwards, the reactors were removed from the furnaces and cooled to room temperature. The solution was then centrifuged at for 8 minutes and the supernatant was used for further experiments.

3.4. Raman spectroscopy

In the present study, two different Raman spectrometers were used. Both spectrometers are equipped with a 2W frequency-doubled Nd:YAG Laser (532.09 nm emission wavelength) that were used as excitation source. For one, a Horiba Scientific LabRam HR 800 spectrometer located at the Steinmann institute of the University of Bonn was employed. It has an adjustable confocal slit and pinhole and two diffraction gratings (600 and 1,800 grooves/mm). The spectrometer was initially calibrated using a build-in software routine by measuring the first order Si band at 520.7 cm^{-1} of a polished silicon wafer. However, for long-term measurements, a Ne line at 1,707.64 cm^{-1} was used as internal frequency standard to correct for any spectrometer shift during long-term acquisition (see below). The objective used for all *in situ* experiments was an Olympus 100x long-distance objective with a numerical aperture of 0.75. At SCHOTT AG research center in Mainz, a WiTec M300+ Raman spectrometer (WiTec, Ulm, Germany) was used. It has confocal setup as well, but not with an adjustable slit and pinhole. Three diffraction gratings are built in (600, 1,200 and 1,800 grooves/mm). The gratings are calibrated for spectral accuracy by a build-in software routine using the atomic emission lines of a He-Ar lamp.

3.4.1. Spectra treatment and band fitting

In all experiments, two wavenumber regions were recorded for each point in space and time to save time considering that every single map consists of 300 spectra and represents only one time step. To correct for any frequency shift during long-term measurements, a Ne light source was placed in the beam path of the Raman spectrometer, leading to the occurrence of additional neon-specific spectral lines in every spectrum. Since the position of neon-lines are physically intrinsic, spectra can be corrected using Ne line emission wavelength that are listed by the American National Institute of Standards and Technology (NIST, 2018) or in the literature (Saloman and Sansonetti, 2004). For correction the lines at 585.248 nm, 667.827 nm were used, occurring in the spectra at 1,707.04 cm^{-1} and 3,819.88 cm^{-1}, respectively. Signals originating from cosmic rays were removed automatically by the software. Additionally, measured Raman intensities I_{Obs} were corrected for (i) the wavelength-dependent instrumental

sensitivity (white light correction), (ii) the thermal population of the excited states by the Bose–Einstein temperature factor $B = [1 - exp(-h\nu c/kT)]$ with h, k, c, and T being the Planck and Boltzmann constant, the speed of light, and the absolute temperature, respectively, (iii) the scattering factor $qs = (\nu_e - \nu) - 3$ with ν_e and ν being the excitation wavenumber and Raman shift, respectively, and (iv) the frequency factor ν (Long, 1977):

$$I = I_{Obs} \times \nu_0^3 \Big[1 - exp\Big(\frac{-hc\nu}{kT}\Big)\Big] \times \frac{\nu}{(\nu_0 - \nu)^3} \tag{3.1}$$

In cases where the correction was performed, it is mentioned in the figure caption. Equation 3.1 slightly differs from the original given by Long (1977) to take into account that the intensities are no longer measured in Watt, but in counts per unit time. Any further spectra treatment, such as the determination of integrated intensities or background subtraction, is reported in detail in the respective methodology section.

3.5. Electron microprobe (EMP)

The corrosion products were qualitatively analyzed with respect to Si (Kα), Ba(Kα), Na(Kα), Mg(Kα), K(Kα), Al(Kα) and Ca(Kα) at the Steinmann institute in Bonn by a JEOL JXA superprobe (JOEL Germany GmbH, Freising, Germany), using a acceleration voltage of 15 keV and a beam current of 10 nA. For the wavelength dispersive analysis, natural oxide glass and silicate standards are used for peak identification. As the corrosion products in the SAL are highly porous and long dwell times lead to excessive sodium loss, a dwell time of 0.5 seconds with two accumulation phases was used for mapping. All point-by-point mappings have a vertical and horizontal distance of 1 µm between two points.

3.6. Inductively coupled plasma optical emission spectroscopy (ICP-OES)

Solution samples were analyzed by inductively coupled plasma optical emission spectroscopy (ICP-OES) at SCHOTT AG research center in Mainz using an Agilent 725 spectrometer (Agilent Technologies, Santa Clara, USA) with a radial setup. All solutions were diluted 1:10 with Milli-Q® ultra-pure water prior to analysis. The machine was calibrated using commercially available standard solutions by Merck for the measured elements (Al, B, Ba, Ca, K, Mg, Na, Si).

CHAPTER 4

Method development: Fluid-cell Raman spectroscopy

As shown in a preliminary Raman *in situ* experiment conducted by Lenting (2018), fluid-cell Raman spectroscopy allows studying glass corrosion phenomena spatially resolved and real time. In this study, the emergence of the surface alteration layer (SAL), the formation of a gap between the SAL and the pristine glass, and the time-dependent polymerization of silica, forming the SAL, could be observed. In this work, it will be evaluated which particular questions concerning glass corrosion can be answered, i.e., what are the potential applications for *in situ* fluid-cell Raman spectroscopy. Each experimental example presented in this study is discussed in detail in a separate section of this chapter.

4.1. Kinetic pretest *ex situ* studies

For preliminary testing, three different glasses were chosen as samples of interest for potential *in situ* experiments. To obtain an comprehensive dataset on a single glass composition that could act as a basis for numerical modeling, the chemically simple TBG was initially chosen as a model glass for the experiments, because this glass is highly susceptible to corrosion so its corrosion kinetics is fast enough to be studied by *in situ* fluid-cell Raman spectroscopy within less than two weeks for which the Raman spectrometer has to be available. To obtain the same dataset for more durable glasses, e.g., the international simple glass ISG (Gin et al., 2013a), experiments need to run for months to years. Nevertheless, the motivation for this work was to also apply the method to highly resistant glasses, such as borosilicate glass tubes, for primary pharmaceutical packaging. At SCHOTT AG, vials or syringes made for holding parenteral pharmaceutical solutions are made from the ABG. For these two industrial glasses the resistance class for attack by aqueous solutions in acidic, neutral, and basic pH regime as determined by DIN standards is displayed in Table 4.1. Regarding these norms, a low number stands for a high resistance. The AR-GLAS® included in this study, because it has a poor

hydrolytic resistance compared to the ABG, while the acidic and basic resistance class is the same. The norms used are: DIN (1989-12, 1994-02, 2001-03).

Table 4.1.: Chemical resitance of ABG and AR-GLAS® determined by DIN standards.

	AR-GLAS®(8350)	**ABG**
Acidic resistance (DIN 12116)	Class 1	Class 1
Hydr. resistance (DIN ISO 719)	Class 3	Class 1
Alkali resistance (DIN ISO 695)	Class 2	Class 2

To investigate the glasses performance while corroding in aqueous solution over the whole pH regime and at different temperatures, several batch experiments were performed (Table 4.2). As the ABG was the most interesting and corrosion-resistant glass, experiments were conducted at both temperatures as well as in all pH regimes. The other two glass were only corroded in Milli-Q® at both temperatures, as the stability of the TBG in acidic solution was known from previous studies (Geisler et al., 2010; Dohmen et al., 2013). Corroded glass coupons were analyzed after the hydrothermal experiments by electron microprobe analysis and the element concentration in solutions was measured by inductively-coupled plasma optical emission spectroscopy (cf. Chapter 3).

Table 4.2.: All batch experiments were conducted in homemade reaction cells with Teflon® inlay. The acidic attack was performed in a 19% HCl solution, whereas for the basic attack a 50:50 mixture of 1M $NaCO_3$ and 1M NaOH was used. Hydrolytic resistance experiments were conducted in Milli-Q®

D[d]	T[°C]	Acidic	Basic	Hydrolytic		
		ABG	ABG	ABG	8350	TBG
7	98	✓	✓	✓	✓	✓
	121	✓	✓	✓	✓	✓
14	98	✓	✓	✓	✓	✓
	121	✓	✓	✓	✓	✓
21	98	✓	✓	✓	✓	✓
	121	✓	✓	✓	✓	✓
28	98	×	×	✓	✓	✓
	121	×	×	✓	✓	✓
35	98	✓	✓	✓	✓	✓
	121	✓	✓	✓	✓	✓
42	98	×	✓	×	✓	✓
	121	×	✓	×	✓	✓

4.1.1. *Post mortem* analysis

Representative run products were analyzed *post mortem* using EMP and SEM. No corrosion zones were visible in all of the backscattered electron (BSE) images of the samples corroded in acidic solution. The edges appeared sharp and the degree of brightness, indicating the average atomic weight of the investigated material, was the same across the entire samples (cf. Appendix Figure B.1). This was also the case for the technical glass samples corroded in Milli-Q®. Merely the TBG samples partially showed signs of corrosion, which correlates well with the corresponding solution chemistry. In some of the BSE images (cf. Appendix Figure B.1) extensive corrosion zones with intriguing features were observed, particularly at areas where excavations were caused by the polishing procedure. These samples were investigated in little more detail by scanning electron microscopy. Secondary electron images of a TBG sample corroded in Milli-Q® for 21 days at 121 °C are shown in Figure 4.1. In 4.1a, a thin dense rim is visible on the outermost part of the corrosion zone. An extensive excavation is located right below it. Its bottom is bowl-shaped and consists of a large number of round tips on top of stalagmite-like structures that are oriented perpendicular to the former glass surface. Based on the BSE contrast (cf. Appendix Figure B.2), it is likely that the "stalagmites" are composed of a corrosion product. However, it is no obvious whether or not the structures were formed during the experiment or rather have emerged during the drying process. Images with increased magnification reveal that the stalagmites composed of different layers that are oriented parallel to the former glass surface (Figure 4.1b) and composed of spherical structures (Figure 4.1c). In Figure 4.1d, a frequently found palisade-shaped structure is shown. Conspicuously, the formation of at least two distinct sets of palisades perpendicular to the former glass surface can be observed. The outermost layer on the right, i.e., solution side is composed of spherical aggregates. A BSE image of the polished corrosion zone without the excavation would most certainly show a pattern (layering) parallel to the corrosion front.

The outer dense rim in Figure 4.1a apparently represents the outermost corrosion product that was in contact with the solution. However, the BSE image in Appendix B.3 shows a comparable structure, followed by a hundred micrometer wide gap and another dense rim. Thus, this outermost rim possibly was detached during the preparation process in the case of the sample shown in Figure 4.1.

In Figure 4.2, a BSE image of the AR-GLAS® sample, corroded in an alkaline solution for 28 days at 98 °C, is shown along with qualitative chemical distribution maps obtained by EMP of the region marked with the red rectangle. The pristine glass is followed by a zone composed of spherical structures that are gradually packed more densely towards the solution side and composed of Si, Al, and Mg. Between this layer and the glass, a gap is visible, which either represents a detachment of the corrosion zone or is filled with a low-density material not detectable by EMP. A palisade-like structure, as described above, is also visible. The palisades with a higher contrast in the BSE image are silhouetted in every chemical map, except for K.

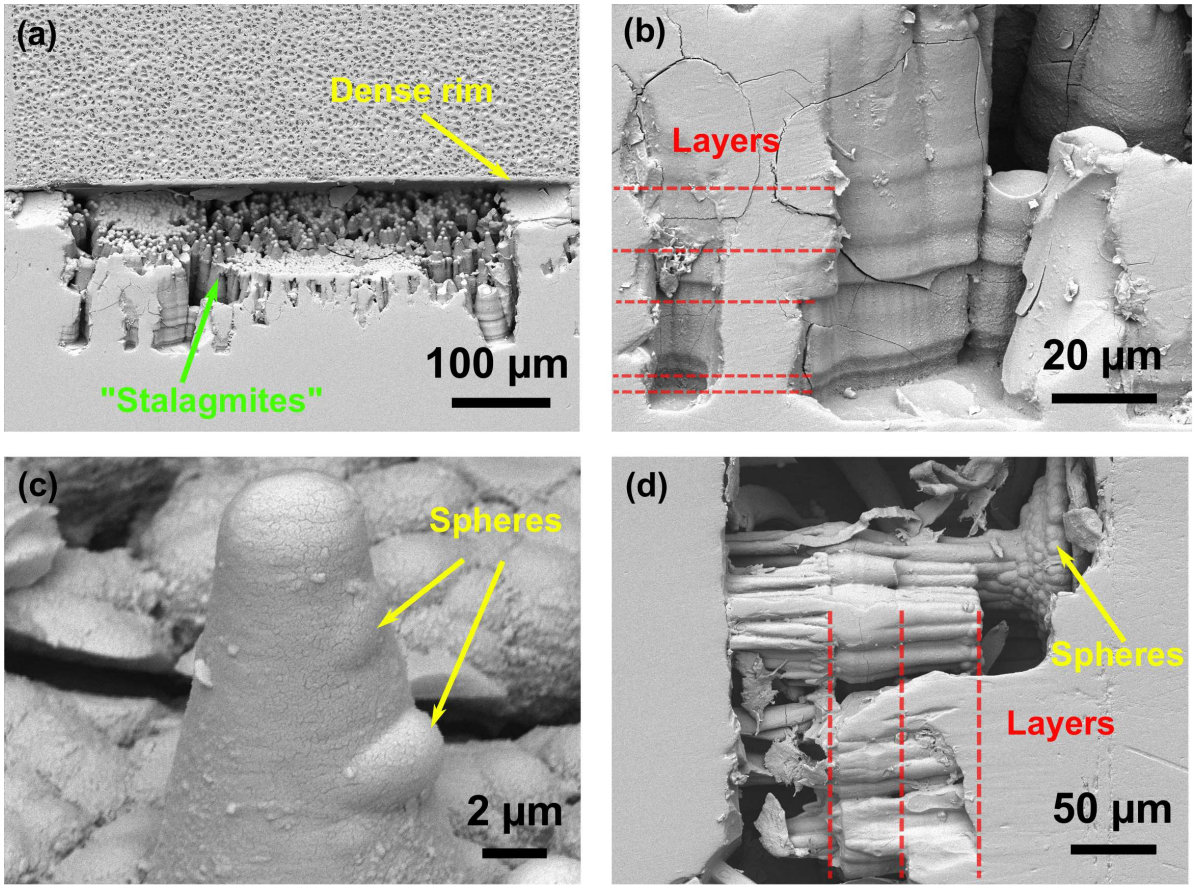

Fig. 4.1.: SEM analysis of the TBG corroded in Milli-Q® at 121 °C for 6 weeks. Some excavations were caused by the polishing procedure, giving unique insight into structural features of the dried SAL. Some of the 'stalactites/-mites' shown in **(a)** appear on a closer look to be composed of small spherules **(b)**, which are known to be the first precipitates of amorphous silica. Higher magnification **(c)** suggest that the stalagmites are composed of spherical structures. In **(b)**, a sharp layering perpendicular to the corrosion front is visible, as well as in **(d)**.

The outermost layer of the corrosion zone is enriched in aluminum and covered with crystal on the solution side. Barium and potassium are strongly enriched in a number of coarse crystal aggregates, appearing bright white in the BSE image. Another secondary phase of acicular crystals is present, mainly composed of silicon.

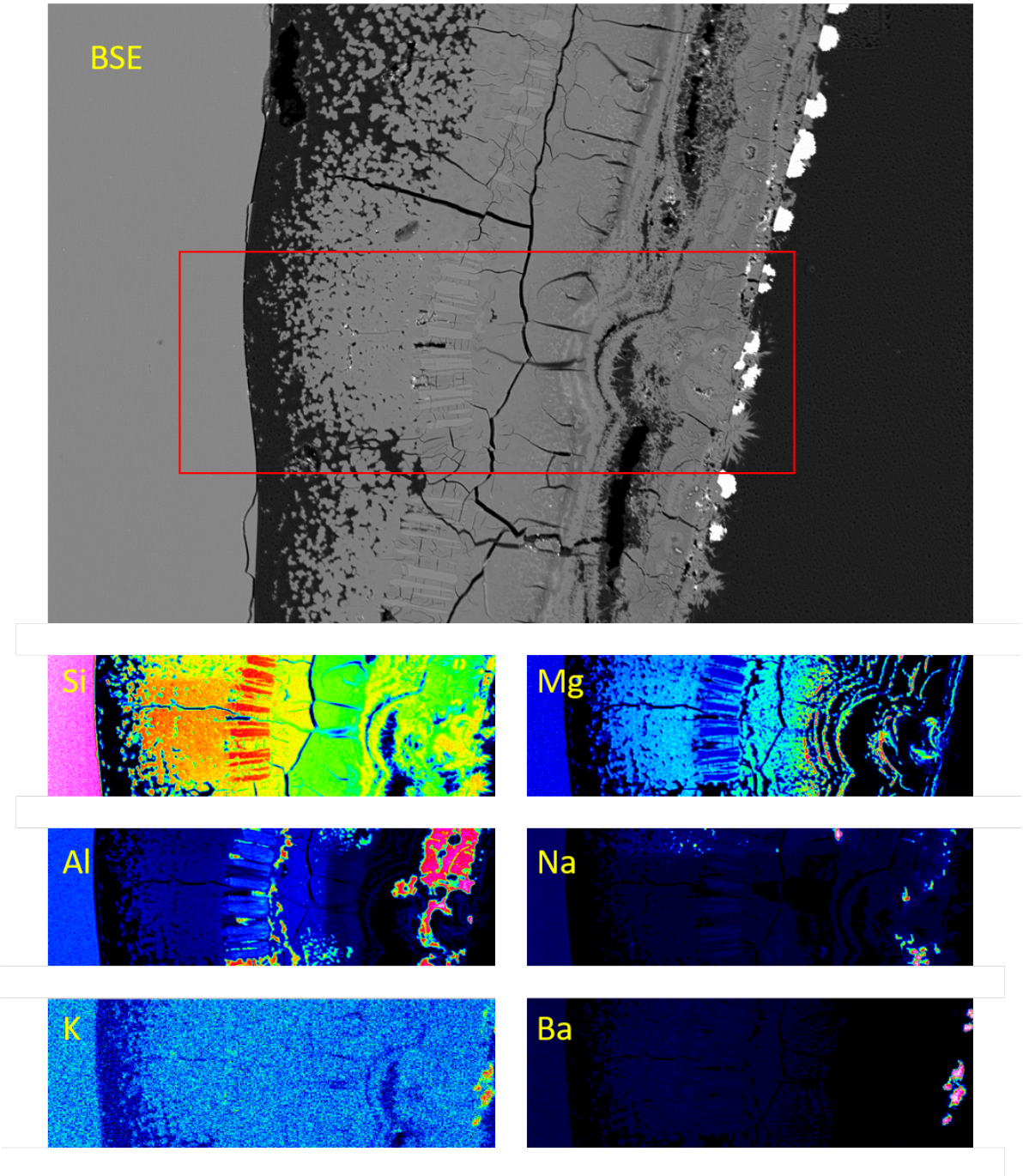

Fig. 4.2.: EMP analysis of a AR-GLAS® sample corroded for 3 weeks in alkaline solution. The backscattered electron image is shown on top, with the analyzed zone marked with a red rectangle. The six colorcoded maps displayed below are representing the element distribution of Si, Al, Na, Mg, K and Ba.

4.1.2. Solution data

The experimental run solutions for the experiments conducted in Milli-Q® were analyzed by ICP-OES. To normalize the solution chemistry to the surface area, the geometrical surface area was calculated for the tube segments as well as for the glass coupons. The results were used to calculate the surface-to-volume ratio, S/V, which allows normalizing the mass loss for an element i (NL_i) using Equation 4.1, where X_i is the fraction of the element in the glass and C_i is its concentration in solution.

$$NL_i = \frac{C_i}{X_i \times S/V} \tag{4.1}$$

The results for the Milli-Q® batch experiments were multiplied with 102 for the TBG and with 103 for the ABG and the AR-GLAS®, respectively. They basically support the conclusion drawn from the BSE images: An *in situ* corrosion experiment with the ABG will not deliver results in the timespan of 2-3 weeks, which is the maximum time for continuous use of the Raman spectrometer. The results from solution analysis are displayed in Figure 4.3. The Na concentrations in the solutions of the experiments performed at 121 °C (4.3b,d,f) were always significantly higher – by roughly one order of magnitude – than those in the experiments performed at 98 °C (Figure 4.3a,c,e).

4.2. *In situ* reaction cell

To study the corrosion of silicate glass *in situ* without the need to quench the sample, a heated fluid-cell that can be mounted on an automated x-y-z stage of a Raman microscope was designed and built with a solution in- and outlet (Figure 4.4). This setup allows the collection of Raman spectra from deep within a transparent glass sample and the surrounding solution with the laser beam parallel to the glass-water interface. As the lateral resolution is significantly better than the axial resolution, a fluid-cell geometry where the sample face of interest is oriented perpendicular to the covering lid and in line with the optical axis was necessary. Lenting (2018) conducted *in situ* experiments by drilling a blind hole in a coupon of the sample, which is then used as the lid and optical window of the fluid-cell. This leads to a high lateral resolution because the optical window has the same refractive index as the sample and there is no fluid film between the optical window and the sample. The corrosion in this setup is observed at the inner surface of the blind hole that was also filled with the respective solution. However, the polishing of the blind hole inner surface is quite challenging as well as the entire preparation process, since the glass block tends to crack while drilling.

In this work, the inner surfaces of glass tubes coming directly from production are to be investigated. Therefore, a quartz glass optical window was used as the lid of the reaction cell under which the sample was vertically fixed. A schematic illustration of the setup, a picture of the reaction cell, as well as a picture of the entire experimental setup, including the Raman

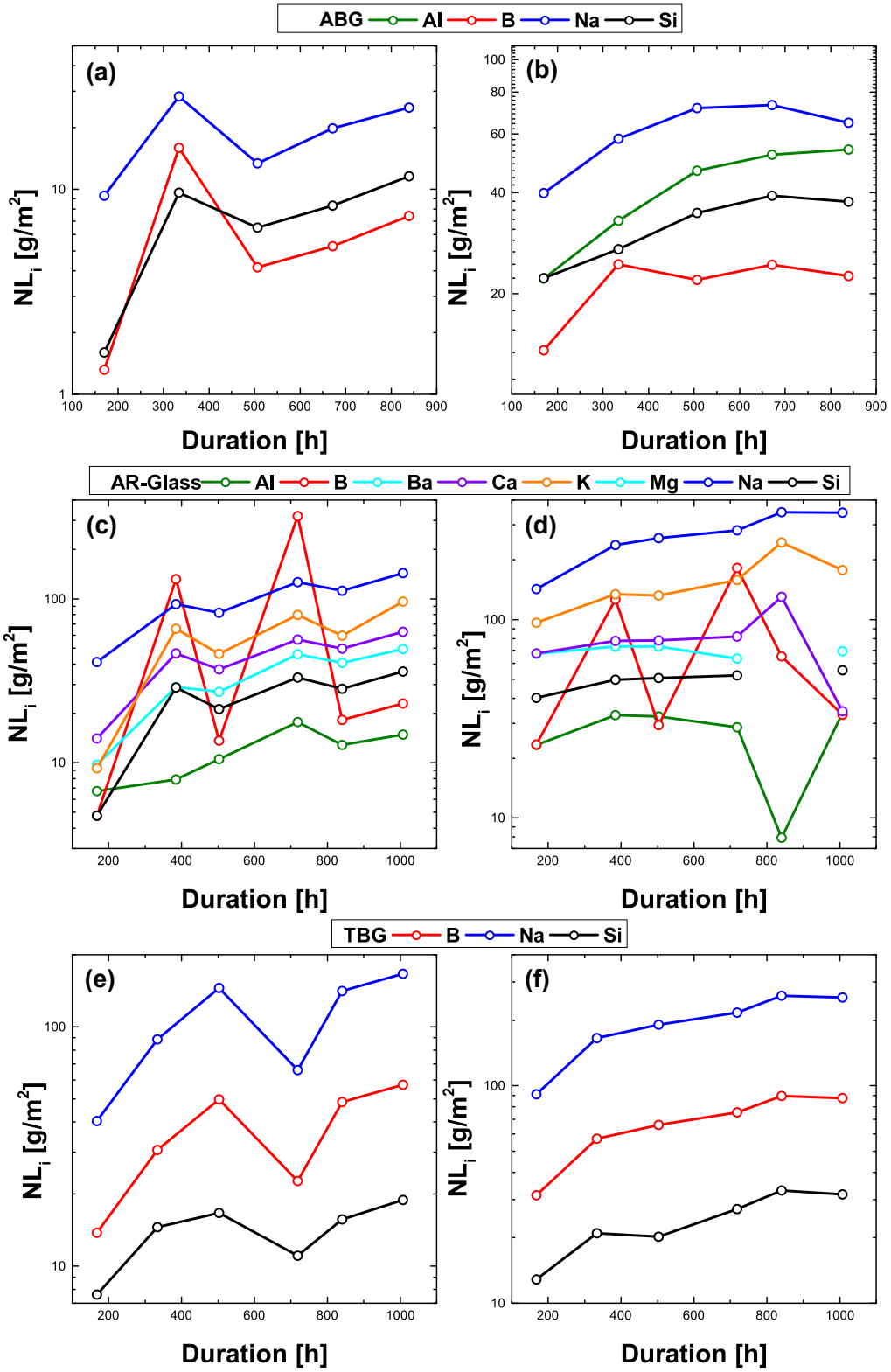

Fig. 4.3.: Normalized concentration (NL_i) of elements i released from the glasses into solution as function of experiment duration in hours. The experiments were conducted in Milli-Q® at 98 °C **(a,c,e)** and **(b,d,f)**. The results were multiplied with 10^2 for the TBG and with 10^3 for ABG and the AR-GLAS®.

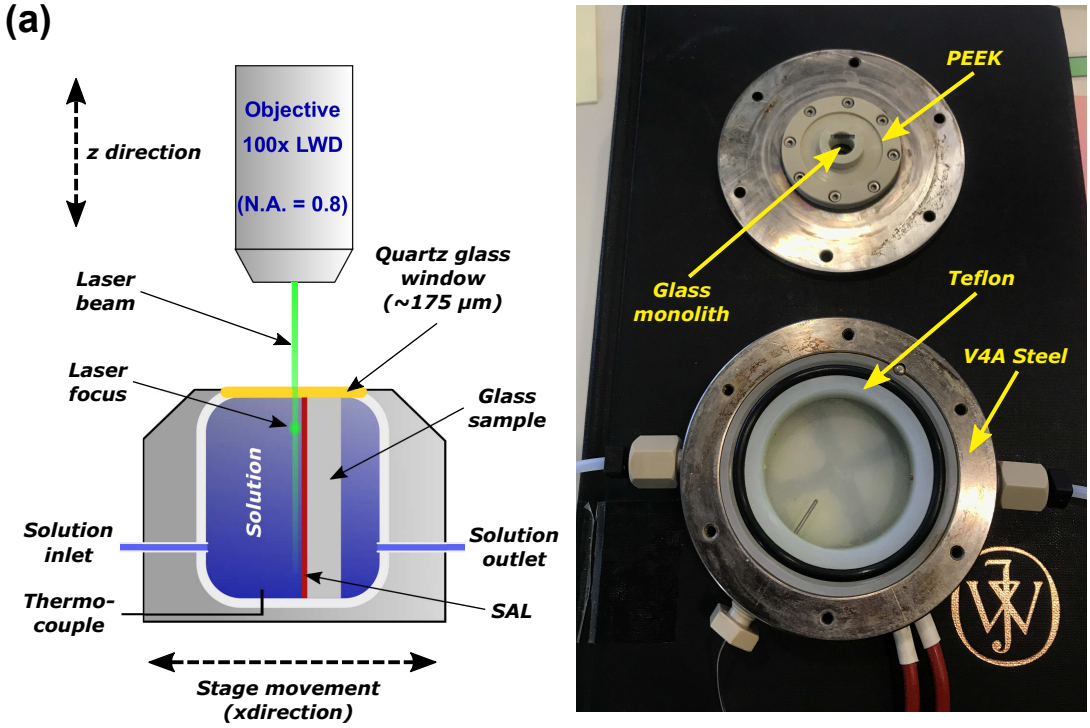

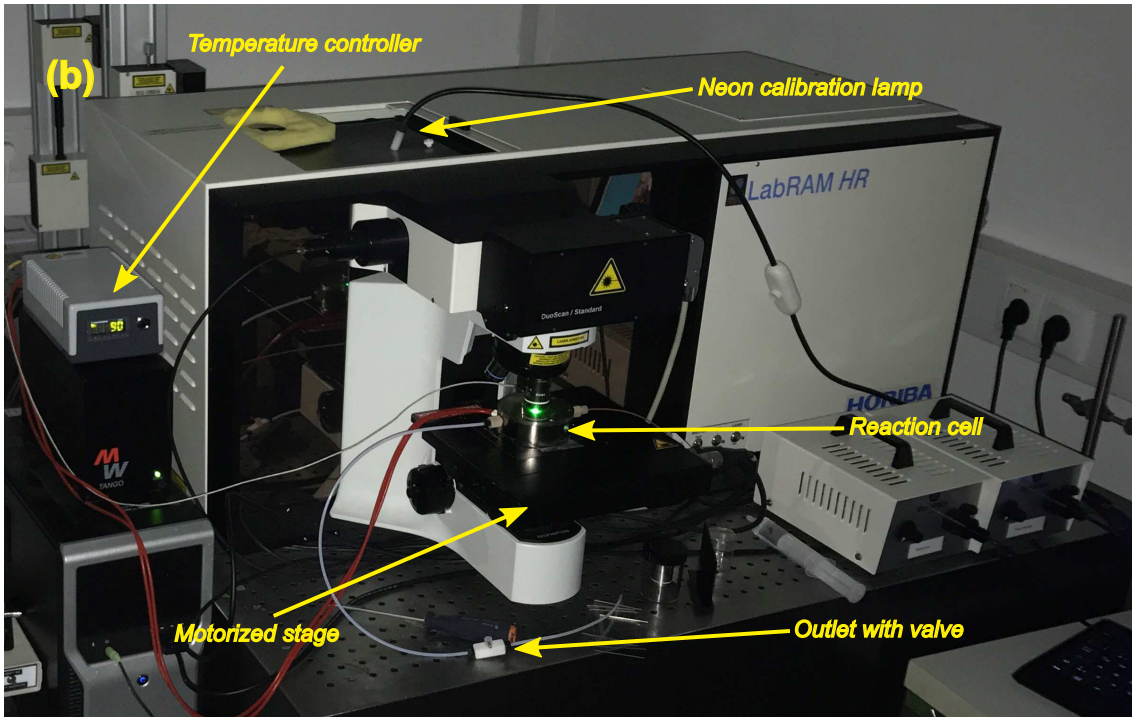

Fig. 4.4.: Schematic illustration of the *in situ* experiment with picture of the open fluid-cell **(a)**. The Laser focus lies beneath the optical window, the stage can be moved in x-y-z direction. The fluid-cell can be heated up to 150 °C and any kind of aqueous solution can be used in the Teflon® inlay. This setup enables a much better lateral resolution of the confocal microscope by mapping the fluid-glass boundary in x and y rather than in z direction. Picture of the experimental setup **(b)**.

microscope, is shown in Figure 4.4. The main task was to properly fix the sample against the gravitational pull, while avoiding the application of too much pressure on the covering lid at the same time. To realize this, there are several possibilities. For example, the sample can be glued under the optical window with a suitable adhesive. The advantage of gluing is that the sample is fixed directly under the window, with only a very thin layer of the adhesive leading to undesirable refractive effects and hence deterioration of the spatial resolution. Moreover, the presence of the adhesive can protect the sample from corrosion. The first design of the reaction cell was designed that way, i.e., only a metal ring with a hole in the middle was used to fix the optical window. The adhesive used must be highly transparent and remain stable during common corrosion procedures (Temperature: $20-120$ °C, pH $0-14$), that is, it must not lose adhesion, dissolve completely, or release components into the solution that alter the pH value or cause unwanted precipitation. Several adhesives were tested at 90 °C in an acidic (HCl, pH = 0), neutral (Milli-Q®, pH = 6.9), and basic (NaOH, pH = 14) solution for their suitability. A commercial glass adhesive from UHU® (suitable for use in dishwashers), a highly transparent silicone, and a fluoroelastomer adhesive (LEZ-VITEX) from Rexio® were tested. Unfortunately, none of the glues were proved suitable. The silicone was not stable in the basic solution, the glass adhesive led to a yellowish discoloration of the solution, and the fluoroelastomer glue did not adhere to the glass surface. For this reason, another means of attaching the sample to the optical window was used: it was clamped. To press the sample from below onto the optical window, a spring of an inert material (Teflon® or a noble metal) could have been placed at the bottom of the reaction cell. However, it can easily happen that too much force is applied to the sample, leading to ruptures of the optical window. Therefore, a metal tube with the diameter of the sample was attached to the metal ring used to seal the optical window. The glass coupon then was wrapped around the lower half of the metal tube with Teflon® sealing tape and the sample was clamped in the drilling. The fluid-cell is heated by four resistors located under the Teflon® inlay at the bottom of the cell. After the first test runs, the metal ring showed first brownish corrosion products on its surface with solution contact. A new ring consisting of PEEK® was manufactured to overcome this problem (Figure 4.5). As a part of this work, a second fluid-cell completely made of PEEK® was designed and assembled. For heating, a plate-shaped resistor was used that was placed at the bottom of the cell. As in the cell described above, the thermocouple was placed nearby the sample and a solution in- and outlet was additionally incorporated. Furthermore, a grommet was introduced to place a gold wire electrode in the solution that, together with the gold-coated thermocouple, can be used for electric impedance spectroscopic measurements as an additional *in situ* analytical tool. The cell was not used in any of the experiments reported in this work, but is currently used in a consecutive PhD project by Moritz Fritzsche.

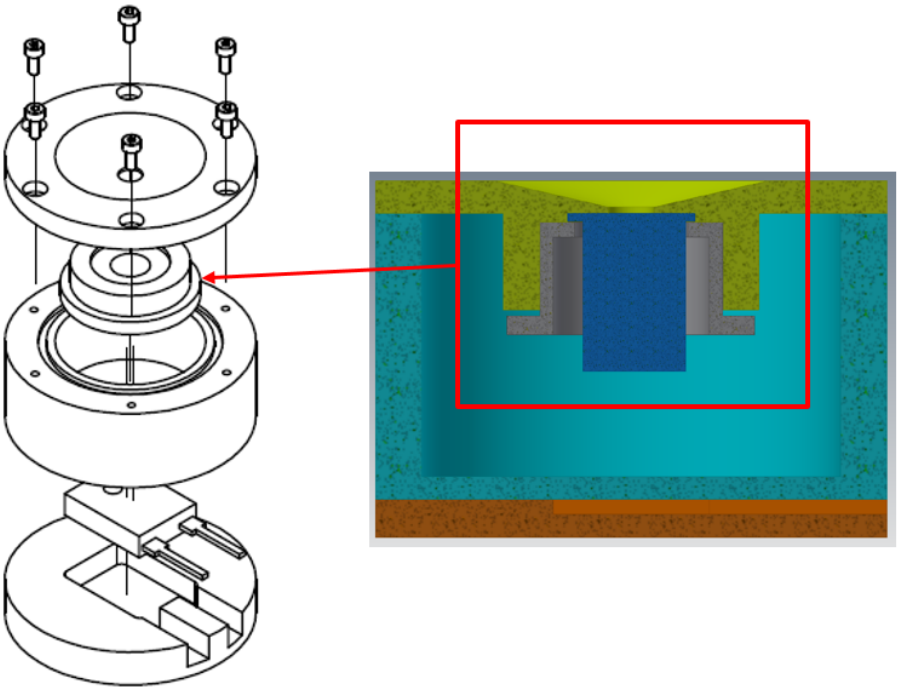

Fig. 4.5.: Technical drawing of the final fluid-cell completely made of PEEK®. The sample is displayed in dark blue in the cross-section on the right hand side.

4.2.1. Contour-plots

As described above, a setup was chosen in which the solution-glass boundary is oriented perpendicular to the optical axis. Horizontal mapping is conducted parallel to the lid, covering this boundary. Typically, point-by-point mapping comprised three lines with a length of five micrometers and 50 points each, with a distance of 2 micrometers between individual points. At every point in the mesh, a Raman spectrum was acquired, resulting in 150 spectra per map (duration ∼2 hours). In a next step, the bands of interest in the acquired spectra were integrated or fitted with a suitable peak function and the resulting intensities were displayed in an intensity distribution map (ID-map). Accordingly, there is exactly one ID-map for each time step. A suitable visualization of the entire experiment could be realized by creating a movie that allows fast-time viewing. Since this method is unsuitable for written publication, the presentation in contour plots was chosen in this work. For this type of depiction, the individual ID-maps were stacked on top of each other and plotted against time on the ordinate and the lateral position on the abscissa. An illustration of the work flow from acquisition of the Raman spectra to the generation of a contour map is shown in Figure 4.6.

The *viridis* color coding (Smith and van der Walt, 2015) was used for all contour plots. This color coding is superior to others, especially to the often used *jet* color palette, because it is also perceptible for color-blind persons. Additionally, it gives a more realistic, i.e., linear color representation of the distribution of a certain spectral feature. In a study by Liu and Heer

(2018), a persons response time and accuracy of estimating whether a random color taken from the colormap is closer to a brighter and a darker color of the same map was investigated. Both the response time and accuracy of the participants were significantly better for the *viridis* compared to the *jet* color palette.

To emphasize certain features of the contour plot, the intensity scale was adjusted in some cases. Usually the brightest color is assigned to the highest value and the darkest to the lowest value. In some cases, e.g., when intensities are plotted, the overall intensity of the maps decreases with time. This phenomenon is sometimes caused by the formation of a surface alteration layer that partly scatters the incident and scattered light along its paths. In such a case, the maximum and minimum value of the intensity scale were adjusted. All values above the manually adjusted maximum value will appear in the brightest color, while the darkest colors represent all values equal to or lower than the selected minimum value. In the case of a phase (e.g., silica gel) sharing Raman band positions with another phase (e.g., glass), the signal intensity from the glass phase, for example, can be higher than the maximum signal intensity from the silica gel. The silica gel would be invisible in the contour map. To overcome this drawback of visualization, there are two options, that are both applied in this work. One approach is to set every value behind the silica gel-glass boundary to zero. In this case, the area with zeroed values is marked with white dashed lines in the plots. The other option is to adjust the color scale to a range that fits the intensity distribution in the silica gel, in which case the glass will appear as a uniform bright area. These adjustments are not explicitly mentioned, as it is common practice in science to emphasize features which would not be visible otherwise.

All *in situ* experiments have an interrupted timeline with irregular intervals for the single maps. This is caused by the fact that the time consumed for a single mapping is not calculated properly by the operation software of the Horiba Raman spectrometer as the movement of the grating during spectral stitching is not included in the time calculation. Consequently, the next map stack was sometimes started too late, leaving a gap in the timeline. Additionally, the software sometimes crashed and had to be rebooted. In other cases, the next stack required more time per mapping, as the acquisition time was modified or the mapped area was extended. To take account for this in the contour plots, the timescale was divided into smaller segments. For example, if the acquisition of a map lasted 2.6 hours its intensity distribution was divided into 26 rows. In the case of an eight-hour gap, 80 rows were filled with zeros (see Appendix A for Matlab® Script). This way, the actual progress in time is plotted on the ordinate without the need for breaks in the axis.

In some cases, the band of interest overlaps with bands originating from glass, leading to false positive signals in the glass area. For a more realistic visualization, the glass area was cut by using the lateral positions from the glass retreat. A customized Matlab® script replaces every value above the glass retreat value (representing the glass boundary) with zeros.

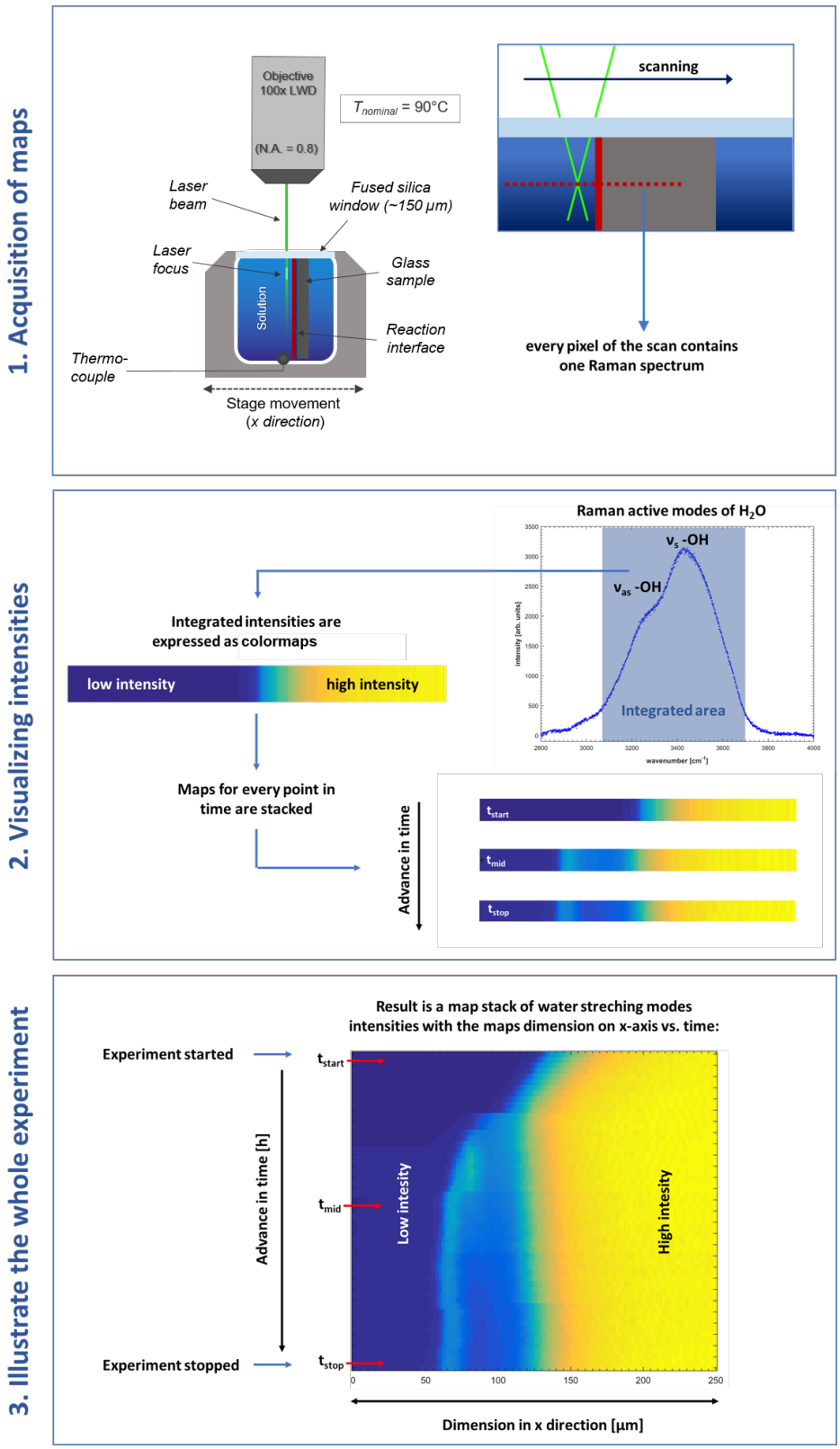

Fig. 4.6.: Schematic illustration of Raman intensity distribution maps acquisition.

4.3. Spatial resolution

The spatial resolution of the *in situ* experiments presented in this work is influenced by many factors. It is a crucial factor when drawing conclusions from the data. The principle of a confocal Raman microscope is that the scattered light is mainly collected from the focal point of the laser. This is achieved by placing a pinhole in the beam path, eliminating the out-of-focus signals and giving rise to Raman measurements with a better spatial resolution at the micrometer scale.

4.3.1. Theoretical considerations

First of all, the distinction between lateral and axial or depth resolution must be made. According to Everall (2000), the depth resolution of a light microscope is strongly variable if the position of the focal point lies in the optically denser medium. This is the case for all experiments carried out in this work and must be taken into account. An objective's focal length is given and optimized for operation in air. Figure 4.7 illustrates how the position of the focal point in the glass affects the depth resolution. When the light wave passes from the optically thinner medium to the denser one, the light is refracted and partly reflected. The difference between the focal length f and the penetration depth into the glass is referred to as Δ_1 and Δ_2. It can clearly be seen that the depth resolution Δ_d will increase with increasing Delta. Δ_d can be calculated with the following equation, where NA is the numerical aperture and n is the refractive index of the sample:

$$\Delta_d = \Delta \left[\left[\frac{NA^2(n^2-1)}{(1-NA^2)} + n^2 \right]^{\frac{1}{2}} - n \right] \tag{4.2}$$

For a typical glass with a refractive index of 1.5 and a numerical aperture of 0.8, the resulting depth resolution would be 61 µm. This means that if a measurement is carried out in 100 µm depth, Δ_d is about 61 micrometers already.
In general, the lateral resolution of an optical system, when viewing self-luminous structures, depends on the Rayleigh criterion (Kuznetsova et al., 2007), that describes the distance at which two punctiform light sources can be just perceived as two separate points. For microscopes, the lateral resolution Δ_l depends on the wavelength λ of the light and the numerical aperture of the objective NA (Equation 4.3). In this study, an objective with a NA of 0.8 and a light source with an excitation wavelength of 532.09 nm was used, resulting in a theoretically achievable lateral resolution of about 900 nm.

$$\Delta_l = 1.22 \times \frac{\lambda}{NA} \tag{4.3}$$

However, the lateral resolution for confocal measurements into optically denser media has not yet been analyzed theoretically and was therefore determined experimentally. In the

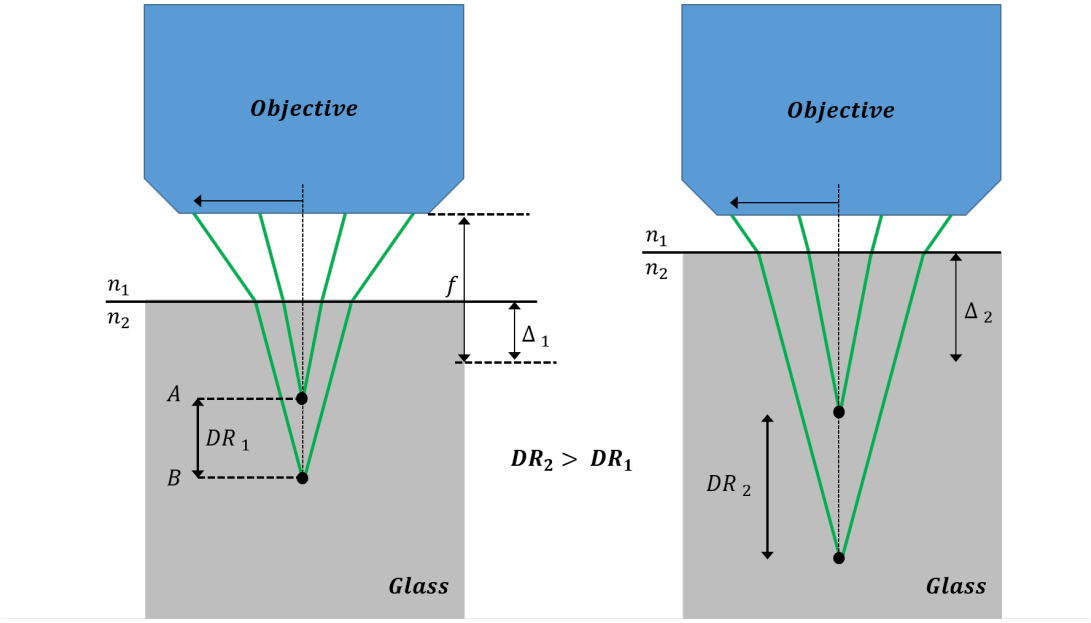

Fig. 4.7.: Schematic illustration of two measurements with the same objective in different depths of a glass sample (according to Everall (2000)). The depth resolution DR_2 is significantly poorer for a measurement in higher depths.

measurements carried out in this study, the laser beam passes through the reaction cell lid (quartz glass or sapphire), a thin layer of water and finally the glass sample itself. The same beam path applies for the Raman light scattered by the sample. Aside from the loss in intensity by reflection with each change of the medium, it is conceivable that there is also a deterioration of the lateral resolution. Typically, the optical resolution is determined by fitting a Gaussian function to the intensity distribution around a punctiform object. The full width half maximum (FWHM) of this function is used as a measure of the resolution (e.g., Gruber (1997)). In this work, however, intensity changes occur across a sharp interface between the boundary fluid and the glass. Therefore, a sigmoidally shaped function, more precisely a dose-response function (Equation 4.4), was used to fit the data. The full width half maximum and thus a measure of the lateral resolution Δ_l can be determined by calculating the x-values for ¼ and ¾ of the parameter $A_2 - A_1$ in Equation 4.4, i.e., by regarding a peak-shaped function as a sigmoidal function that is horizontally mirrored in its inflection point.

$$f(x) = A_1 + \frac{A_2 - A_1}{1 + 10^{(LOG_{x0} - x)p}} \tag{4.4}$$

4.3.2. Empirical determination

In the fluid-cell used for the experiments, the light must pass the optical window, a fluid film between it and the sample itself. At every boundary the light is refracted, which makes

the calculation of the lateral resolution difficult. Thus, the lateral resolution was empirically determined as a function of the depth of focus. A fresh TBG monolith was placed into the fluid-cell at room temperature along with distilled water and measurements were performed at different depths across the glass-water interface. As in all experiments presented herein, the optical window of the fluid-cell was a 150 µm thick fused silica disc. Since much lower integration times are required to obtain a spectrum that is adequate for intensity distribution studies, it was investigated whether the O−H stretching region can be used rather than the bands stemming from the glass. For this purpose, for the first map of experiment #6, both the integrated intensity of the Q^n bands and that of the H_2O bands were plotted and fitted with the sigmoidal function (Figure 4.8). The calculation of the resolution resulted in very similar values (21.76 µm (Q^n) and 21.42 µm (νO−H)), yet the position of the interface, represented by the inflection point of the function, differs remarkably (-5.1 µm (Q^n) and -13.42 µm (νO−H). This is caused by the different shape of the profiles, which are both not ideally described by a sigmoidal function. In particular, both profiles do not approach their maximum within the measured region. This causes the inflection point to shift towards the fitted phase.

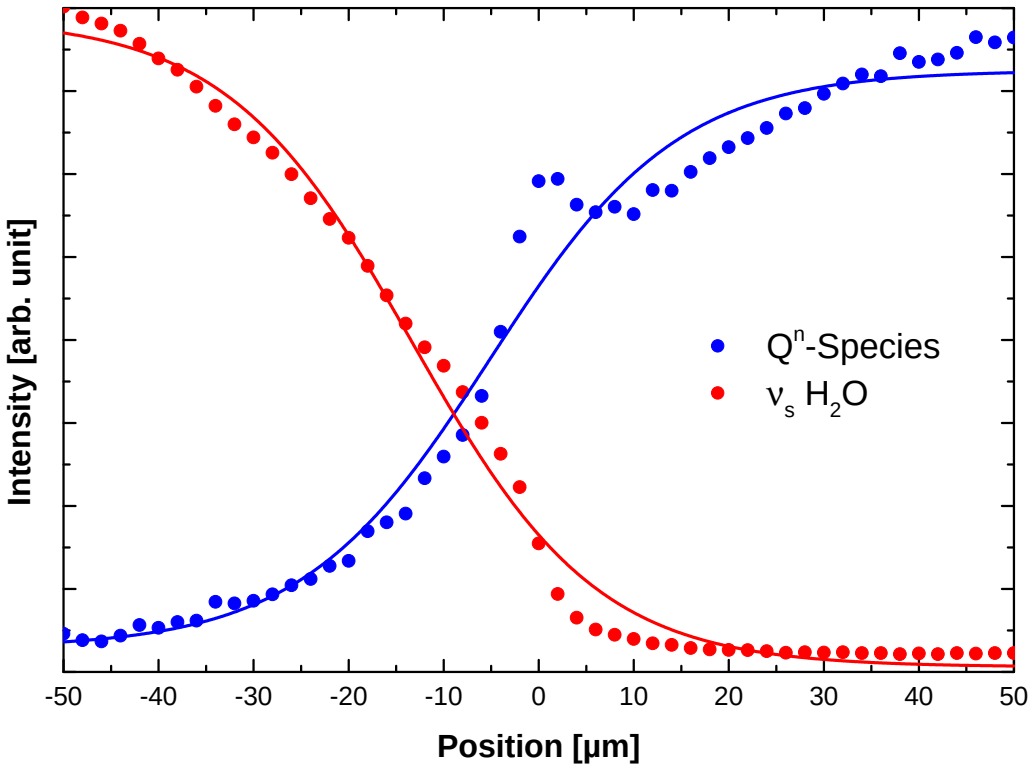

Fig. 4.8.: Sigmoidal fit of the H_2O and the Q^n-species mode intensity of the first map from *in situ* experiment #6 (cf. Table 4.3). Very similar values were determined for the resolution (21.76 µm (Q^n) and 21.42 µm (H_2O).

As mentioned above, the integrated intensity of the H_2O band across the glass-water interface (normalized between 0 and 1) describes a sigmoidal profile rather than a Heaviside step function (or unit step function), reflecting limitations of the lateral resolution. In Figure 4.9a, the integrated normalized intensity of the water mode is displayed in a contour map. Note that the depth scale represents the pathway the sample stage has moved in z-direction. As pointed out in section 4.3.1, the depth and size of the focal point is dependent on the refractory index of the optically denser medium through which the light passes. For glasses, the actual depth can be calculated by multiplying the nominal depth with the refractory index of the glass (≈1.55). Starting with a depth of 0 µm (representing the top edge of the sample), sigmoidal least-squares fitting of every horizontal dataset was performed, resulting in a resolution of about 20 µm at a nominal depth of 80 µm. However, this resolution is significantly worse than expected when looking at the contour plot shown in Figure 4.9a. Here, the glass-water interface can clearly be followed down to a nominal depth of 120 µm below the glass surface. Furthermore, the inflection points do not mark the "true" glass–water interface. A detailed look at the intensity profiles reveals a kink at ≈ 40 µm (black arrow in Figure 4.9b), where the $\nu_S(H_2O)$ intensity profiles appear to start stagnating, but then almost linearly increase with increasing distance from the glass–water interface. Therefore, a sigmoidal function was fitted to the data between x = –30 µm and x = 40 µm (red curve in Figure 4.9b). The inflection points of these fitted curves correlate well with the "true" glass–water interface and the functions yield significantly better lateral resolutions (Δl,min in Figure 4.9c) than the fits comprising the entire profiles (Δl,max in Figure 4.9c). Thus, Δl,min and Δl,max can be considered as the minimum and maximum lateral resolution. The actual *in situ* measurements were performed at a nominal depth of 80 µm below the glass surface, as dictated by the stage movement in z-direction after the laser has been optically focused onto the sample surface. However, due to refraction effects, the actual depth of focus was rather about 120 µm below the sample surface. At this depth, an empirical lateral resolution between Δl,min ≈ 6 µm and Δl,max ≈ 20 µm was determined (Figure 4.9c).

Considering only the diffraction between air and the glass sample, i.e., ignoring multiple diffraction effects along the beam path, the axial resolution was estimated to be in the order of 120 µm and 190 µm in solution ($n = 1.34$) and borosilicate glass ($n \approx 1.55$), respectively, using equation 4.2 of Everall (2000). For this reason, the sample–laser setup was arranged so the laser beam runs parallel to the glass–water reaction interface. In this arrangement, the significantly higher lateral resolution is in the direction of the reaction progress (cf. Figure 4.9a).

Furthermore, the influence of the confocal hole on the spatial resolution was investigated by executing the procedure described above with different hole sizes. With the Horiba LabRAM HR800 system, it is possible to set the size of the confocal hole in the range between 100 and 1,000 µm in diameter. As with increasing size of the pinhole the intensity of the collected Raman light increases, while the optical resolution is diminished, a significant influence on

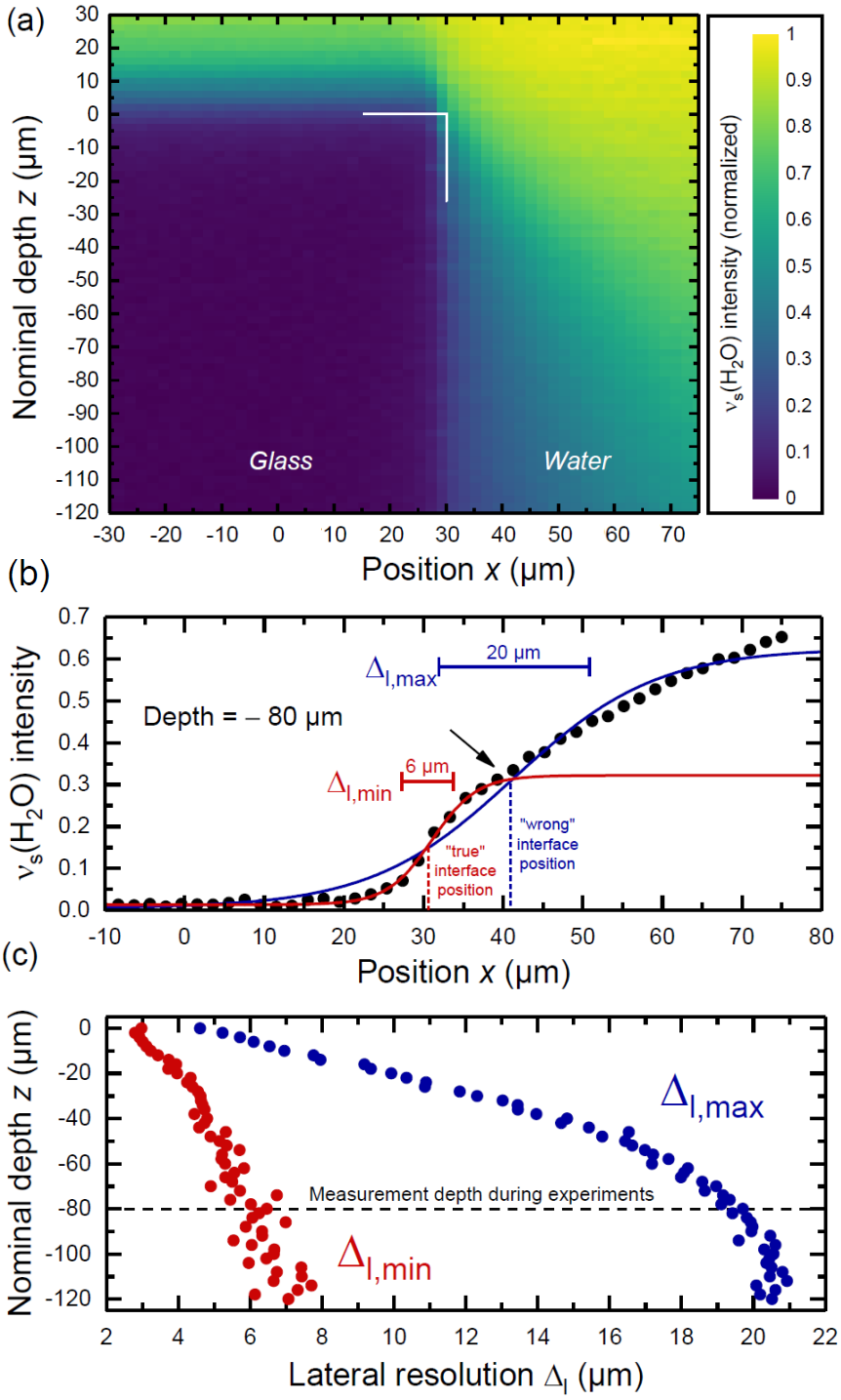

Fig. 4.9.: (a) The normalized ν_S(H2O) intensity across the glass–water interface (x direction) as a function of the nominal depth (z-direction). White lines mark the upper right corner of the sample. **(b)** The normalized ν_S(H2O) intensity across the glass–water interface at a nominal depth of 80 µm. Note the kink of the profile (black arrow) at x ≈ 40 µm. The blue and red curve represent least-squares fit of the entire profile and of the data between x = – 30 to x = 40 µm respectively (including measurements with x < -30 µm that are not shown). The latter fit describes the "true" glass–water interface and results in a much better lateral resolution (= Δl,min) than the fit using the entire x profile (= Δl,max). **(c)** The empirically determined lateral resolution Δl,min and Δl,max (b) as a function of nominal depth below the surface of the glass sample as given by the z–drive of the stage. The *in situ* measurements were taken 80 µm below the surface of the glass monolith (y = 0), yielding a lateral resolution between Δl,min ≈ 6 µm and Δl,max ≈ 20 µm. Figure taken from Geisler et al. (2019).

the spatial resolution was expected. In Figure 4.10a the lateral resolution is plotted against the depth. Below approximately 70 µm the influence of the aperture size starts to increase. Nevertheless, the largest difference in lateral resolution is 2 µm for the nominal depth of 120 µm. Counterintuitively, at this depth, the lateral resolution is better when using a confocal hole diameter of 1,000 µm instead of 200 µm. This observation can be explained by the integration time, which was the same for every map conducted with the varying pinhole size. As a result, the signal-to-noise ratio was significantly worse for the smaller pinhole diameter. Thus, fitting of the intensity profiles was poor.

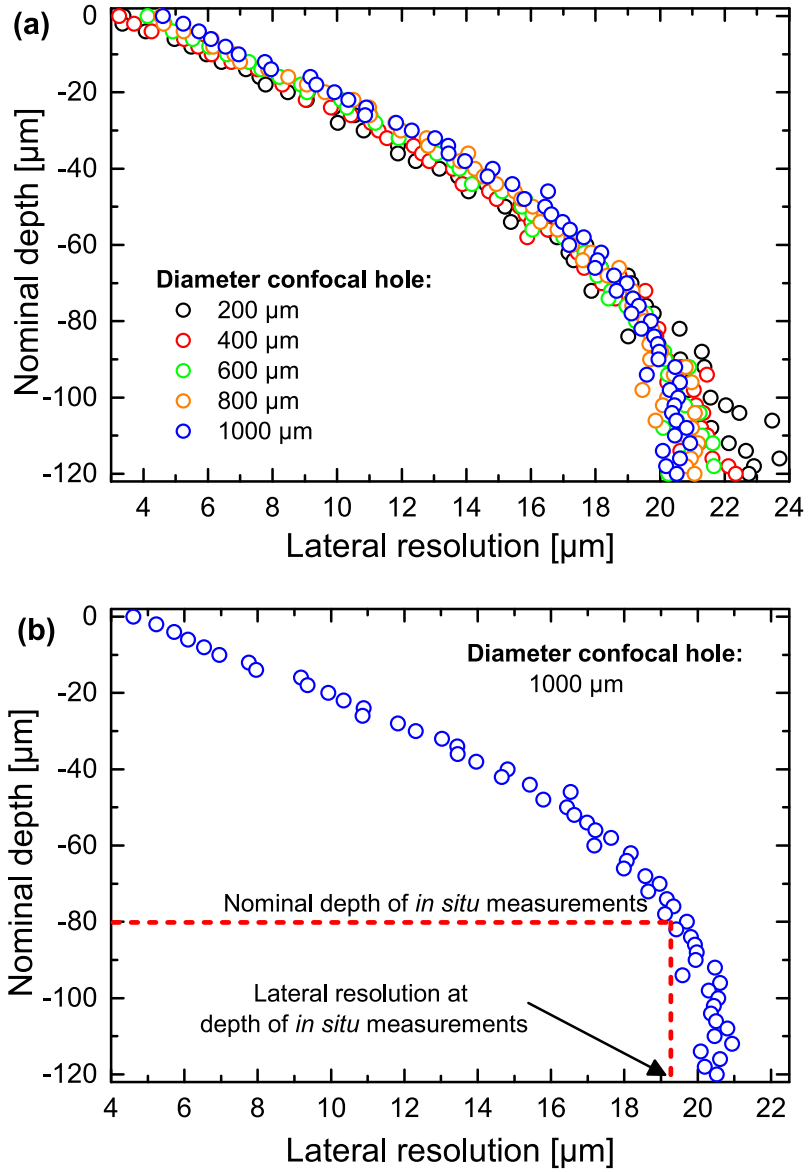

Fig. 4.10.: The empirically determined lateral resolution as a function of nominal depth below the surface of the glass sample as given by the z-drive of the stage. The data obtained with different confocal hole diameters is given in **(a)**. The *in situ* measurements (confocal hole = 1,000 µm) were performed 80 µm below the surface of the glass monolith (y = 0), yielding a lateral resolution of about 20 µm **(b)**.

4.4. Applications

The aim of this thesis is — apart from investigating the glass corrosion mechanism — to develop a methodology for *in situ* hyperspectral Raman spectroscopy and explore its limits. Most of the data and figures presented in this chapter are already published in Geisler et al. (2019). A Raman spectrum contains a vast amount of information, such as the polymerization degree of silica, the temperature or the salinity of water. Even the solution pH value can be derived via pH-dependent speciation of certain oxo-ions like phosphate, sulfate, or carbonate. As the frequency of a Raman-active vibration depends on the bond strength and the masses of the atoms involved in the vibration, hyperspectral Raman spectroscopy opens a new possibility for *in situ* isotope tracer studies.

4.4.1. Determination of glass retreat/dissolution rate

To determine the glass retreat as a function of time, the integrated intensities of the Q^n-species region (1,000 - 1,250 cm^{-1}) were extracted after subtracting the background with a 1st order polynomial. In this region, no silica bands occur and, in solution, only the comparatively weak bands of the carbonate species are present. In the case of the AR-GLAS® experiment, precipitation of calcite is observed. The mineral is a relatively strong Raman scatterer compared to the glass, with its most intense band appearing at 1,090 cm^{-1} and thus overlapping with the Q^n species region. Hence, in this particular experiment, the broad band engendered from the Danburite-like groups at 630 cm^{-1} was integrated (525 - 680 cm^{-1}). The background was subtracted by fitting a 1st order polynomial to the selected region of the spectrum.

If the lateral resolution was smaller than the step size of the measurement (2 µm), a sharp edge would appear in the intensity curve. However, due to the much larger resolution in the experiment, this sharp edge of the glass-solution interface is widened and exhibits a sigmoidal profile. In Figure 4.11a, the intensity profiles of three map stacks (separated by red dashed lines) are plotted. To locate the interface, a sigmoidal dose-response function (Equation 4.4) was fitted to the intensity profiles, as displayed in Figure 4.11b. The Märzhäuser automated sample stage is reproducible within about ± 1 µm, which is a significantly higher uncertainty than the error calculated from the sigmoidal fit (typically ranging between ± 0.2 and ± 0.9 µm).

In some experiments, the congruent dissolution of the glass was so fast that the glass/water interface moved to the edge of the mapped region or, in some cases, even out of it. In these cases, the measurement window had to be shifted in the direction of proceeding corrosion. For this reason, the full sigmoidal profile was not always recorded. To take this into account, an alternative method for determining the glass retreat was tested. The data was additionally fitted with an exponential function of the form:

$$f(x) = a \times e^{bx} + c \times e^{dx} \tag{4.5}$$

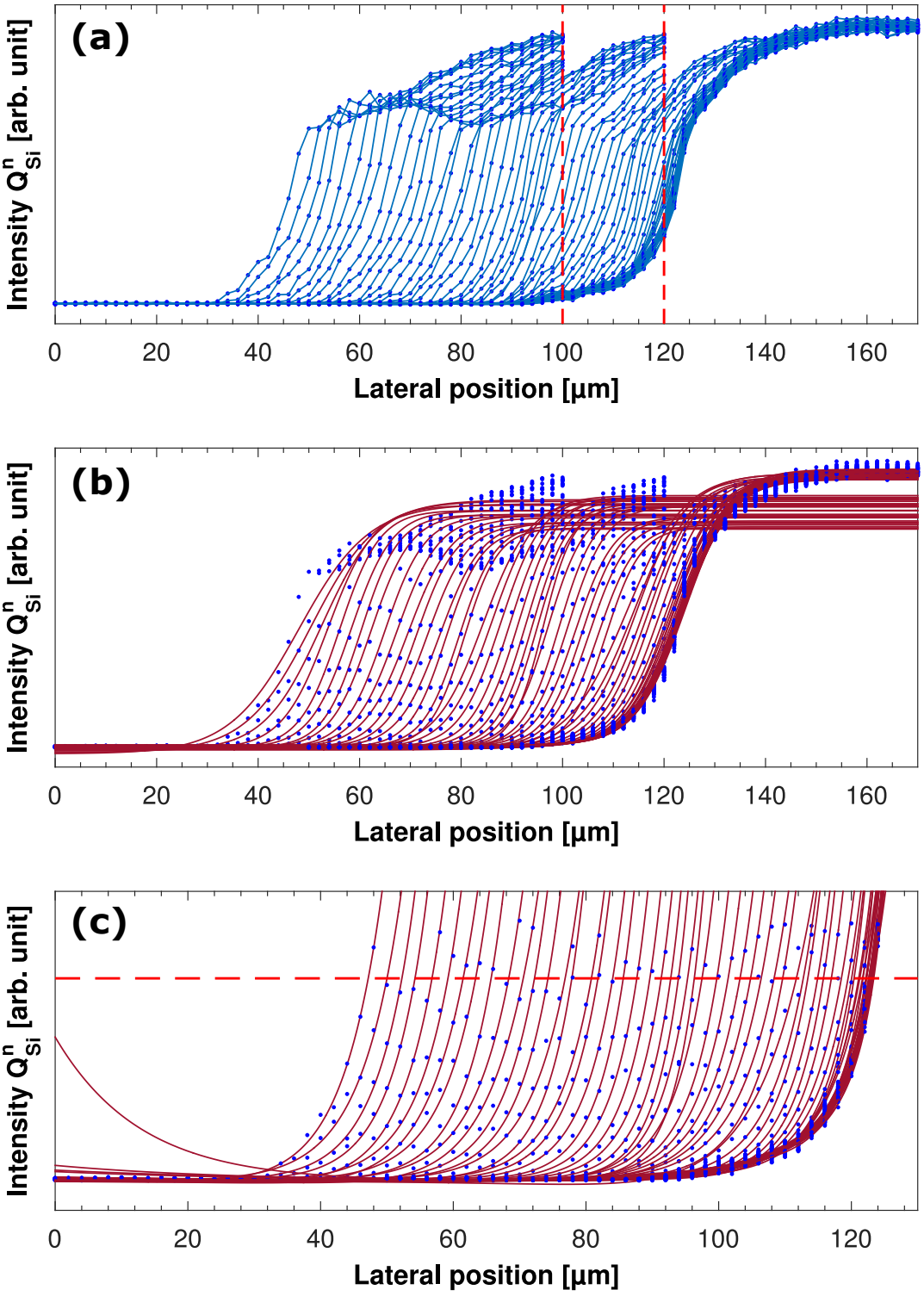

Fig. 4.11.: Demonstration of the two fitting procedure to determine the retreat of the glass. **(a)** The total integrated intensity of the Q^n species between 1,000 and 1,250 cm^{-1} as a function of position for the complete data set of the second experimental run. The three map stacks are separated by red dashed lines. **(b)** Same data as in **(a)** with sigmoidal least–squares fits. **(c)** Same data as in **(a)** (half the intensity scale), but with exponential fits. The red dashed line marks the hight where the intersections with the exponential functions are calculated. Figure taken from Geisler et al. (2019).

and then the lateral position was extracted at a given intensity (dashed red line in Figure 4.11c).

This position provides a relative measure of the progress of the glass boundary within the observed time interval, but does not necessarily reflect the "true" position of the interface, which cannot be accurately determined in this way. However, the difference between values obtained from the two fitting procedures is smaller than about 2 µm (Figure 4.12), even though a distinct difference is noticeable for the three position intervals (Figure 4.12, inset diagram). Certainly, it is evident from Figure 4.12 that the main trend for the calculated glass retreat is not significantly influenced by the way it was determined.

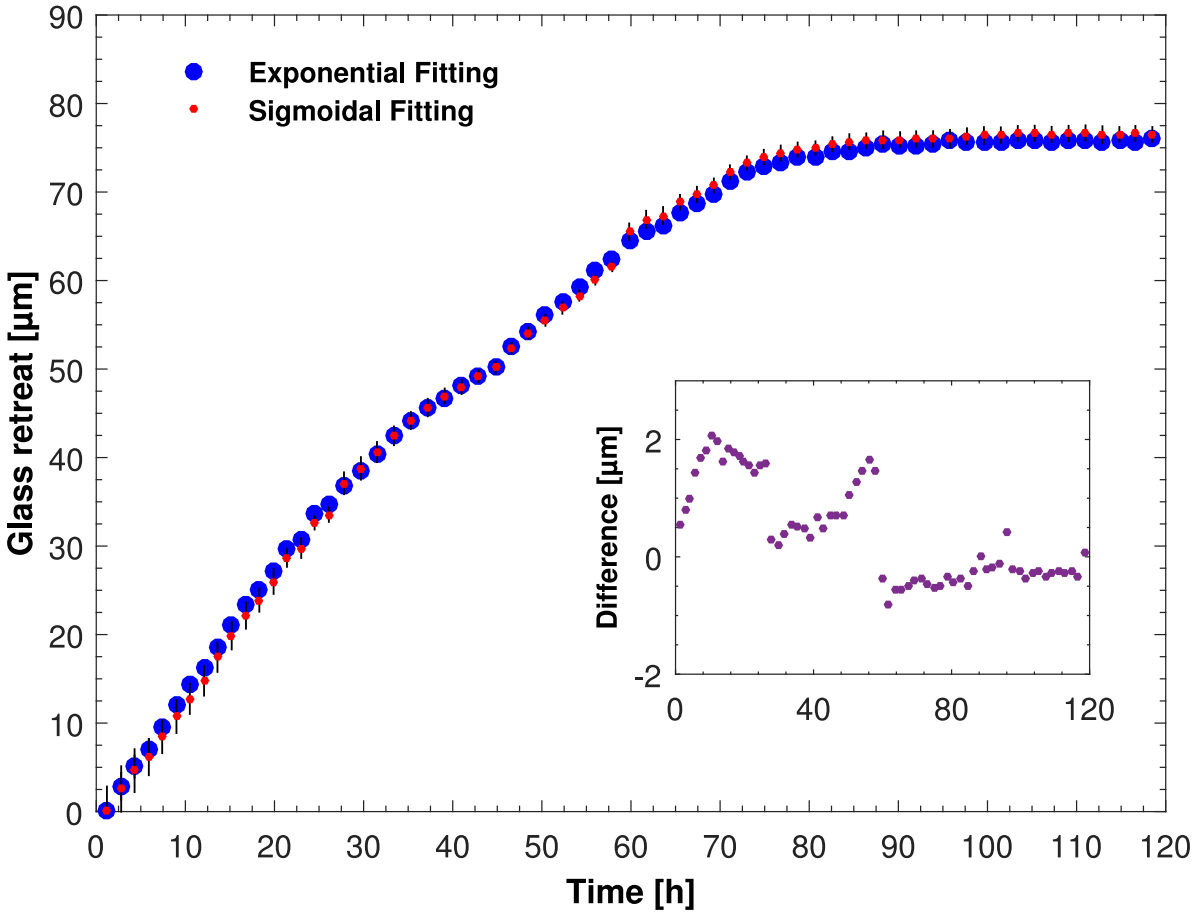

Fig. 4.12.: Glass retreat data as a function of time obtained from an exponential (blue) and sigmoidal fit (red) (see Fig. 4.11). The inset graph shows the difference of the glass retreat between the two methods. The sigmoidally fitted data are presented in Fig. 4.11a. Figure taken from Geisler et al. (2019).

4.4.2. Determination of silica ring structure parameter R_n

To study structural changes in the precipitated amorphous silica, the δ(Si–O–Si) breathing mode region between 250 and 600 cm^{-1} was used. In this region, the relatively sharp D_1 band appears near 485 cm^{-1}, which stems from the 4-fold silica ring structures (Aguiar et al., 2009).

The larger ring structures with $n = 5$ and 6 evoke broad bands at lower wavenumbers between about 350 and 420 cm^{-1}. Initially, the spectra were cut between 250 and 600 cm^{-1}. To account for the background, a linear function was fitted to the data and subtracted. Subsequently, the intensities were integrated between 250 - 460 cm^{-1}, i.e., the wavenumber region that is mainly composed of signals from the D_1 defect band and between 250 and 600 cm^{-1}, representing the total breathing mode intensity from all silica rings. Representative spectra are shown in Figure 4.13. The ratio of the two values is represented by the parameter R_n. It must be noted that R_n is not a correct quantitative measure of the actual fraction. In the absence of a detailed understanding of the silica structure and its Raman spectrum, however, R_n is an easily determinable parameter that can be used to monitor structural changes in silica as a function of time and space, which is relatively independent of the spectrum quality and physical assumptions. In the experiments presented in this work, R_n values ranged from about 0.60 to 0.76. These values obtained from silica that formed in neutral to slightly alkaline conditions can be compare with R_n values obtained from silica formed during an *in situ* experiment that was conducted at 70 ± 1 °C with a 0.1M HCl solution, i.e., at a pH of 1 (Lenting, 2018). Initially, the silica was characterized by an R_n value of 0.43. However, in this experiment R_n changes as a function of reaction time to a value of 0.67, indicating continuous aging of the silica that is accompanied by a change of the solution pH to 7.9 (at room temperature), i.e., to a pH value that is close to the initial pH of the experiments of this work. For further details and references see Section 5.1.2.

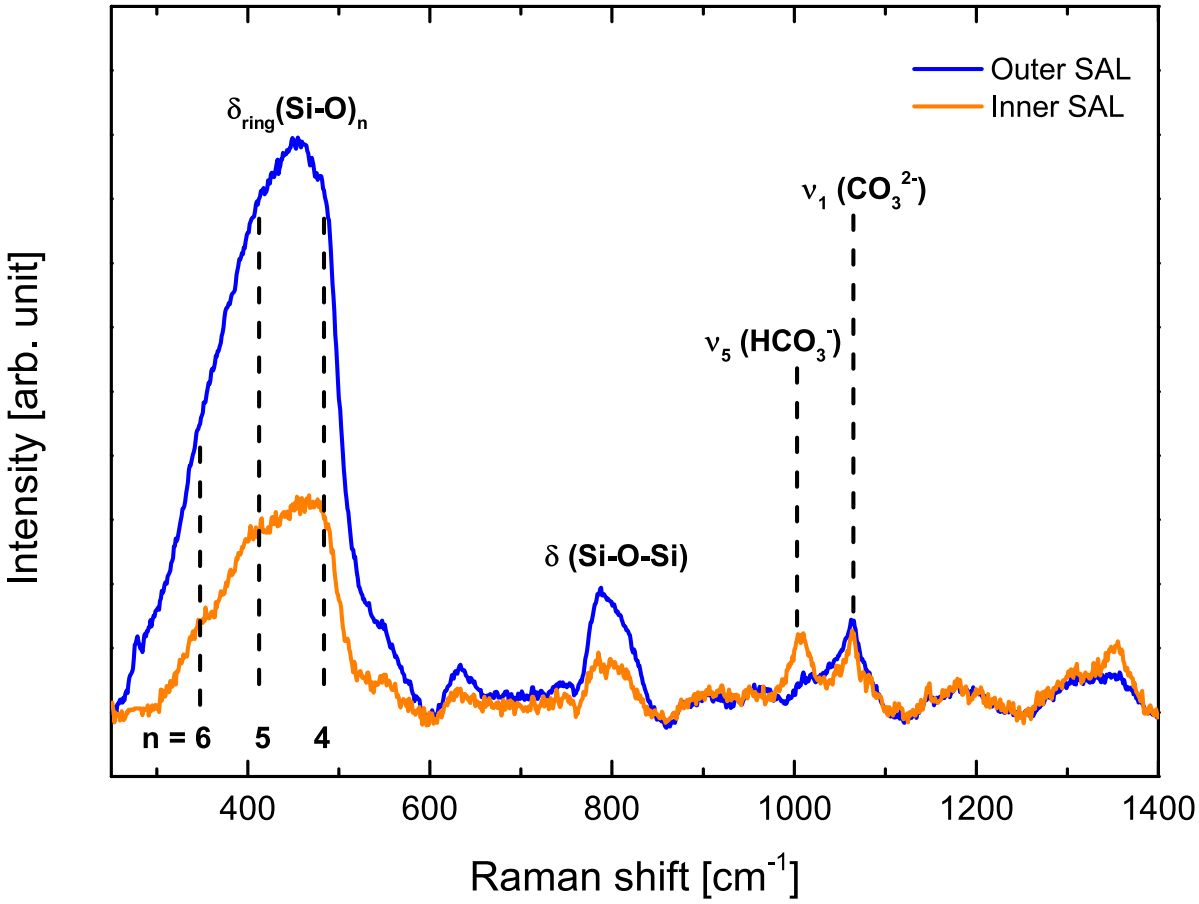

Fig. 4.13.: Representative, background-corrected, *in situ* Raman spectra from the SAL along with the assignment of the most important bands of each phase. The spectra from the SAL resemble those from amorphous silica, characterized by a broad band profile between 250 and 600 cm^{-1}, reflecting breathing modes of different $(Si–O)_n$ ring structures. Larger rings with $n > 4$ vibrate at lower frequencies than the sharper D_1 defect mode ($\sim$475 cm^{-1}) that has been assigned to breathing modes of four-fold rings ($n = 4$). The integrated intensity ratio, R_n, between 250 and 460 cm^{-1} and between 250 and 600 cm^{-1} is used in this work as a relative measure of the proportion of larger ring structures in the amorphous silica product. Note the different shape of the breathing mode profile of silica formed at two different locations within the SAL, which is reflected by different R_n values of 0.64 and 0.74 for the inner and outer SAL, respectively.

4.4.3. Temperature calibration

Although the fluid-cell is well isolated, the open arrangement of the cell towards the fused silica glass window causes a slight temperature gradient within the cell. Furthermore, the thermocouple is not located at the glass-solution interface but roughly 5 mm below it. Since the frequency of the $\nu_5(HCO_3)$ mode shifts significantly with temperature (Rudolph et al., 2008), the band position can be used to determine the temperature at any time and point within the fluid-cell. Therefore, *in situ* Raman spectra were collected from a 0.5 M $NaHCO_3$ solution at 16 different temperatures between room temperature and about 100 °C in close proximity to the thermocouple inside the cell that is accurate within ± 0.1 °C. Subsequently, the position of the $\nu_5(HCO_3)$ band maximum was determined by least-squares fitting of two Gauss-Lorentz

functions along with a linear background to the $\nu_5(HCO_3)$ and the neighbouring $\nu_1(CO_3)$ band in the wavenumber range between 950 and 1,100 cm^{-1}. In this way, a clear linear relationship of the frequency of the $\nu_5(HCO_3)$ mode with the temperature was determined (Figure 4.14) that can be best described by the following equation:

$$T(°C) = -5.939(31) \times \nu_5(HCO_3) + 6058(31) \tag{4.6}$$

Using this equation, it was possible to visualize not only the chemical properties of phases present in the system, but also the temperature as a function of time and location within the fluid-cell. In Figure 4.15, two representative contour plots of experiments #4 (a) and #6 (b) are shown, revealing some time dependent temperature fluctuations. The average of all temperature values and its standard deviation is 81.7 ± 0.1 and 85.2 ± 0.2 °C for experiment #4 and #6, respectively.

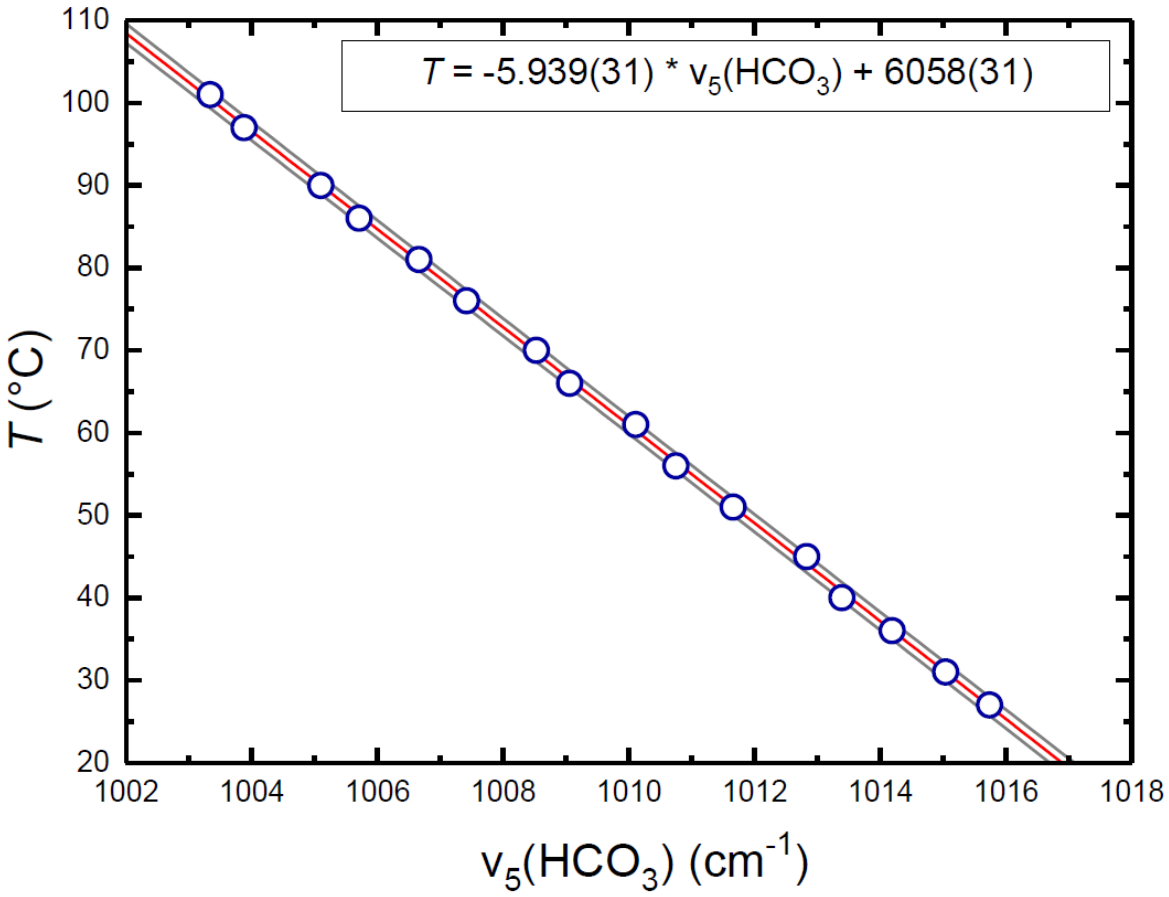

Fig. 4.14.: Solution temperature as a function of the $\nu_5(HCO_3)$ band position. The 2–sigma errors of the temperature and the $\nu_5(HCO_3)$ band position are within the symbol size. The data exhibits a linear relationship with a squared correlation coefficient of $R^2 = 0.999$, which was used to determine the solution temperature at the depth at which the Raman measurements were carried out. Confidence intervals are plotted with grey lines. Figure taken from Geisler et al. (2019).

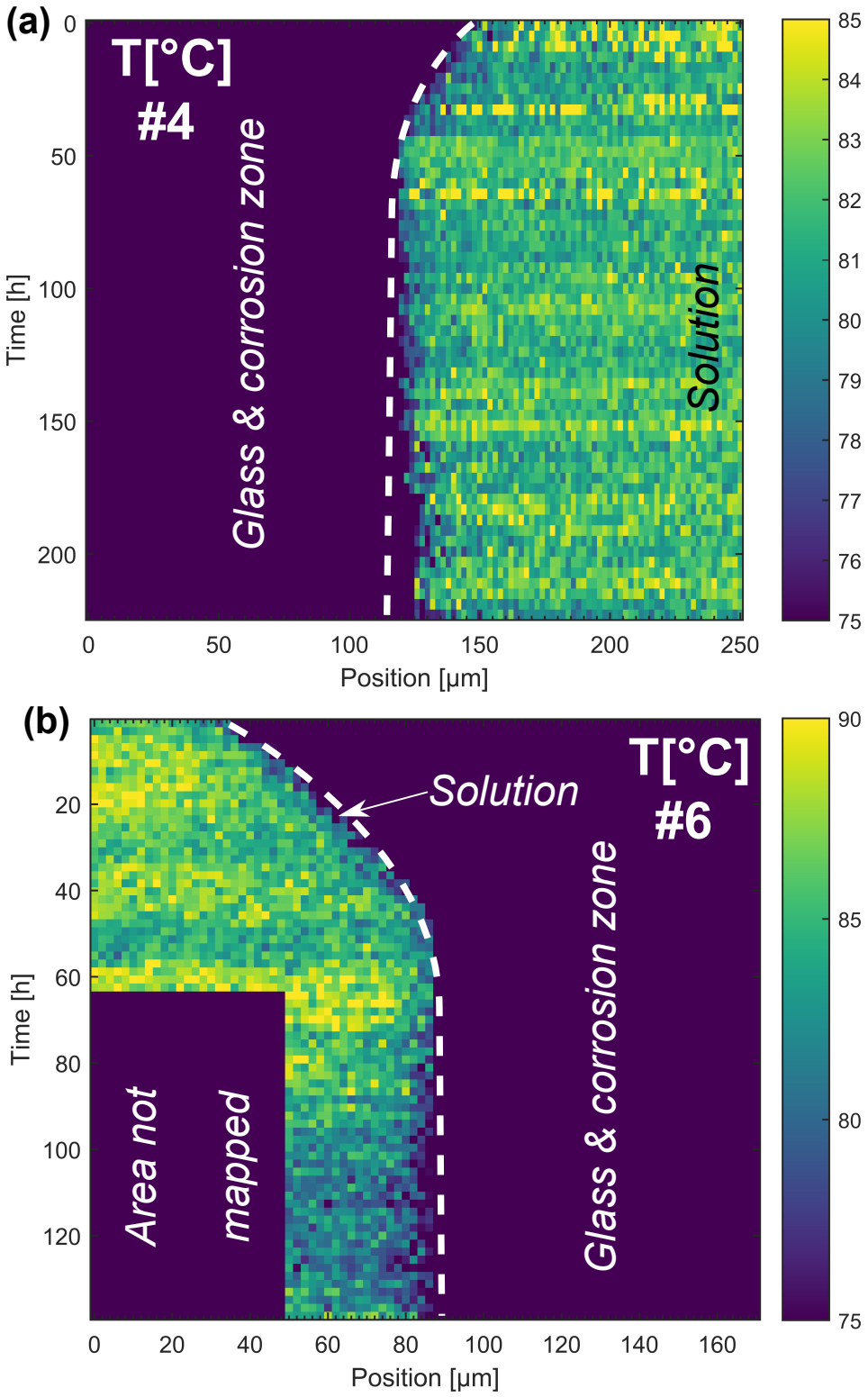

Fig. 4.15.: Temperature calibration using the $\nu_5(HCO_3)$ band position for experiment #4 **(a)** and #6 **(b)**. Plotted are the calculated temperatures at any given time for all positions inside the solution. Value in the areas not mapped, the glass and the corrosion zone are set to zero and not used for determining the average temperature and the error.

4.4.4. Monitoring the solution pH

In this study, the pH value at each point in time and space was calculated by determining the carbonate speciation in the bicarbonate solution from a Raman spectrum, which is strongly dependent on the pH value of the solution. The speciation of the carbonate system is an ideal local pH tracer for the following reasons:

- Both the bicarbonate and the carbonate ion are good Raman scatterers, producing intense bands near 1,064 and 1,006 cm^{-1} (at 85 °C), respectively.
- The reversible hydrolysis reaction $CO_3^{2-} + H_2O \longleftrightarrow HCO_3^- + OH^-$ is extremely fast (Wang et al., 2010).
- Significant changes in the carbonate speciation occur in a pH range of interest between 6 and 9.
- Both carbonate species are not involved in the glass–water reactions.

For quantitative analysis, the relative molar scattering factors (RMSF) of the $\nu_5(HCO_3)$ (J_{1016}) and the $\nu_1(CO_3)$ mode (J_{1066}) measured in a $KHCO_3$ solution at 23 °C by Rudolph and coworkers (Rudolph et al., 2008) were used. The RMSF values are 0.1667 for the bicarbonate and 0.2434 for the carbonate vibration. To determine the integrated intensity of both bands, the wavenumber region between 900 and 1,150 cm^{-1} was background-corrected by fitting a 4^{th}-order polynomial to the background signals, which was then subtracted from the spectrum. By using a 4^{th}-order polynomial function, the underlying background contribution from the glass in the spectra taken close to the glass surface was also accurately subtracted. The intensities were then integrated between 970 and 1,040 cm^{-1} for the $\nu_5(HCO_3)$ (J_{1016}) and between 1,050 and 1,075 cm^{-1} for the $\nu_1(CO_3)$ band (J_{1066}). To calculate the bicarbonate–carbonate concentration ratio from the Raman data, the ratio of the integrated intensities must be multiplied with the ratio of both RMSF values (Equation 4.7):

$$\frac{c\mathrm{HCO}_3^-}{c\mathrm{CO}_3^{2-}} = \frac{A_{1016}}{A_{1066}} \times \frac{J_{1016}}{J_{1066}} \tag{4.7}$$

To obtain the pH value from the measured $cCO_3^{2-}/cHCO_3^-$ ratios, the pH value as a function of solution speciation in the pH range of interest (pH = 6 - 9) was calculated with the geochemical code PHREEQC using the PHREEQC and SIT(specific interaction theory) databases (Parkhurst, D.L. and Appelo, C.A.J., 2013). For the experimental conditions (0.5 M $NaHCO_3$ solution at 85 °C), a pH value of 6.95 is obtained, with two bicarbonate (HCO_3^-, $Na(HCO_3)$) and two carbonate (CO_3^{2-}, $Na(CO_3^-)$) species present. The two species are summed up because both contribute equally to the respective vibrational mode intensity. The results are shown in Figure 4.16. Since the SIT theory provides better results for solutions with high

ionic strengths than the Debye–Hückel theory, the results from this database were fitted with a power function:

$$pH = 8.258 \pm 0.002 \times (\mathrm{cCO_3^{2-}/cHCO_3^-})^{0.06808 \pm 0.00009} \tag{4.8}$$

The function was then used to obtain the pH value of a solution by Raman analysis (Figure 4.16). An initial solution pH value of 7.23 ± 0.03 was obtained, which compares reasonably well with the calculated pH value of 6.95 for a 0.5 M $NaHCO_3$ solution at 85 °C. The difference may result from a temperature dependence of the RMSFs, but is considered to be insignificant with respect to any conclusions drawn in this work, which are based on relative pH changes rather than on absolute values. For determination of the pH value in a deuterated bicarbonate solution (*in situ* experiment #6), the pH value cannot be calculated in this way due to the HCO_3^--DCO_3^-–isotope exchange.

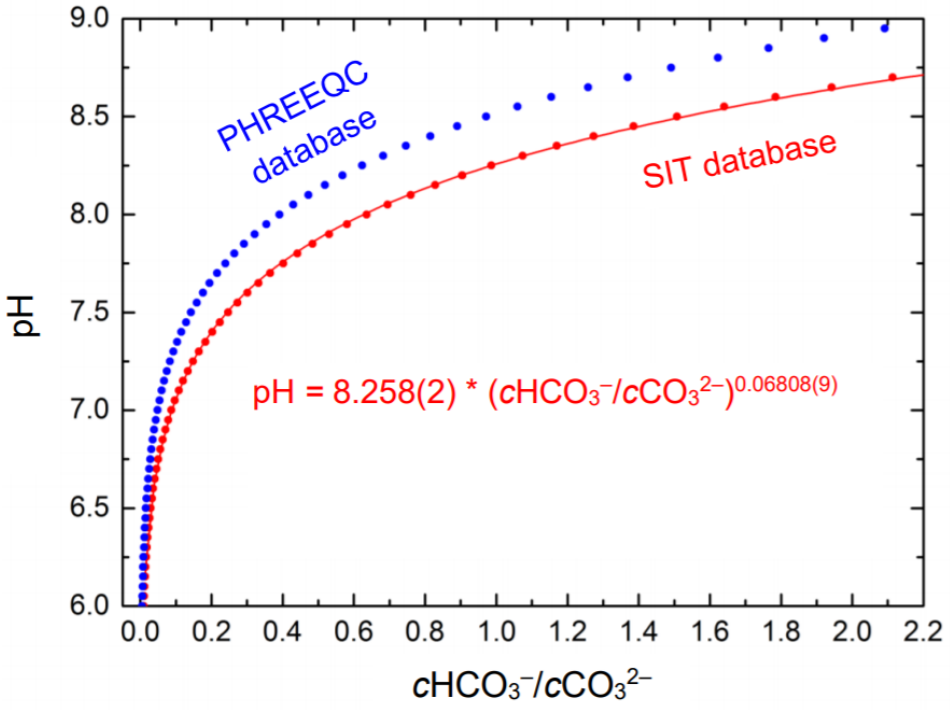

Fig. 4.16.: The pH as a function of the cCO32–/cHCO3– ratios calculated with PHREEQC using the SIT (red) and PHREEQC (blue) database. The SIT data set was fitted with a power function (R2=0.9999) and was used to calculate the pH from the cCO32–/cHCO3–ratio measured by Raman spectroscopy. Figure taken from Geisler et al. (2019).

4.4.5. Isotope tracer study

During *in situ* experiment #6, the bicarbonate solution was exchanged with a deuterated one in order to trace the water and its transport through the rim. This is possible due to the pronounced frequency shift of the O−H stretching modes by about 1,000 cm^{-1} caused by the

exchange of the proton with the heavier deuterium (cf. Figure 5.5). A series of deuterium concentration profiles from the first 7 hours after partial solution exchange was recorded and is plotted in Figure 4.17. It clearly shows that the glass surface represents a boundary for D_2O, preventing leakage of deuterium into the glass. D_2O is thus concentrated in the interface solution along the glass surface. Such a diffusion situation can be modelled reasonably well by convoluting two error functions, one of which accounts for the actual diffusion of D into the SAL and the other for the virtual diffusional loss of D into the glass (Crank, 1956):

$$cD(x,t) = 0.5cD_0 \left[erfc\left(\frac{L-x}{B}\right) + erfc\left(\frac{L+x}{B}\right)\right] \tag{4.9}$$

where cD_0 is the fraction of D_2O/OD in solution (= 0.55), i.e., in the infinite deuterium reservoir, L is the diffusion length and $B = 2\pi D_{pw}t$ with t being the diffusion time and D_{pw} the pore water diffusion coefficient. Note that this simple model neglects the (small) loss of deuterium from the pore water through the exchange with hydrogen from ≡Si–O–H surface groups and, as a first approximation, considers complex diffusion in a porous medium simply as volume diffusion. However, a reasonable empirical value for the pore water diffusion coefficient was obtained that allows the unambiguous distinction from self-diffusion of water and the diffusion velocity of hydrogen and molecular water into silicate glasses (see result section).

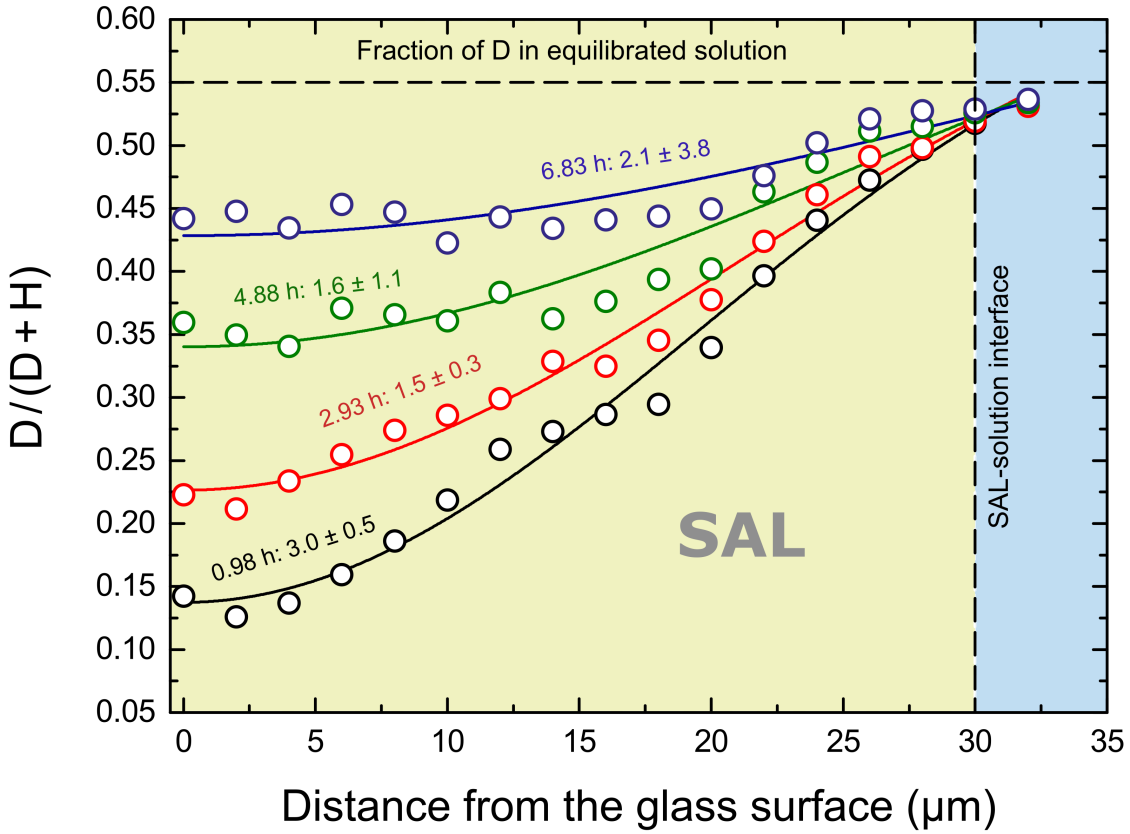

Fig. 4.17.: Deuterium diffusion(-reaction) profiles across the surface alteration layer (SAL). D/(D+H) in solution as a function of the distance from the glass–SAL interface for different reaction times after partial solution exchange with a deuterated bicarbonate solution. The pore water diffusion coefficient was determined by least-squares fitting a convolution of two error functions to the data (cf. Section 4.4.1). This function considers that D_2O piles up at the glass surface since it acts as diffusion barrier. This simple model neglects the (small) loss of deuterium from the pore water by the exchange with the hydrogen from ≡Si–O–H surface groups and, as a first approximation, considers complex diffusion in a porous medium simply like volume diffusion. However, a reasonable empirical value was obtained for the pore water diffusion coefficients that are given for each curve ($\times 10^{-14}$ m^2/s) along with the diffusion time. Figure taken from Geisler et al. (2019).

Table 4.3.: Overview over all *in situ* experiments. The lateral distance between two points of all was 2 µm for all point-by-point mappings. The nominal (T_n) and calculated (T_c) - using the bicarbonate band position - temperature is given. As solution used in the experiment #11 contains only THAM and no bicarbonate the temperature could not be calculated. If no x-y-maps were obtained, the pixel size for the line scan is the distance between two points times the lateral resolution (Δl_{lat}). Abbreviation: tris(hydroxymethyl)aminomethane (THAM)

Exp.	**Sample**	**Solution**	**pH**	$\mathbf{T}_n$	$\mathbf{T}_c$	**Image size**	**Pixel size**	**Counting time/pixel**	**Exposure time/image**	**Total duration**	$\mathbf{\Delta l_{max}}$
				[°C]	[°C]	[µm²]	[µm²]	[s]	[h]	[h]	[µm]
#1	TBG	$NaHCO_3$ 0.5 M	6.8[a]	90	98.7(5)	150 x 10	2 x 3.3	5 x 2[b] 2 x 2[c]	1.8	235	18.1
#2	AR-GLAS®	$NaHCO_3$ 0.5 M	6.9[a]	90	91.0(2)	150 x 10	2 x 3.3	6 x 2[b] 2 x 2[c]	2.4	252	8.4
#3	TBG	$NaHCO_3$ 0.5 M	6.8[a]	90	85.1(7)	150 x 10	2 x 3.3	5 x 3[b] 2 x 2[c]	2.5	150	4.3
#4	TBG	$NaHCO_3$ 0.5 M	7.0[a]	90	81.7(1)	150 x 10 180 x 10	2 x Δl_{lat}	6 x 10[b] 0.5 x 10[c]	2.5	223	10.5
#6	TBG	$NaHCO_3$ 0.5 M	6.9[a]	90	85.2(1)	150 x 10 180 x 10	2 x 3.3	6 x 2[b] 2 x 2[c]	1.6	206	13.6
#7	TBG_{irr}	$NaHCO_3$ 0.5 M	7.0[a]	90	82.6(3)	100 x 10	2 x 3.3	6 x 2[b] 2 x 2[c]	1.5	160	13.9
#8	TBG_{irr}	$NaHCO_3$ 0.5 M	7.0[a]	90	80.0(2)	100 x 10	2 x 3.3	6 x 2[b] 2 x 2[c]	1.5	87	14.3
#11	TBG	THAM 0.5 M	9.5	90	X	150 x 10 180 x 10	2 x Δl_{lat}	4 x 8[b] 2 x 8[c]	2.1	265	4.2

CHAPTER 5

Results

5.1. Raman band assignment

A large number of Raman spectra were acquired at the glass-fluid contact zone in this study, resulting in complex spectra comprising signals from the two different glasses, as well as the corrosion products forming the SAL. In addition, bands originating from the H_2O molecules occur together with bands stemming from the species dissolved in the water, e.g., bicarbonate (HCO_3^-) and carbonate (CO_3^{2-}) ions, that are subsequently used to determine the solution pH value. Raman band positions are strongly dependent on several factors, like temperature, mechanical stress or even the salinity of the surrounding solution. Therefore, for some of the assignments a wavenumber region will be given, reflecting the diversity of values found in the literature.

5.1.1. Glasses

The vibrational spectra of silicate glasses can be divided into three major domains. In the wavenumber range below 700 cm^{-1}, a broad band is present in all silicate glasses, which can be attributed to a mixture of bending and rocking vibrations of Si−O−Si angles (Kilymis et al., 2017). The most striking spectral features are the narrow defect bands D_1 (495 cm^{-1}) and D_2 (606 cm^{-1}). It is known that the intensity of these bands may vary with certain glass properties, e.g., the water content (Stolen, 1976) or mechanical stress (Walrafen et al., 1981). According to Galeener (1982) the defect bands are caused by the breathing motion of the oxygen atoms in planar ring structures (D_1: 4-fold rings, D_2: 3-fold rings). However, for some years there have been competing theories (e.g. Phillips (1984)). Later, Pasquarello and Car (1998) proved the assignment of these defect bands to the breathing motions by quantum mechanical calculations. In borosilicate glasses, the D_1 band shifts to higher wavenumbers when compared to fused silica. This can be explained by the growing boron influence on the Si/B-O-Si/B rocking and bending vibrations (Winterstein-Beckmann et al., 2014). A sharp

band occurs at approximately 630 cm^{-1}, which was assigned to the vibrations in a Danburite-like group (two Q^4 silicate and two $[BO_4]^-$ units) by Malchow et al. (2015).

In the mid-frequency range (700 - 900 cm^{-1}), only a few bands occur for borosilicate glasses. At $\sim$ 800 cm^{-1} a band appears, which originates from the cage movement of the Si−O stretching vibration. With decreasing Si content, the intensity of this band decreases and shifts to lower wavenumbers (Neuville, 2006). Other possible vibrations to occur in this region are the breathing mode of boroxol rings at 808 cm^{-1} and of AlO_4 units with one NBO (Yadav and Singh, 2015).

The high-frequency wavenumber region in silicate glasses is characterized by the vibrations of Q^n species. In order to describe the short-range order of a silicate glass, the abundance of the individual Q^n species can be used. Starting from a SiO_4 tetrahedron (Q^4), the index n indicates the number of bridge oxygens (BO). A strongly depolymerized network relative to the quartz glass, thus leads to a strong band of the Q^1 and Q^2 configuration, with Q^4 band intensity being significantly decreased. According to Malfait et al. (2008) Q^n species distribution is dependent on the network modifiers type, i.e. a direct determination of is impossible for complex compositions.

All assignments mentioned can be found in Table 5.1. A more comprehensive and detailed overview of band assignments from literature for a broad range of glass types can be found in Aguiar et al. (2009) and Yadav and Singh (2015).

Table 5.1.: Band assignment for borosilicate glasses

	Wavenumber [cm^{-1}]	**Raman assignment**
Low-freq. region	495 and 606	D_1: 4-fold rings and D_2: 3-fold rings
	400 - 600	Rocking and bending modes of Si−O−Si
	$\sim$ 630	Danburite-like group (two Q^4 silicate and two $[BO_4]^-$ units)
Mid-freq. region	779	AlO_4 or ZnO_4 units with one NBO
	808	Breathing mode of boroxol rings
	$\sim$ 800	Si−O stretching in cage
High-freq. region	900 - 1,200	Q^n_{Si} species (with increasing n bands appear at higher wavenumbers)

The Raman spectra of the glasses investigated in this study are shown in Figure 5.1. In the low-frequency region, both glasses exhibit a broad band — or rather several superimposed bands — derived from the Si−O rocking and bending modes. The band maximum is at

slightly higher wavenumbers for the alumosilicate glass AR-GLAS® than for the borosilicate glass in accordance with the literature (Yadav and Singh, 2015). Furthermore, the TBG shows a distinct band at 630 cm^{-1}, originating from the Danburite-like borate group. The band at 790 cm^{-1}, a feature in the spectrum of the AR-GLAS®, is assigned to Si−O stretching in cage. In the high-frequency region, the spectrum of the AR-GLAS® has a pronounced band at 1,093 cm^{-1}. Winterstein-Beckmann et al. (2014) examined a chemically similar glass and found a very high Q^3 content (70%). Thus, they assigned the bands at 1,095 and 950 cm^{-1} to the Q^3 and Q^2 species, respectively. This also explains the displacement of the broad band in the low frequency range, since the bending vibrations of Si−O−Si connected to Q^3 and Q^2 units generate bands at 545 cm^{-1} and 600 cm^{-1}. In the case of TBG, the Q^3 band occurs at 1,060 cm^{-1} and the Q^4 band at 1,150 cm^{-1}. The Q^2 band, which should appear at 950 cm^{-1}, is almost not visible. It is most likely hidden in the left flank of the Q^3 band (Osipov et al., 2013; Stavrou et al., 2014).

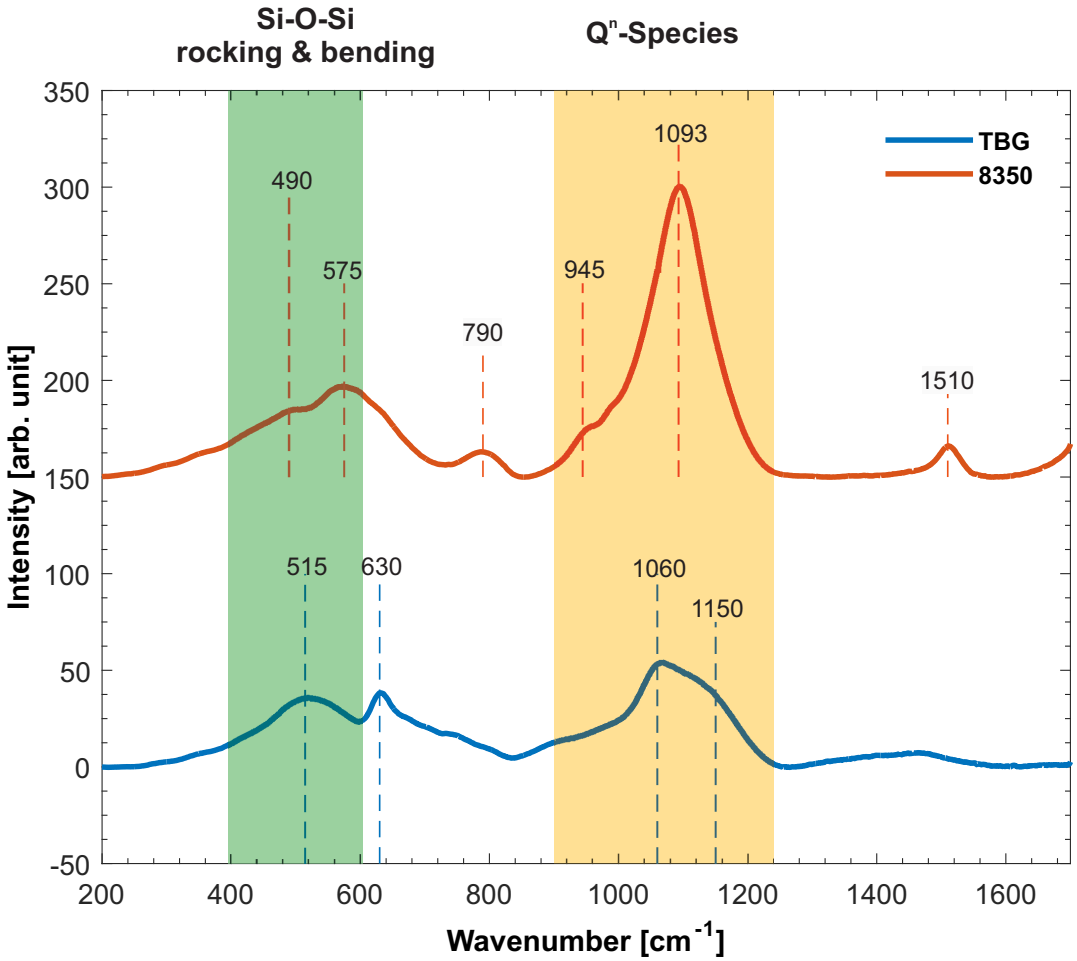

Fig. 5.1.: Raman spectra of the two glasses examined in this thesis. Homemade ternary borosilicate glass (TBG) and AR-GLAS® tube (8350). Spectra are corrected with Equation 3.1. Regions of prominent vibrations are marked in green and yellow, respectively. Band positions are marked with dashed lines and are discussed in text.

5.1.2. Precipitated phases

In this study, *in situ* experiments were carried out in aqueous alkaline solution ($NaHCO_3$ solution). Lenting (2018) performed similar experiments in acidic solution (1M HCl). In both studies, the observed corrosion products were silica gels. Even though the same glass (TBG) was used, the obtained silica gel Raman spectra differ notably (Figure 5.2). For simplicity, the gel precipitated under alkaline and acidic conditions will be referred to as $SiGel_{alk}$ and $SiGel_{ac}$, respectively.

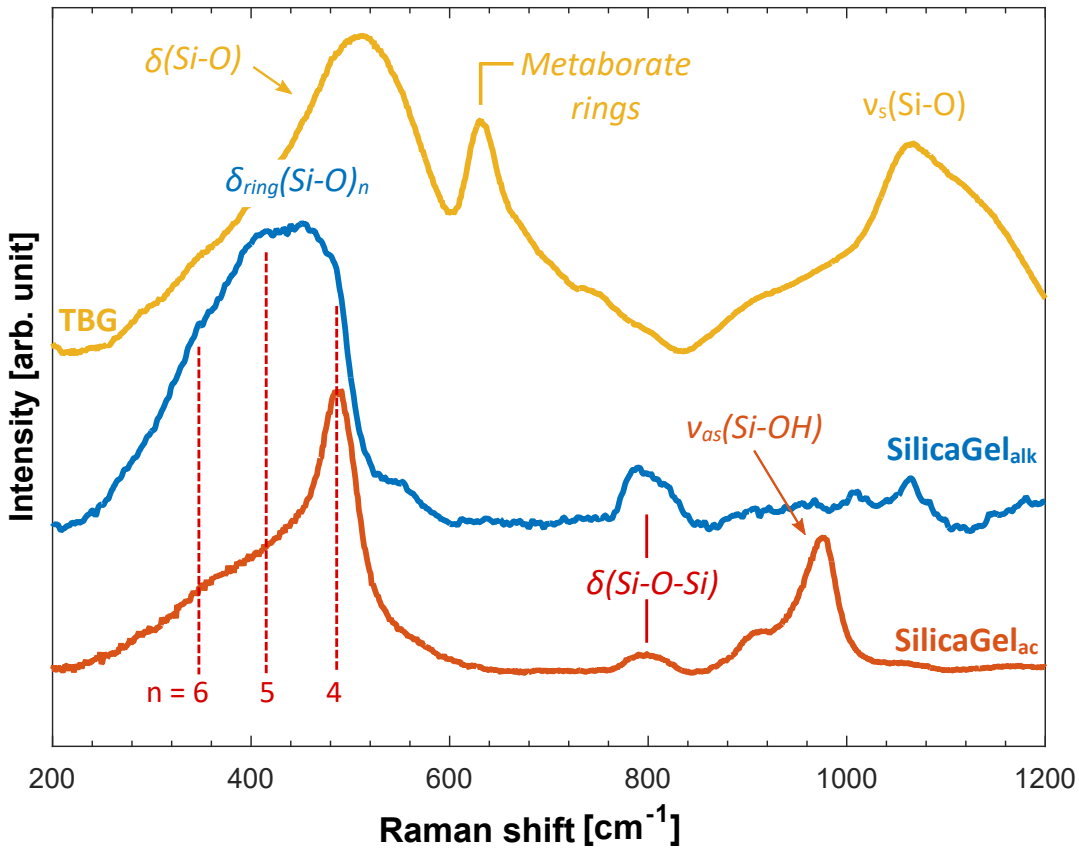

Fig. 5.2.: Silica gel Raman spectra observed in alkaline (blue) and acidic (orange) conditions. In light yellow, the spectrum of the TBG is displayed for comparison. The background was subtracted with a 3rd-order polynomial for all spectra. The D_1 band at 490 cm^{-1} is engendered by the silica ring breathing ($\delta_{ring}(Si{-}O)_n$) with $n = 4$. The bands correlating to larger ring structure ($n = 5$ and 6, marked with red dashed lines) are located at lower wavenumbers. Note that the Spectrum for $SiGel_{ac}$ differs significantly from the spectrum for the $SiGel_{alk}$ in this region, which means that fewer larger ring structures with $n > 4$ are present in the $SiGel_{ac}$. In this study the parameter R_n is introduced to asses these differences in ring structure size (cf. Section 4.4.2). Furthermore, the $SiGel_{ac}$ features a prominent band at ~975 cm^{-1} originated by the asymmetric stretching of Si−OH.

Both silica gels feature a band at about 800 cm^{-1}, which is more pronounced in the $SiGel_{alk}$ spectrum and can be assigned to the Si−OH symmetric stretching vibrations (Chemtob et al., 2012). In both spectra, a band appears near 487 cm^{-1}, which can be attributed to the respiration mode of planar 4-fold rings, often referred to as the D_1 defect band that is also observed in silicate glasses (Aguiar et al. (2009), Section 5.1.1). Rings with five members or

more are denoted as ω_1 and their bands are visible at lower wavenumbers (Brinker and Scherer, 1990). These bands are all engendered from the $\delta_{ring}(\mathrm{Si{-}O{-}Si})_n$ vibration, with $n = 5$ at 422 cm^{-1} and $n = 6$ at 350 cm^{-1} (red dashed lines in Figure 5.2). In this study, the parameter R_n is introduced to asses these differences in the ring structure size (cf. Section 4.4.2). Chemtob et al. (2012) investigated three samples of amorphous silica with different water contents. The intensity of the broad left shoulder of the ring breathing modes frequencies at 487 and 422 cm^{-1} evidently correlates with the water content (cf. blue arrows in Figure 5.3).

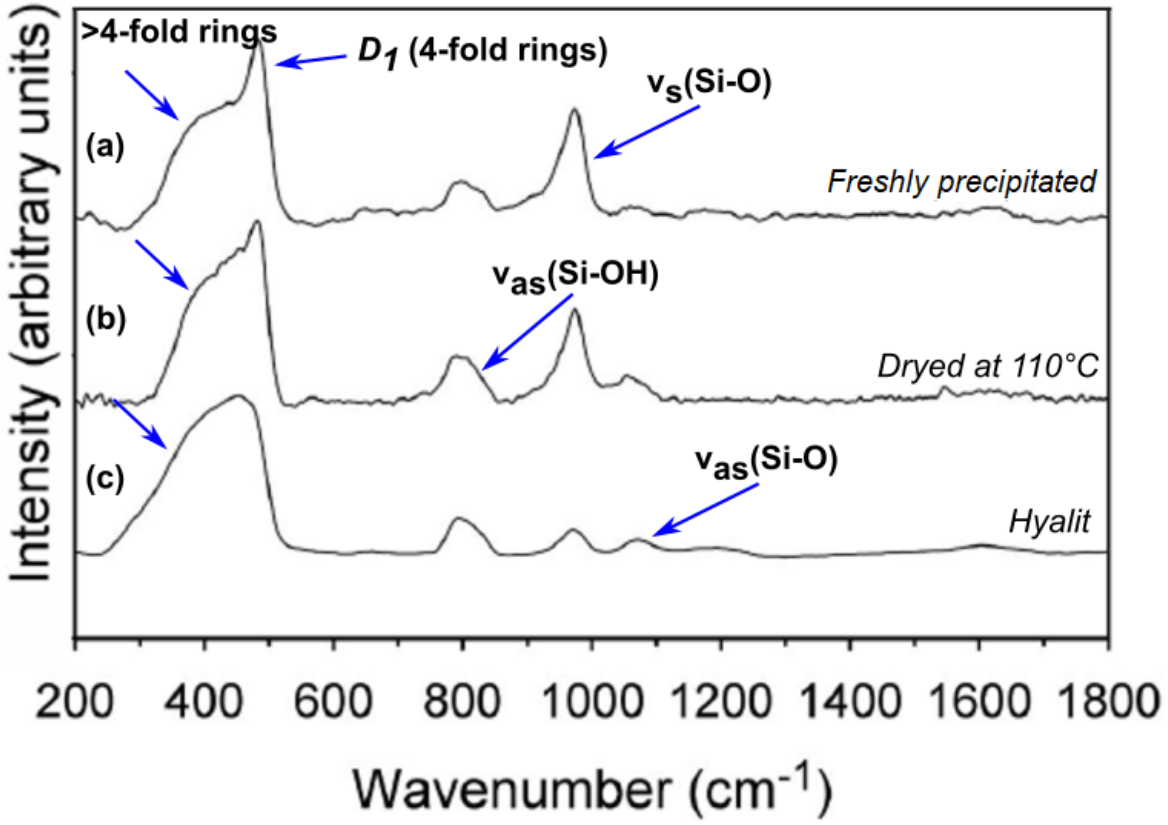

Fig. 5.3.: Spectra of amorphous silica with different water content modified after Chemtob et al. (2012). Spectrum **(a)** is obtained from a silica gel precipitated from a saturated basic solution by adding HCl and spectrum **(b)** from the dried gel (110 °C). Spectrum **(c)** stems from a glass-clear Hyalit, typically containing 3-8% of water.

An intense band can be observed at about 970 cm^{-1} only in the spectrum of SiGel_{ac}, which proposedly originates from the Si−(OH) stretching in a Q^3 tetrahedron (Stolen, 1976). A less intense band is visible in the left shoulder that was assigned to the stretching of $=\mathrm{Si{-}(OH)_2}$ in Q^2 species (Krol and van Lierop, 1984). Spiekermann et al. (2012) calculated vibrational mode frequencies of silica species in water. The authors argue that their results do not confirm the origin of the 970 cm^{-1} band proposed by (Stolen, 1976), because of another study that described the presence of Q^2-units in hydrous silicate glass. This means that the asymmetric

stretching of a Q^2 tetrahedron may be the cause of the band. However, in the same study the single ν(Si−OH) stretching for Q^0-units frequency was calculated to be 915 cm^{-1}, at which frequency a band is visible in the spectrum of $SiGel_{ac}$. At 630 cm^{-1}, in the spectrum of $SiGel_{alk}$, a weak band is vaguely perceptible, which may stem from the mixed rocking δ(Si-BO-Si) and stretching ν(Si-BO) in the dissolved pyrosilicic acid, $H_6Si_2O_7$ (Zotov and Keppler, 2000, 2002), or, more likely, from the Danburite-like groups mentioned above.

During the *in situ* experiment with the AR-GLAS® (#12), precipitation of calcite ($Ca[CO_3]$) was observed. The corresponding spectrum is shown in Figure 5.4. In the low frequency range at ∼160 and 280 cm^{-1}, the bands originating from the translational lattice modes are visible (Gunasekaran et al., 2006). The carbonate anion produces a pronounced band at roughly 1090 cm^{-1}, stemming from the symmetric stretching (ν_1) of the $[CO_3]$ group (Gunasekaran et al., 2006). The weak $\nu_3(CO_3)$ band from the asymmetric stretching mode of the $[CO_3]$ group near 1,440 cm^{-1} (Buzgar and Apopei, 2009) was not observed in the spectra obtained in this study. The observed band at 715 cm^{-1} can be assigned to the asymmetric bending (ν_4) of the $[CO_3]$ group (Buzgar and Apopei, 2009).

In the experiment, another band is discernible near the ν_4 band at ∼680 cm^{-1}. At first, it seemed appropriate to assign this band to an additional carbonate phase, like witherite ($Ba[CO_3]$), or to a solid solution, like barytocalcite ($BaCa(CO_3)_2$), both showing a double band in this wavenumber region (Buzgar and Apopei, 2009; Frost and Dickfos, 2008). This band, however, was only visible in the spectra from the outer part of the corrosion zone (solution side) and it was found that its appearance was coupled to the emergence of a sharp hydroxide band in the O−H stretching region. Most likely, it stems from a C-S-H phase, with an intense band at exactly 680 cm^{-1} engendered by the δ(Si−O−Si) mode (Ortaboy et al., 2017). Calcium silicate hydrate phases barely occure in nature but are an important component in cement systems. Notably, C-S-H phases are known to precipitate in a sol-gel process from glass precursors in hydrothermal experiments (Krassimir Garbev, 2004). However, only one band is visible in the spectrum. Other bands of C-S-H phases occur in the (ν_1) stretching region of the $[CO_3]$ group and may thus be superimposed by the intense calcite bands.

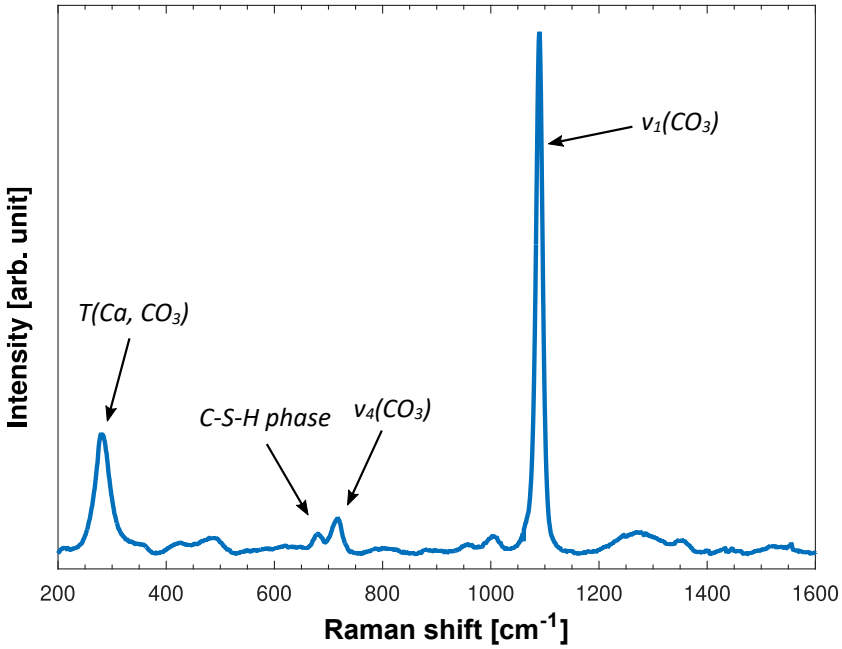

Fig. 5.4.: Spectrum of calcite precipitated during *in situ* experiment #2. Two bands appear for the asymmetric bending (ν_4), most likely reflecting the formation of a calcite/witherite solid solution called barytocalcite ($BaCa(CO_3)_2$).

Table 5.2.: Band assignment for corrosion products. The table is divided into two parts. The assignment for the silica gel can be found in the upper part and for the carbonate phase in the lower part, respectively.

Wavenumber [cm^{-1}]	**Raman assignment**
482 - 488	D_1: 4-fold rings ($\delta_{ring}(Si{-}O)_n$ with $n = 4$)
$\sim$ 300 - 480	>4-fold ring ($\delta_{ring}(Si{-}O)_n$ with $n = 5$ and 6)
$\sim$ 630	Mixed $\delta(Si{-}BO{-}Si)$ and $\nu(Si{-}BO)$ of dissolved pyrosilisic acid or danburite-like groups
793 - 796	Si-O symmetric stretching
972 - 978	Si-OH asymmetric stretching
1,068 - 1,074	Si-O asymmetric stretch
$\sim$ 160 and 280	Carbonate translational lattice modes
~680	$\delta(Si{-}O{-}Si)$ of C-S-H phases
715	Asymmetric bending (ν_4) of the CO_3 group
1,090	Symmetric stretching (ν_1) of the CO_3 group
~1,440	Asymmetric stretching of the CO_3 group

5.1.3. Aqueous solution

All experiments were carried out in aqueous solution, i.e., all modes of the H_2O molecule are expected to be observed. Water bands occur in the low frequency region (200 - 1,700 cm^{-1}) as well as at higher wavenumbers (3,000 - 3,800 cm^{-1}). In addition, Raman bands of solute species were observed. In this study, the used buffers were sodium hydrogencarbonate and tris(hydroxymethyl)-aminomethane ($C(CH_2OH)_3NH_2$), referred to as THAM in the following. Representative spectra from solutions are displayed in Figure 5.5.

For liquid water, the band assignments found in the literature are manifold. All authors, however, agree that the broad band profile, located between 3,000 – 3,800 cm^{-1}, is caused by O−H stretching vibrations, but the number of individual contributions to the broad H_2O profile as well as their respective origins is still under discussion. The shape of the band — or rather the intensity ratios of the individual peaks, depends on (i) solution salinity (Sun, 2012), (ii) temperature (Carey and Korenowski, 1998), pH (Pezzotti et al., 2015), and (iv) even the excitation wavelength Pastorczak et al. (2008), as one band is in resonance with visible light. Typically, the O-H stretching region is deconvoluted using five Gaussian peak functions (Figure 5.5b). The origin of the splitting into five bands is unclear. It has been suggested to stem from either the O−H bond length (Diedrich A. Schmid, Kazushi Miki, 2007) or the H−O−H bonding angle (Rey et al., 2002). Another explanation, which is in good agreement with the observation of a change in shape of the O−H stretching band with salinity, is provided by Sun (2012). The author argues that the splitting is caused by H_2O molecules that act as donors or acceptors for hydrogen in their direct neighborhood. In presence of Na^+ ions, the tetrahedral hydrogen bonding is broken, leading to an excess of donor sites and a change in the pH value, which is expressed in the vibrational spectra. In the low frequency region there are several weak bands of molecular water which are not of special interest for this work. However, to study transport phenomena, isotope tracers were used in this study. For heavy water (D_2O), the entire O−H stretching region is shifted significantly to lower wavenumbers, which is clearly visible in Figure 5.5b. The shift originates from the dependence of the vibrational frequency on the masses of the vibrating atoms (Herzberg, 1945), resulting in a large frequency difference between H_2O/OH and D_2O/OD vibrations (Brooker et al., 1989).

The experiments were performed in a 0.5M $NaHCO_3$ solution, which allows the monitoring of the solution pH value by determining the [HCO_3^-] and [CO_3^{2-}] concentration from the intensity of their Raman bands near 1,016 and 1,065 cm^{-1}, respectively, using published Raman cross sections (Rudolph et al., 2008) and calculations with the geochemical program PHREEQC (Parkhurst, D.L. and Appelo, C.A.J., 2013). A detailed description of the method is given in Chapter 4.4.4. Calculations with PHREEQC, using the SIT database, revealed five carbonate species with considerable concentrations in the pH range covered by the experiments of this work (pH 7-9). Dissolved CO_2 displays two relatively weak bands at 1,277 and 1,382 cm^{-1}, which are not apparent in any of the obtained spectra, since the calculated amount

of this neutral species is ten times lower than that of the next most abundant one. The remaining four species are represented by two main bands in the Raman spectra, as they are, the $\nu_5(HCO_3^-)$ and $\nu_1(CO_3^{2-})$ bands of bicarbonate (HCO_3^-, $Na(HCO_3)$) and the carbonate ($[CO_3^{2-}$, $Na(CO_3)^-$) species, respectively.

In one *in situ* experiment, the THAM buffer was added to the solution to study the transport of the buffer molecules through the SAL. Organic compounds usually display strong bands in the frequency of the C−H_x region (2,800 – 3,100 cm^{-1}), where vibrations of carbon bonded to x = 1, 2, or 3 hydrogen atoms appear (Howell et al., 1999). In Figure 5.5b, the CH_2 vibrations are visible, as well as the NH_2 mode at 3,300 cm^{-1} (Emmons et al., 2010). THAM exhibits several bands in the low frequency region, marked with asterisks in Figure 5.5a, which, however, are not relevant to this study. A list of Raman band assignments for an aqueous THAM solution is given in Table 5.3.

Table 5.3.: Band assignment for the aqueous solutions and dissolved species.

Wavenumber [$\mathbf{cm^{-1}}$]	**Raman assignment**
1,016 / 1,065	$\nu(HCO_3^-)$ / $\nu_1(CO_3^{2-})$
∼ 2,800 - 3,100	C−H stretching
∼ 3,300	N−H stretching
∼ 2,200 - 2,800	O−D stretching (five separate bands)
∼ 3,000 - 3,800	O−H stretching (five separate bands)

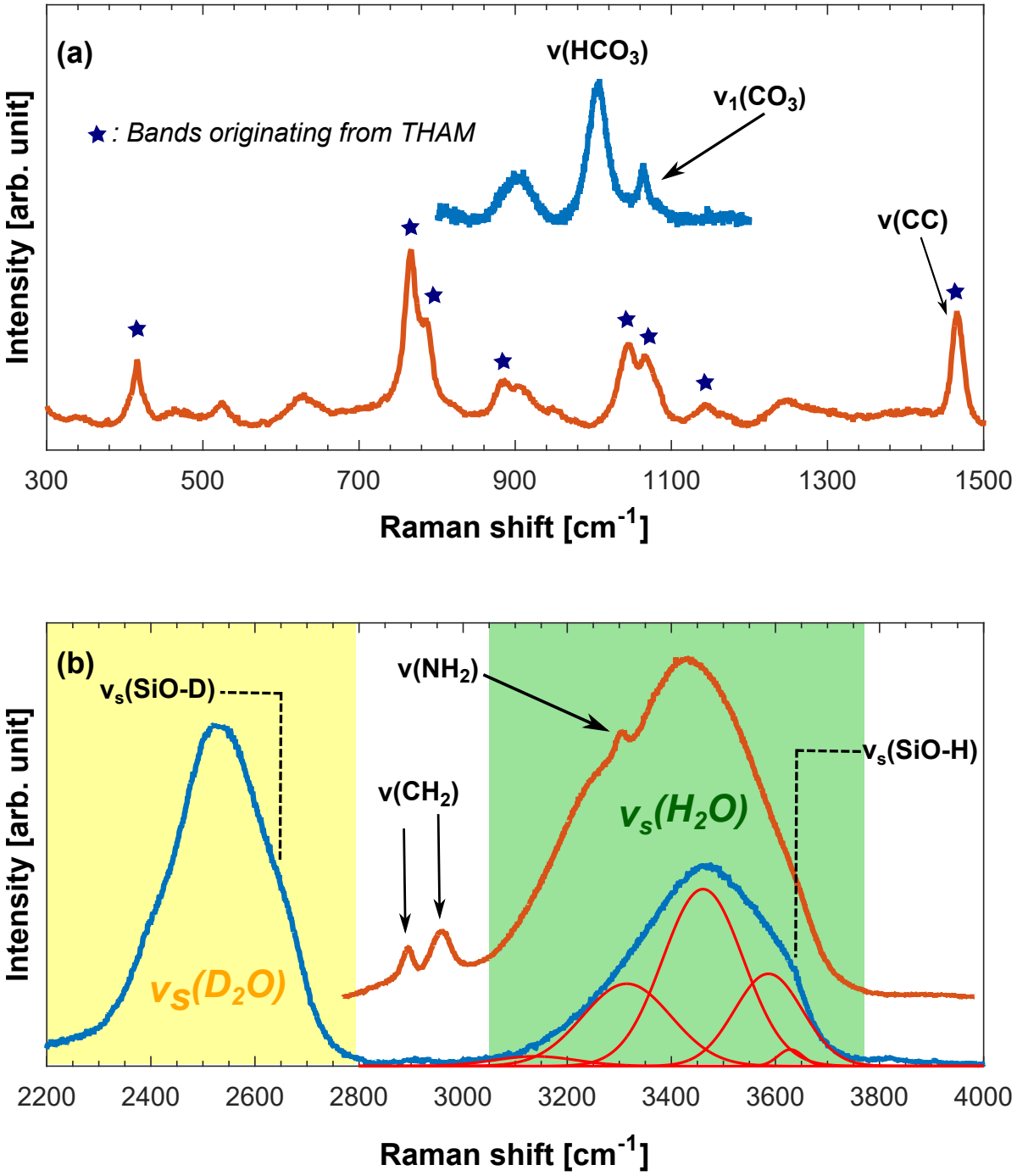

Fig. 5.5.: Raman band assignment for the aqueous solution in the low **(a)** and high **(b)** frequency region. The bicarbonate (HCO_3^-) and carbonate (CO_3^{2-}) stretching is marked in the blue spectrum in **(a)**, as well as the bands stemming from the THAM buffer (Tris(Hydroxymethyl)Aminomethane). In **(b)** the blue spectrum is obtained from a H_2O/D_2O mixture is plotted with a typical deconvolution of the O−H stretching region in red. In orange a spectrum of the same region is shown but with organic bands stemming from THAM being marked.

5.2. *In situ* experiments

5.2.1. Experiment #1, #3 and #4 - Kinetic pretest study

The first two experiments (#1, #3) were conducted under the same conditions to estimate, in the first place, the reproducibility of the method and to plan the isotope tracer study. For both experiments, the temperature was determined using the HCO_3^- band position (cf. Chapter 4.4.3). The temperature in experiment #1 was estimated to 98.7 ± 0.5 °C, whereas in experiment #4, the temperature was 81.7 ± 0.1 °C. In experiment #3, the temperature was 85.1 ± 0.7 °C. As all three experiments were run at a nominal temperature of 90 °C and the depth of measurement below the fluid-cell window was about the same in all experiments, this significant temperature difference may have been caused by a misplacement of the thermocouple after or during cleaning the fluid-cell. For experiment #1 and #3, the glass retreat was calculated by fitting sigmoidal functions to the glass intensity distributions (cf. Chapter 4.4.1). In experiment #4, an offset of about 4 µm is visible in the contour plots after 190 hours. This is most likely caused by a slight shift of the sample or the fluid cell during the course of the measurement.

For experiment #1, the observed bicarbonate-carbonate band intensity ratio had to be corrected prior to calculation of the pH value due to a dead pixel in the region of the carbonate band at 1,060 cm^{-1}. The correction value was determined by comparing the integrated intensity ratio of an average spectrum from the solution region in the second map to the same region in the first map, but after removal of the dead pixel. As the calculation of this ratio yielded a reasonable pH value of 6.96 (PHREEQC calculations at 98 °C lead to a pH value of 6.81), the difference of both ratios (0.15) was used to correct all values. It should be noted that the absolute pH values should be considered as an estimate with a systematic error, resulting, e.g., from a temperature-dependence of the relative Raman cross section of both carbonate species, that is probably in the range of about ± 0.2 log units.

Unfortunately, a massive data loss was caused by a PC crash during experiment #3. Between 23 and 100 hours, no data is available. Although no Raman signal from amorphous silica was observed, a 20 µm thick SAL was present after 100 hours, reflected by a residual rate r_1 of 0.042 µm/h. For comparison with other experimental data the initial rate was determined as well. In Figure 5.6, a linear fit to the glass retreat data in the first 23 hours can be found, resulting in an initial rate r0 of 2.1 ± 0.03 µm/h.

Already in the first image of experiment #1, slight signals for amorphous silica were visible. Due to this remarkably fast formation of an SAL, it was not possible to determine the initial rate r_0. The residual glass dissolution rate, together with the SAL growth rate, remained more or less constant during the entire experiment. Only in the last 20 hours the rate dropped slightly. A linear fit of a linear function to the data between 20-80 hours yields a residual rate r_1 of 0.63 ± 0.01 µm/h (Figure 5.7f). The offset of the retreat data at 5 and 20 hours is most

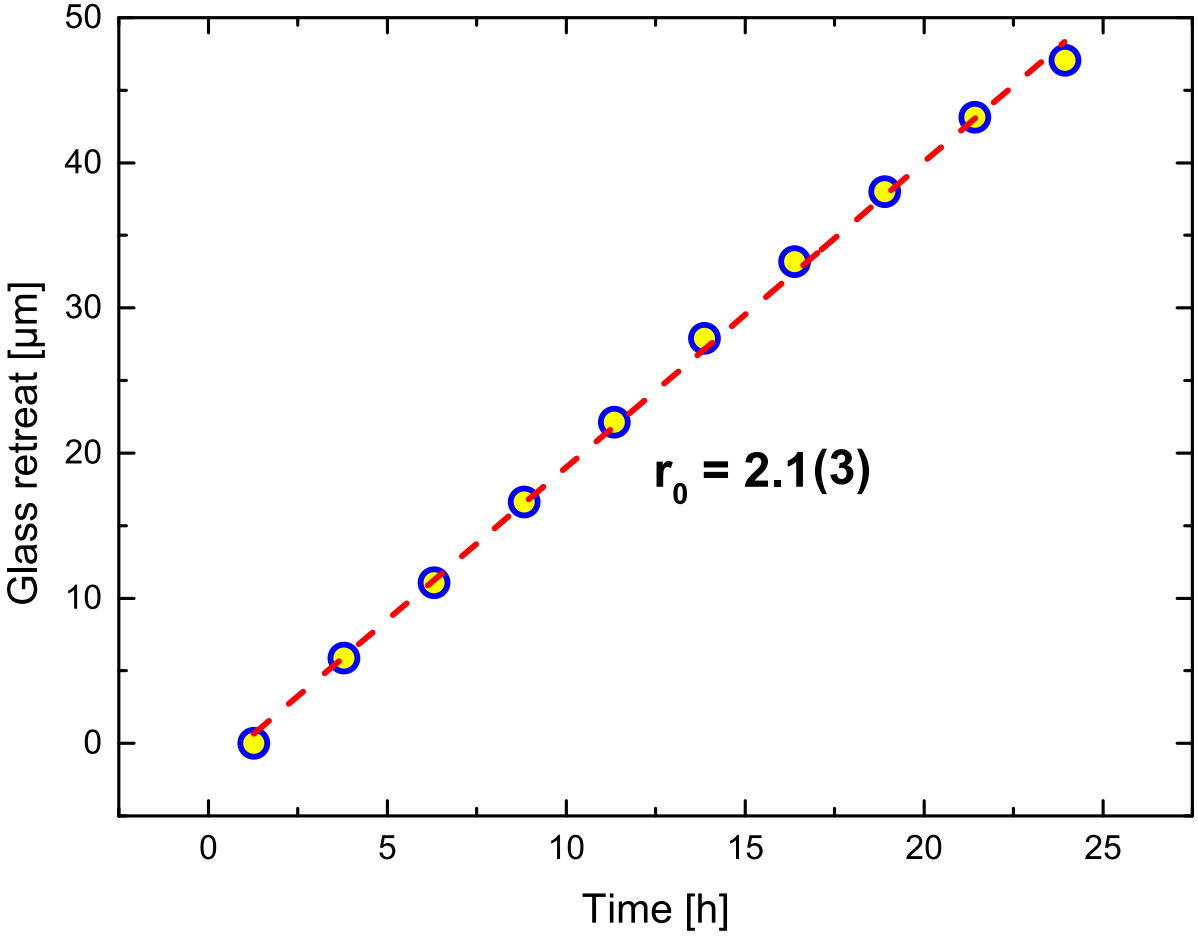

Fig. 5.6.: Glass retreat of experiment #3 between 0 and 23 hours. The dashed red line represents a linear fit to the data, giving an initial rate of 2.1 ± 0.3 µm/h.

likely caused by slight but sudden movements of the fluid-cell within the microscope stage.

The glass retreat reflects a continuous growth of the SAL to a final thickness of about 50 µm (Figure 5.7b). The R_n parameter reveals that the SAL is structurally inhomogeneous. The outer part of the SAL, which is in contact with the solution, has a higher R_n value and contains less water compared to the inner part of the SAL (Figure 5.7d,e). At the beginning of the experiment, a slight gradient in the solution pH value is visible near the glass surface (Figure 5.7c). Here the pH value is slightly higher compared to the bulk solution. Overall, the pH value increases steadily with time. A water-rich zone between the SAL and the pristine glass is hard to identify, as the whole silica phase is water-rich. Only the zone of the SAL that is in contact with the solution and which produces the strongest silica signal contains almost no water.

The results from experiment #4 are displayed in Figure 5.8. In the beginning, the glass dissolves with an initial rate of 0.89 ± 0.02 µm/h. After about 50 hours the first silica signal was detected in the Raman spectra. With the formation of the SAL, the glass retreat rate

drops by roughly one order of magnitude to 0.057 ± 0.006 µm/h (Figure 5.8f). The inset graph shows the glass retreat rate as a function of time. The red line presents a linear fit to the rate data collected between 0 and 95 hours. The intercept represents the initial forward dissolution rate (= 1.61 ± 0.4 µm/h). The SAL has grown to a final thickness of 40 µm in the course of the experiment and is, like in the other experiment, structurally inhomogeneous, as again discernible from the R_n value contour map that is plotted in Figure 5.8d. It reveals that the silica in the outer part of the SAL has a significantly higher fraction of $(Si{-}O)_4$ rings. Notably, the two zones evolve to a more distinct separation with time. In this experiment, the formation of a water-rich zone between the glass and the SAL was observed (Figure 5.8e). The solution pH value at any point in space and time was determined using the bicarbonate/carbonate ratios (cf. Chapter 4.4.4). In the bulk solution, a steady increase of the pH value is observable over time. Near the glass surface the pH values are slightly higher, most likely representing a fluid boundary layer (Figure 5.8c).

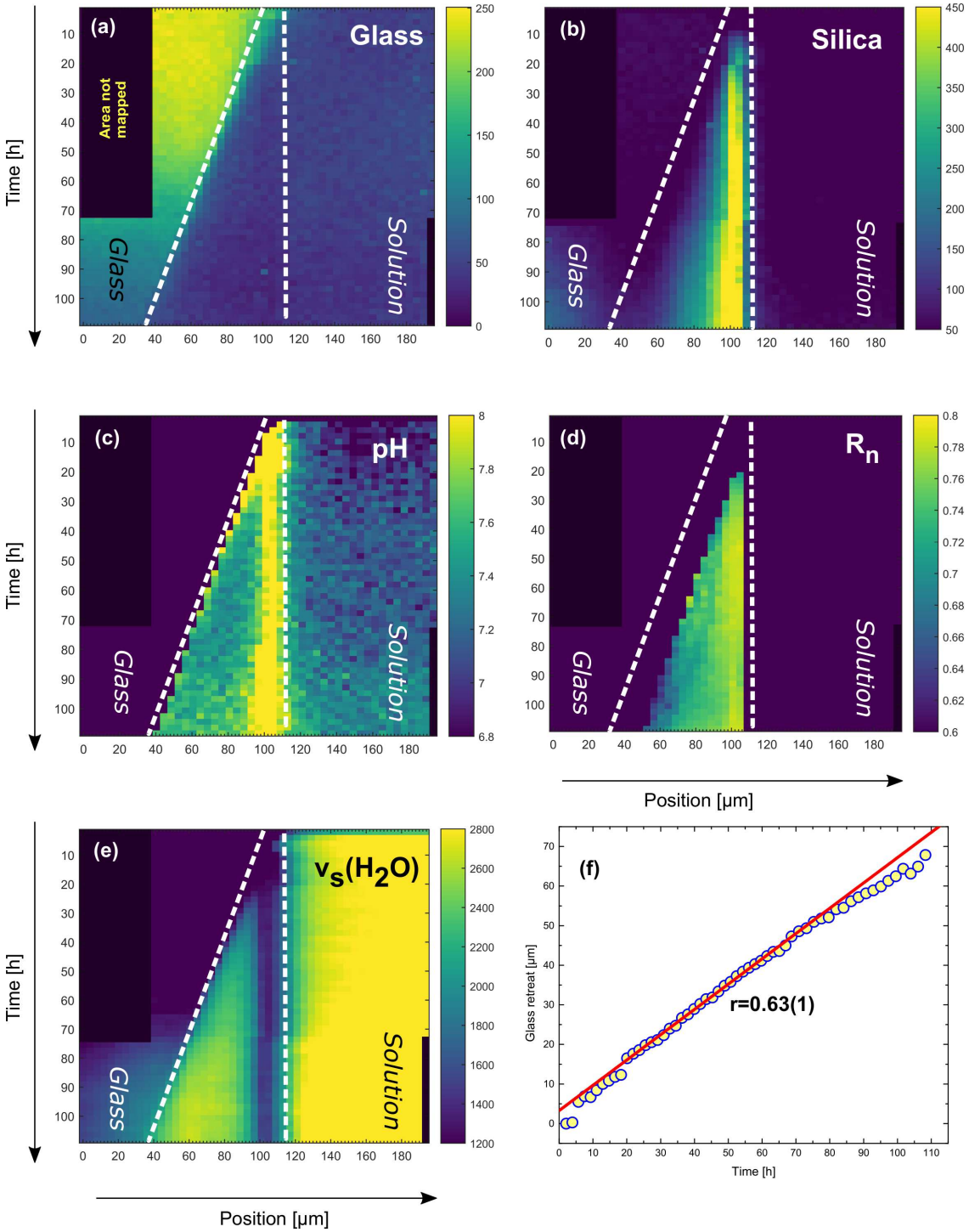

Fig. 5.7.: Distribution and chemical properties of the solution and the silica product phase (color-coded) as a function of time and space for experiment #1. **(a)**, glass (Q^n-species region); **(b)**, relative fraction of amorphous silica, represented by the integrated intensity of breathing modes of silica ring structure between 250 and 600 cm^{-1}; **(c)**, solution pH value; **(d)**, relative fraction of $(Si–O)_{n>4}$ rings in silica, represented by the ratio, R_n, of the integrated intensity between 250 - 460 cm^{-1}, i.e., the wavenumber region that is mainly composed of signals from the D_1 defect band and between 250 and 600 cm^{-1}, representing the total breathing mode intensity from all silica rings; **(e)**, total water content (H_2O + SiO–H), represented by the integrated $\nu_s(H_2O)$ intensity; **(f)**, glass retreat calculated using sigmoidal functions. Images were generated with the software package MATLAB® using the *viridis* color palette.

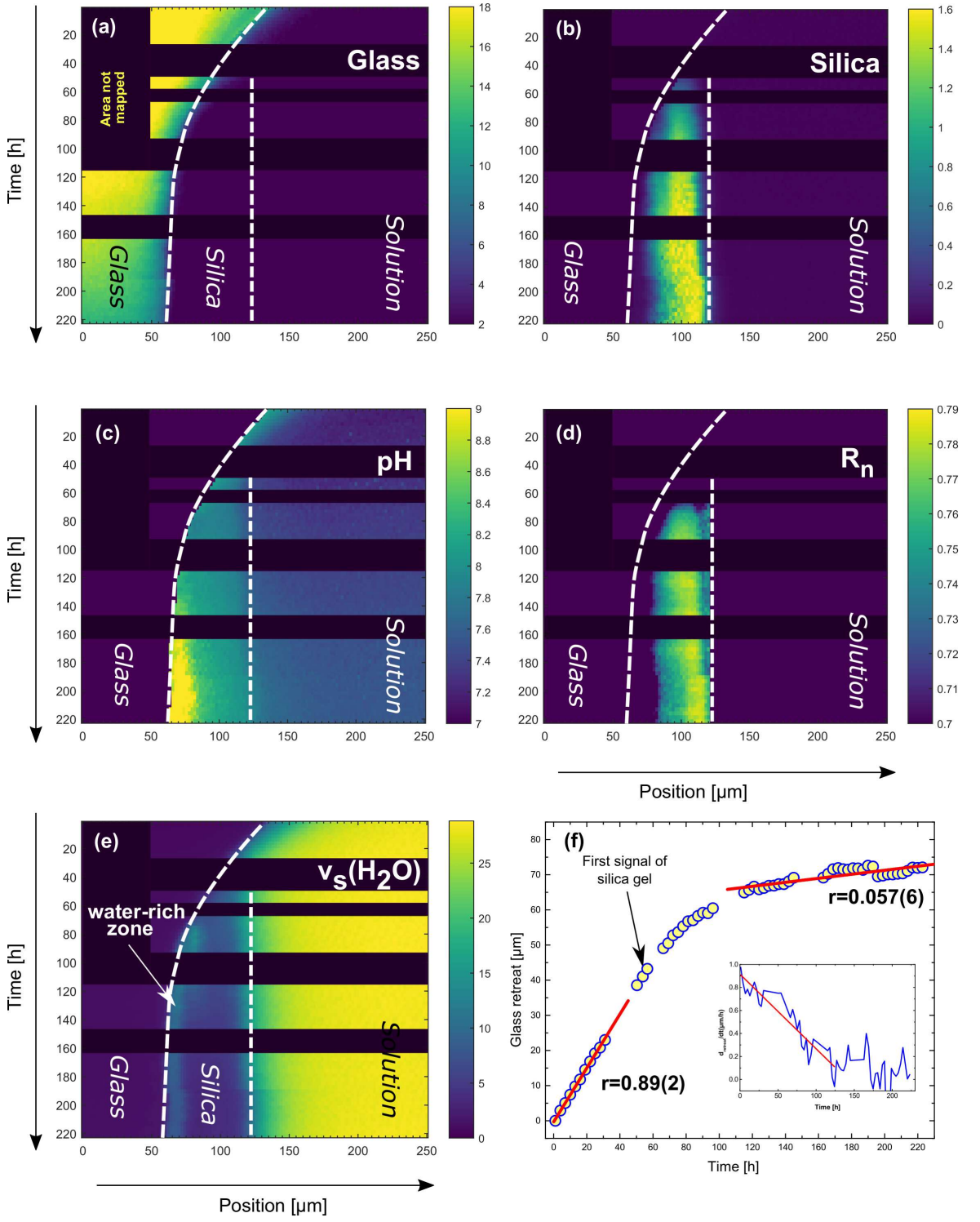

Fig. 5.8.: Distribution and chemical properties of the solution and the silica product phase (color-coded) as a function of time and space for experiment #1. **(a)**, glass (Q^n-species region); **(b)**, relative fraction of amorphous silica, represented by the integrated intensity of breathing modes of silica ring structure between 250 and 600 cm^{-1}; **(c)**, solution pH value; **(d)**, relative fraction of $(Si–O)_{n>4}$ rings in silica, represented by the ratio, R_n, of the integrated intensity between 250 - 460 cm^{-1}, i.e., the wavenumber region that is mainly composed of signals from the D_1 defect band and between 250 and 600 cm^{-1}, representing the total breathing mode intensity from all silica rings; **(e)**, total water content (H_2O + SiO–H), represented by the integrated $\nu_s(H_2O)$ intensity; **(f)**, glass retreat calculated using sigmoidal functions. The inset plot shows the derivate of the glass retreat. Images were generated with the software package MATLAB® using the *viridis* color palette.

5.2.2. Isotope tracer experiment (#6)

The experiment described in this section was designed to assess the permeability of a preexisting SAL for molecular water and the results have already been published Geisler et al. (2019). Coupled with the emergence of an SAL, usually a glass retreat rate-drop is observed. Consequently, it is assumed that the SAL must have a passivating effect. The question that shall be answered in this experiment is whether the transport of water through the SAL is responsible for the rate-drop. The *in situ* experiment was performed in a 0.5 M $NaHCO_3$ solution at a nominal temperature of 90 °C. After an SAL of ∼30 µm thickness was formed, the solution was exchanged with a fresh solution that was prepared by dissolving $NaHCO_3$ (99.98 at. % H) in D_2O (99.0 at. % D).

A preliminary experiment (140 hours) was conducted without solution exchange to plan the second experiment. For both experiments, the glass retreat was determined (cf. Section 4.4.1) and is plotted in Figure 5.11a. Initially, a continuously retreating glass-water interface was observed (forward rate r_0). After precipitation of silica, the rate drops by several orders of magnitude (r_1) and the SAL grows to a final thickness of 40 µm in the test experiment. From the inset plot, it can be derived that the rate decreased linearly with time from the beginning and dropped to almost zero after the SAL had been formed.

Using the $\nu_s\,HCO_3^-$ band position, the solution temperature at the position of the measurements was estimated (cf. Section 4.4.3) to be 81.7(1) °C for experiment #4 and 85.2(1) °C for experiment #6, respectively. This temperature difference could explain the slower forward dissolution rate in the test experiment. Figure 5.9b shows a backscattered electron image of the TBG sample corroded in experiment #4 with superimposed chemical composition maps obtained with the electron microprobe. A considerable SAL of about 40 µm thickness has formed during the experiment. The images show a clear phase boundary between the pristine glass and a dark amorphous silica phase. This phase fills a gap between the actual SAL and the glass and is characterized by (i) low backscattered electron signal intensities, indicating a high porosity and/or water concentration, (ii) a high Na concentration, and (iii) bowl-shaped cracks (filled with epoxy resin). These textural and chemical features suggest that this phase is a silica quench phase that was formed from an interfacial solution during quenching of the experiment and drying of the sample. This zone can be correlated with the water-rich zone that was observed *in situ* between the SAL and the glass (Figure 5.11d).

In Figure 5.11, the contour plots of the experiment are displayed, divided in two parts: before (Figure 5.11a-d) and after (Fig. 5.11e,f) the solution exchange. The first contour plot (Figure 5.11a) shows the evolution of the solution pH value over time prior to the solution exchange. The pH value was determined using published relative molar scattering factors to calculate the amount of the dissolved carbonate species, which strongly depends on the pH value (cf. Section 4.4.4). To measure the bulk pH value at the beginning of the experiment as accurately as possible, the first 10 spectra from the first map were averaged. From the

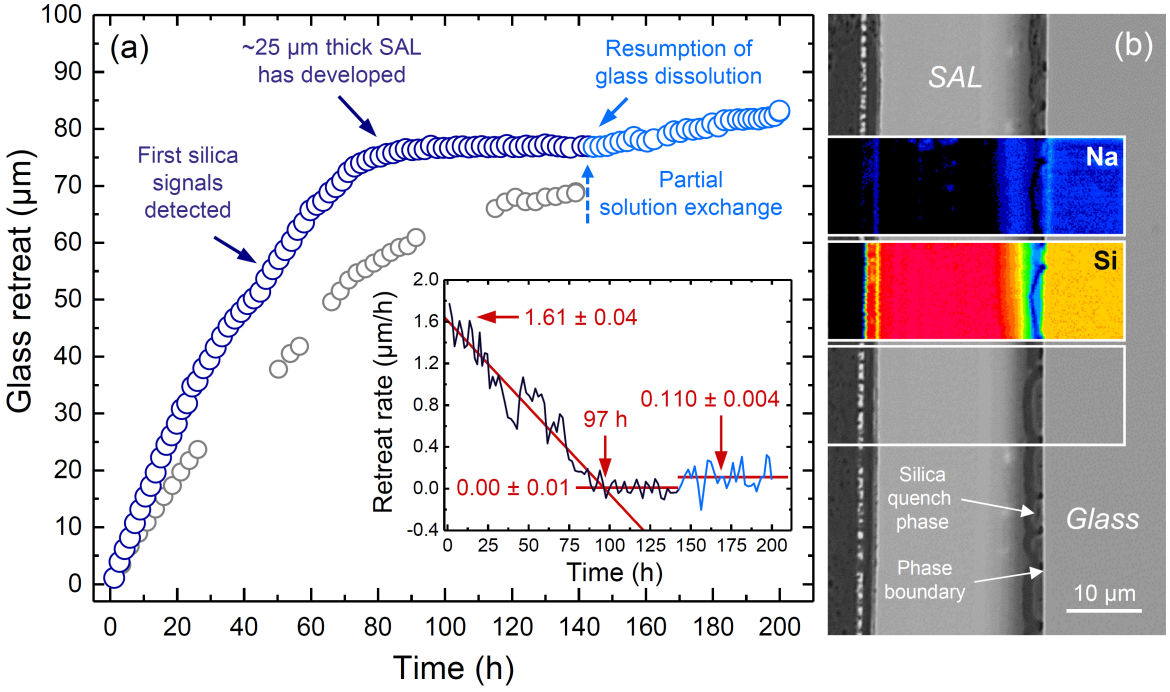

Fig. 5.9.: Temporal development of the glass retreat and chemical and textural characteristics of the dried surface alteration layer (SAL). **(a)**, Measured one-dimensional glass retreat as a function of time for the test experiment (grey circles) at 81.7 °C and the isotope exchange experiment (indigo blue circles) at 85.2 °C. Gaps in the data set of the test experiment are due to software malfunctions during the experiment. The red line presents a linear fit to the rate data collected between zero and 95 hours, the intercept of which represents the initial forward dissolution rate (= 1.61 ± 0.4 µm/h); **(b)**, Backscattered electron image from the dried SAL formed during the first test run, partly superimposed by Na and Si distribution images from an area outlined by the white rectangle. Figure taken from Geisler et al. (2019).

resulting spectrum, a pH value of 7.08 ± 0.03 was determined, which compares reasonably well with the pH value of 6.95 at 85 °C calculated with the geochemical code PHREEQC. Already at the beginning of the experiment, a steep pH gradient has evolved towards the glass surface (Figure 5.10a, 5.11a). The pH value in this ca. 50 µm thick solution boundary layer is about one unit higher, presumably reflecting a higher concentration of Sodium (as well as boric and silicic acids). Hence, the pH value of the bulk solution is different from the one at the glass surface. This finding is in perfect agreement with an in situ study by Ruiz-Agudo et al. (2016). The authors observed a steep pH gradient during the hydrothermal alteration of wollastonite ($CaSiO_3$) using microelectrodes. In a study by Putnis (2005) interferometry was applied to measure the pH value during the corrosion in a KBr-KCl-H_2O system. In both studies, pH gradients, as well as chemical gradients, ranging from a few to several hundred micrometers were observed.

The first signal of silica was detected after about 55 hours. Remarkably, the rate does not drop simultaneously with the emergence of the SAL, but rather decreases from the very beginning of the experiment. In fact, the SAL has a total thickness of 30 µm when the rate

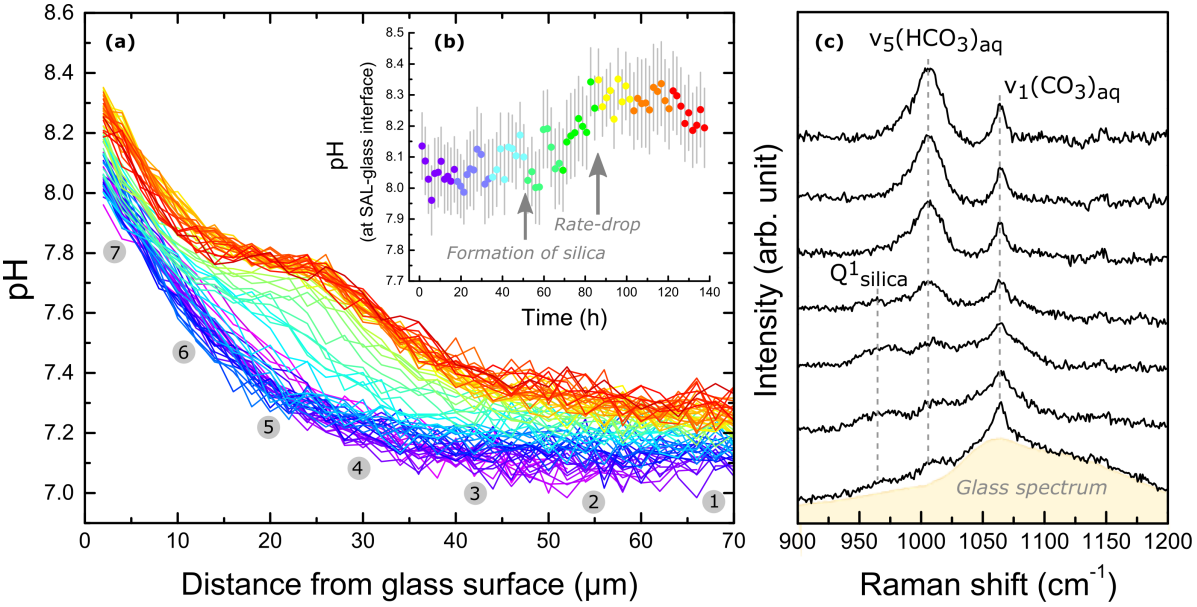

Fig. 5.10.: *In situ* solution pH value at a given time across the interfaces between the bicarbonate solution,the surface alteration layer (SAL), and the glass. **(a)**, Solution pH value as a function of the distance from the glass surface for different times between about 1 and 140 hours. Color graduation. Note the steep pH gradient from the bulk solution towards the glass surface at the beginning of the experiment (blues/purple coloured lines) and also within the 30 µm-thick SAL (red coloured lines). Numbers mark positions where spectra shown in **(c)** were taken; **(b)**, the pH value of the (interfacial) solution at the glass surface as a function of time. Note the sudden pH value increase once an SAL has begun to form; **(c)**, representative *in situ* Raman spectra in the wavenumber region of the $\nu_1(CO_3)$ and $\nu_5(HCO_3)$ band at 85 °C after 139 hours, showing their evolution from the bulk solution towards the SAL–glass interface. Note that the increasing $\nu_1(CO_3)$ and decreasing $\nu_5(HCO_3)$ band intensity from the bulk solution (spectrum 1) towards the glass surface (spectrum 7). The spectra close to the SAL–glass boundary the carbonate bands are overlain by ν_s(Si−O) bands from the glass (light yellow area) and from amorphous silica (the Q^1 band of silica is marked). Figure taken from Geisler et al. (2019).

drops to zero after ∼80 hours. This is apparent from Figure 5.11b, where the contour map for the total intensity of amorphous silica is shown. Along with the rate-drop, a steep pH gradient within the SAL emerges, which is shown in Figure 5.10a. The pH value is plotted as a function of the distance from the glass. Every plotted line represents a time step between the start of the experiment (blue/purple colored lines) and the time point after 139 hours (red colored lines). The inset plot shows the evolution of the pH value at the SAL/glass interface over time. A sudden increase in the pH value with the formation of the SAL is noticeable. The numbers in the grey circles mark the position at which the spectra in (c) were acquired 139 hours after the experiment start. It is clearly visible that the ratio of the $\nu_1(CO_3)$ and $\nu_5(HCO_3)$ bands significantly changes towards the SAL, reflecting a change in the pH value.

In Figure 5.11c, the contour plot of the ring structure parameter R_n is shown. It is defined as the ratio of the integrated intensities of the $(\delta_{ring}(\text{Si}-\text{O}-\text{Si})_4)$ to $(\delta_{ring}(\text{Si}-\text{O}-\text{Si})_{4\ldots6})$ modes. Basically, it gives the fraction of $(\text{Si}-\text{O})_{n>4}$ rings (cf. Section 4.4.2). From the contour plot it is evident that the SAL formed in the *in situ* experiment was not structurally homogeneous. The siloxane ring structure gradually changes to a lower fraction of $(\text{Si–O})_{n>4}$ rings towards

the glass side, pointing to changes of the physicochemical conditions at the reaction interface with increasing SAL thickness. Apparently, the R_n parameter does not change for any given location within the SAL with time, indicating the silica ring structure to be rather stable. In Figure 5.11f, the contour plot of R_n is shown after the solution exchange. It can be noted that at least two domains are formed. As before the solution exchange, the fraction of $(\text{Si–O})_{n>4}$ rings is lower towards the glass. However, during the first twenty hours the part of the SAL in contact with the solution also exhibits a lower value for R_n. This may be due to the breakage of siloxane bonds triggered by the fresh, silicon-free solution. Furthermore, the distribution of the R_n parameter in the SAL is blurred at the beginning, while evolving with time to a distinct layer of about 5 µm thickness with a high fraction of $(\text{Si–O})_{n>4}$ rings towards the solution.

Another unique observation is the formation of a water-rich zone between the SAL and the pristine glass (Figure 5.10d), which is an immanent feature of an ICDP process. The interfacial solution was postulated to appear during glass corrosion (Geisler et al., 2010; Dohmen et al., 2013; Geisler et al., 2015; Lenting et al., 2018), which is in good agreement with the 4 microns thick contact zone between the pristine glass and the SAL observed in the microprobe analysis of in situ experiment #4 (Figure 5.9b). This relatively broad sodium-rich zone with a low density most likely corresponds to interfacial fluid found in the *in situ* experiment. That could be the reason why the interfacial fluid was detected here with confocal Raman spectroscopy, whereas for more complex glasses a nanometer-sized interfacial fluid (Lenting et al., 2018) would not be detectable with this method.

After 142 hours, the solution was partially exchanged with a fresh 0.5 M $NaHCO_3$ solution prepared in D_2O. The deuterium gives the possibility to monitor the water transport through the SAL towards the interfacial solution by Raman spectroscopy due to a pronounced vibrational frequency red shifts compared to H_2O. The fresh bicarbonate solution passed the SAL and reached the water-rich zone within an hour. However, by that time an equilibrium was not fully reached (Figure 5.11e). As the full equilibrium was reached after 10 hours, the SAL clearly acts as a barrier for water molecules. In Section 4.4.5 it is explained in detail how the diffusion coefficient was calculated from the intensity distribution maps. A mean pore water diffusion coefficient D_{pw} of $2.1 \pm 0.2 \times 10^{-14}\ m^2/s$ was obtained, which is six orders of magnitude slower than self-diffusion of water at 85 °C (Mills, 1973), but still significantly faster than hydrogen and molecular water diffusion in silicate glasses ($D_{gw} < 10^{-18}\ m^2/s$ (Grambow and Müller, 2001; Frugier et al., 2008)).

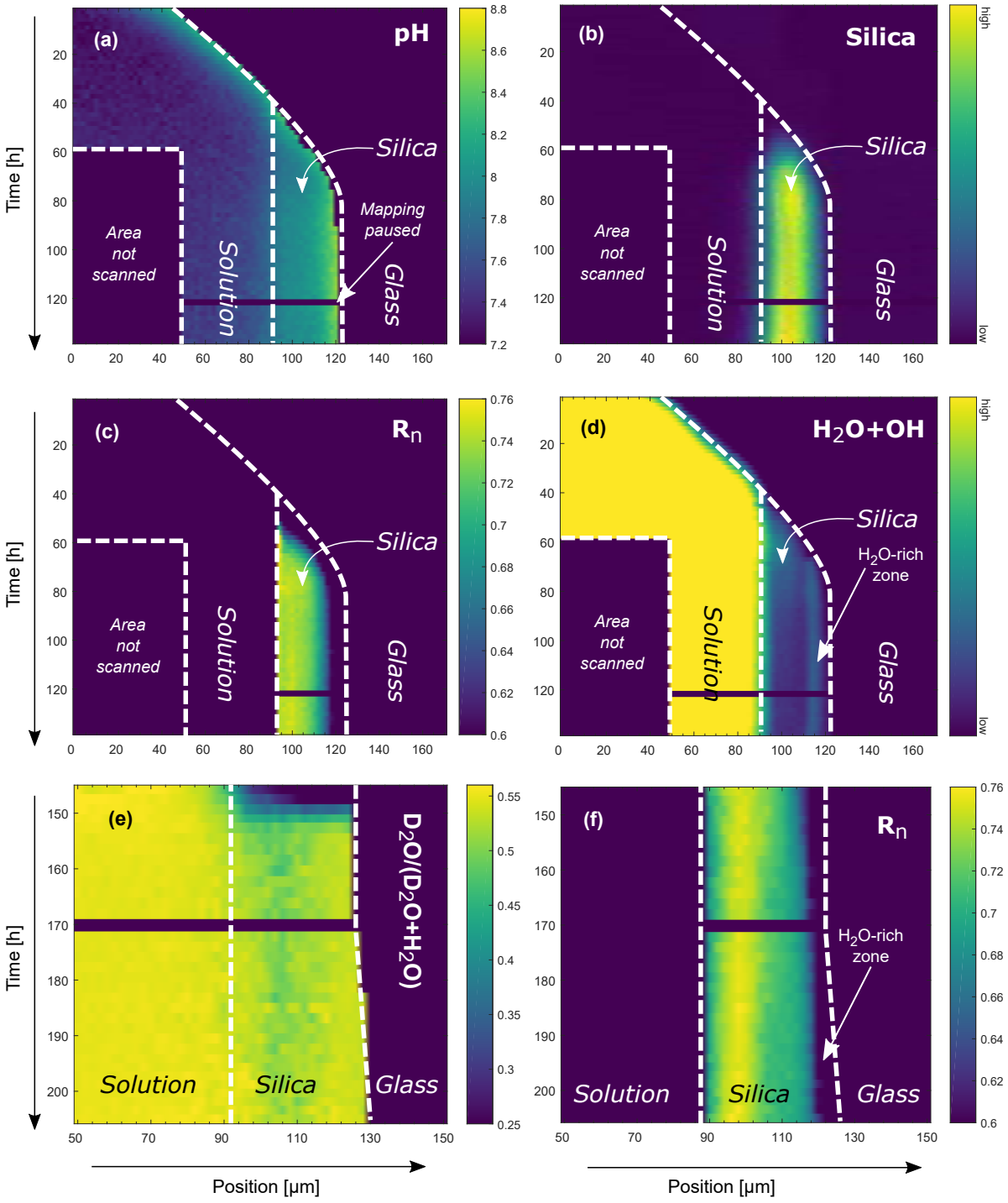

Fig. 5.11.: Distribution and chemical properties of the solution and the silica product phase (color-coded) of experiment #6 as a function of time and space. **(a)**, Solution pH value; **(b)**, Relative fraction of amorphous silica, represented by the integrated intensity, A250–600, of breathing modes of silica ring structure between 250 and 600 cm^{-1}; **(c)**, Relative fraction of $(Si–O)_{n>4}$ rings in silica, represented by the ratio, R_n, between integrated intensity between 250–460 cm^{-1} of silica O–Si–O breathing modes and A250–600; **(d)**, total water content (H_2O + SiO–H), represented by the integrated $\nu_s(H_2O)$ intensity; **(e)**, Fraction of D_2O in solution after solution exchange; **(f)**, Relative fraction of $(Si–O)_{n>4}$ rings after partial solution exchange. Note the clear separation of the SAL in two distinct structural layers. The value behind each pixel in the images represents the average from three parallel line profiles. Images were generated with the software package MATLAB® using the *viridis* colour palette. Figure taken from Geisler et al. (2019).

5.2.3. THAM buffered experiment (#11)

Usually, glass corrosion studies that aim to examine the influence of the pH value use buffer solutions. A widely applied buffer for the pH range from 9 to 10 is the organic compound THAM or TRIS (Arab et al., 2008; Icenhower and Steefel, 2013, 2015; Verney-Carron et al., 2008). Concerning an ICDP process, it is of interest whether the interface fluid is buffered or not. If the buffer is able to reach the reaction front, the dissolution of the glass and the resulting precipitation of the silica occur under buffered conditions, so a THAM buffer solution would affect the formation of a SAL in glass corrosion experiments. The following experiment was designed to shed light on the ability of the buffer to migrate through the SAL.

A fresh TBG glass coupon was placed in the fluid-cell, which was then filled with a 0.5 M THAM solution and heated to a nominal temperature of 90 °C. Most probably, a gas bubble was present at the mapping position on the glass surface between 30 and 50 hours during the experiment. This can be concluded from the H_2O vibrations contour map (Figure 5.13a), where a steep drop in intensity is observable at a position of 30 µm. In the next 20 hours, the signal intensity recovers, presumably due to shrinking of the gas bubble or slow movement out of focus. However, this does not influence the results presented below.

After the start of the experiment, the dissolution rate of the glass was virtually zero for about 24 hours. The evolution of the glass retreat over the whole experiment is plotted in Figure 5.13e. The glass retreat was calculated by fitting sigmoidal profiles to the intensity distributions presented in Figure 5.13a. After the first day, the glass started to dissolve with a forward dissolution rate of $r_0 = 1.1(1)$ µm/h until the first silica precipitates after 60 hours. From here on, the dissolution rate dropped dramatically to values to almost zero, i.e., $r_1 = 0.001(1)$ µm/h. However, after 110 hours, a resumption of the rate was observed that persisted for the rest of the experiment that was eventually stopped after 265 hours. The resumption rate was $r_2 = 0.477(6)$ µm/h and thus not as high as the forward rate. It is also notable that the rate slightly deceased after 230 hours. During the whole stage III rate regime, the SAL has grown constantly to a final thickness of ca. 100 µm, at which point the experiment was aborted (Figure 5.13b). The integrated intensities of the OH stretching region, stemming from molecular water and OH bonded to silicon, are plotted in the contour map in Figure 5.13c. The emergence of a water-rich zone between the SAL and the pristine glass was observed after 220 hours. This observation is supported by the average spectrum from the interfacial region shown in Figure 5.13f (spectrum number 5) that is characterized by only the broad water band without the SiO−H stretching. Apparently, the drop in the stage III rate is coupled to the appearance of the water-rich zone. The vibrations in the CH_x region were used to trace the THAM (Fig. 5.13f). To estimate the concentration of THAM in the pore water of the SAL, the bands in the CH_x region were integrated and normalized to the overall integrated intensity in the OH stretching region (Figure 5.13d). Average spectra of five regions in the bulk solution, the SAL and the reaction interface are shown in Figure 5.13f. It is evident that the buffer is

more concentrated in the SAL pore water solution than in the water-rich zone, although it is also clearly detectable in the water-rich zone. Strikingly, the highest enrichment is visible in the SAL zone that is in direct contact with the bulk solution.

A possible explanation for the rate resumption is that the outermost layer of the silica rim hinders the transport of the buffer towards the interface fluid. The frequent observation of a thin dense rim as the outermost layer of glass corrosion zone during *post mortem* analysis supports this assumption. After the first ∼10 µm SAL had been formed and the residual rate had ensued, the corrosion reaction de facto came to a halt. Presumably, the SAL acts as an effective barrier for the transport of silica agglomerates/colloidal particles that are present in the interface fluid. As the particle size of the polymeric silica depends on many factors like the pH value, the salinity and the solution chemistry (Iler, 1979), changes in one of these factors have an influence on the silica particle size. An enrichment of the buffer over time at the interface may have led to smaller colloidal silica particles and the negation of the passivating character of the SAL. A slower diffusion of the buffer compared to the inward moving reaction front would lead to a decrease in the retreat rate, which is visible in Figure 5.13e at ∼220 hours. The CHx/H_2O intensity ratio as a function of the experiment's duration in Fig. 5.12 gives further evidence. The data is obtained from the respective contour plot, were the first three data points next to the glass boundary were averaged. A linear fit delivers proof that the concentration of the buffer in the interface fluid decreased with time, suggesting a decoupling of buffer diffusion and the ICDP reaction front velocity. The *in situ* experiment clearly demonstrates that the THAM buffer itself has a profound influence on the dissolution kinetics, i.e., the buffer cannot be considered to be inert with respect to the glass-water reaction process.

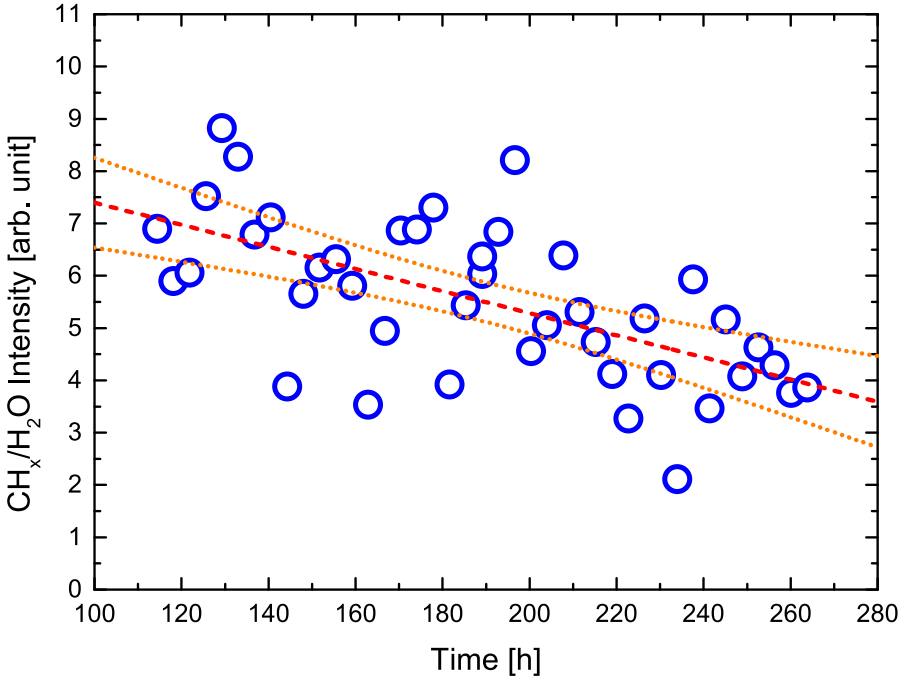

Fig. 5.12.: CH_x/H_2O intensity ratio as a function of the experiment's duration. The blue circles are represent the average of the three datapoints next to the reatreating glass. The error lies within the symbol size. A linear fit (red dashed line) and the 95% confidence intervals (orange dotted line) show the decrease of the CH_x intensity in the interfacial fluid with time.

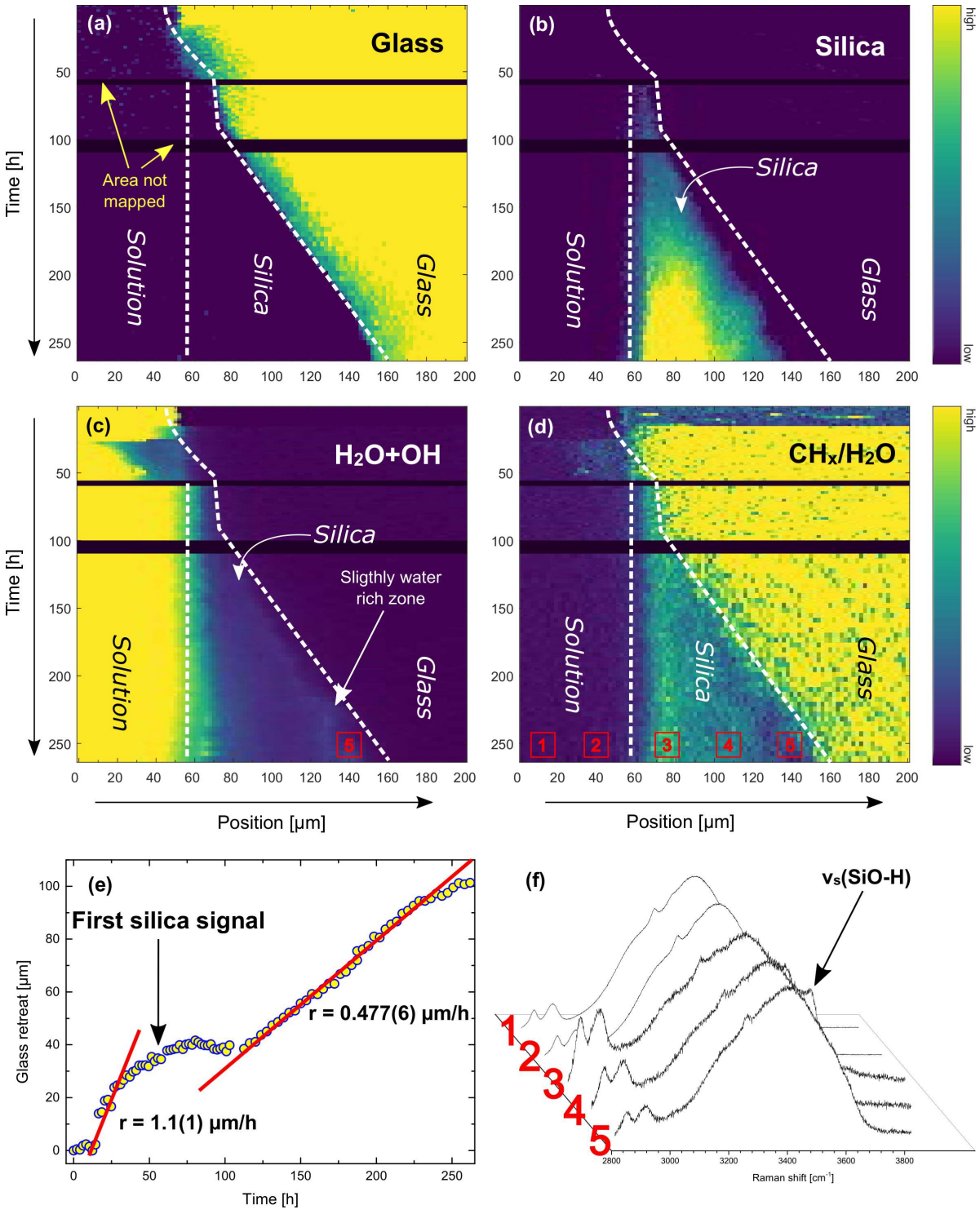

Fig. 5.13.: Distribution and chemical properties of the solution and the silica product phase (color-coded) of experiment #11 as a function of time and space. **(a)**, glass (integrated Q^n-species region); **(b)**, relative fraction of amorphous silica, represented by the integrated intensity of breathing modes of silica ring structure between 250 and 600 cm^{-1}; **(c)**, total water content (H_2O + SiO–H), represented by the integrated $\nu_s(H_2O)$ intensity; **(d)**, relative fraction of THAM in water represented by the CH_x modes versus the total OH stretching modes (H_2O + SiO–H); **(e)**, glass retreat calculated using a sigmoidal function. Rates for stage I and III are given; **(f)**, averaged Raman spectra from the regions labeled 1-5. Images were generated with the software package MATLAB® using the *viridis* color palette.

5.2.4. AR-GLAS® experiment (#2)

The *in situ* experiment presented in this section is the only one in this work with a glass other than TBG and addresses the question whether the corrosion of glasses that are more refractory can also be examined by fluid-cell Raman spectroscopy. Preliminary *ex situ* experiments and subsequent *post mortem* microprobe analysis indicated that an SAL should form within a suitable time period (cf. Section 4.1). Because each of the acquired maps contained 3 lines with 5 µm distance, vertical three-points averages were calculated for all values presented for this experiment.

In this particular experiment, the fluid-cell was fixed to the sample stage with double-sided tape. By the end of the experiment the tape had considerably softened and was almost melted due to the high temperature of the steel mantle. In the first 10 hours of the experiment, the retreat value was negative, which most likely is due to a slow relocation of the fluid-cell, slowly sliding into its final position. After that, a linear glass retreat with a rate of 0.11 µm/h was observed (using a sigmoidal fitting method). Figure 5.14a and b shows the contour plots of the glass signal and the glass retreat, respectively, as a function of time. The inset graph in Figure 5.15b displays the evolution of the glass retreat rate with time. The red line is a linear fit to the data between 10 and 150 hours with its intercept representing the initial forward rate of 0.14 ± 0.03 µm/h. After 150 hours, the precipitation of calcite on the former glass surface was detected (Figure 5.14d). At this time, the pH and the glass retreat rate slightly decreased. After 225 hours a resumption of the glass retreat is noticeable from Figure 5.15b. However, after 150 hours the overall dissolution rate of the glass was very low, so the changes may lay within the error, at least for the change in the retreat rate-versus-time plot (inset in Figure 5.15b).

Before the formation of calcite, another secondary phase had already been precipitated. A representative spectrum of this phase is shown in the inset plot of Figure 5.14b. Only one Raman band is observed for this yet unknown phase that appears near 680 cm^{-1}. It can be excluded that the phase is a modification of the calcium carbonate, as the band appears before the formation of calcite precipitates and no CO_3 vibration is present in the spectrum. Apparently, the phase is the first precipitate and represents the outermost layer of the corrosion zone. In Figure 5.15c, the positions of the intensity maxima of the respective phase are plotted. The data represents averaged values for the last five images that were taken before the experiment was stopped. Two bands, one stemming from the unknown phase and one from the calcite phase, are visible. The corrosion zone can be divided in two parts, one facing the solution, consisting of the unknown phase, and the calcite section next to the pristine glass. Between the calcite and the glass, a slim water-rich zone has formed that is interpreted to represent an interfacial solution. Representative spectra from the two positions, labeled as 1 and 2 in the grey circles, are shown in Figure 5.15d. The calcite spectrum (purple) shows only a low intensity signal for the 680 cm^{-1} band, assigned to the unknown phase,

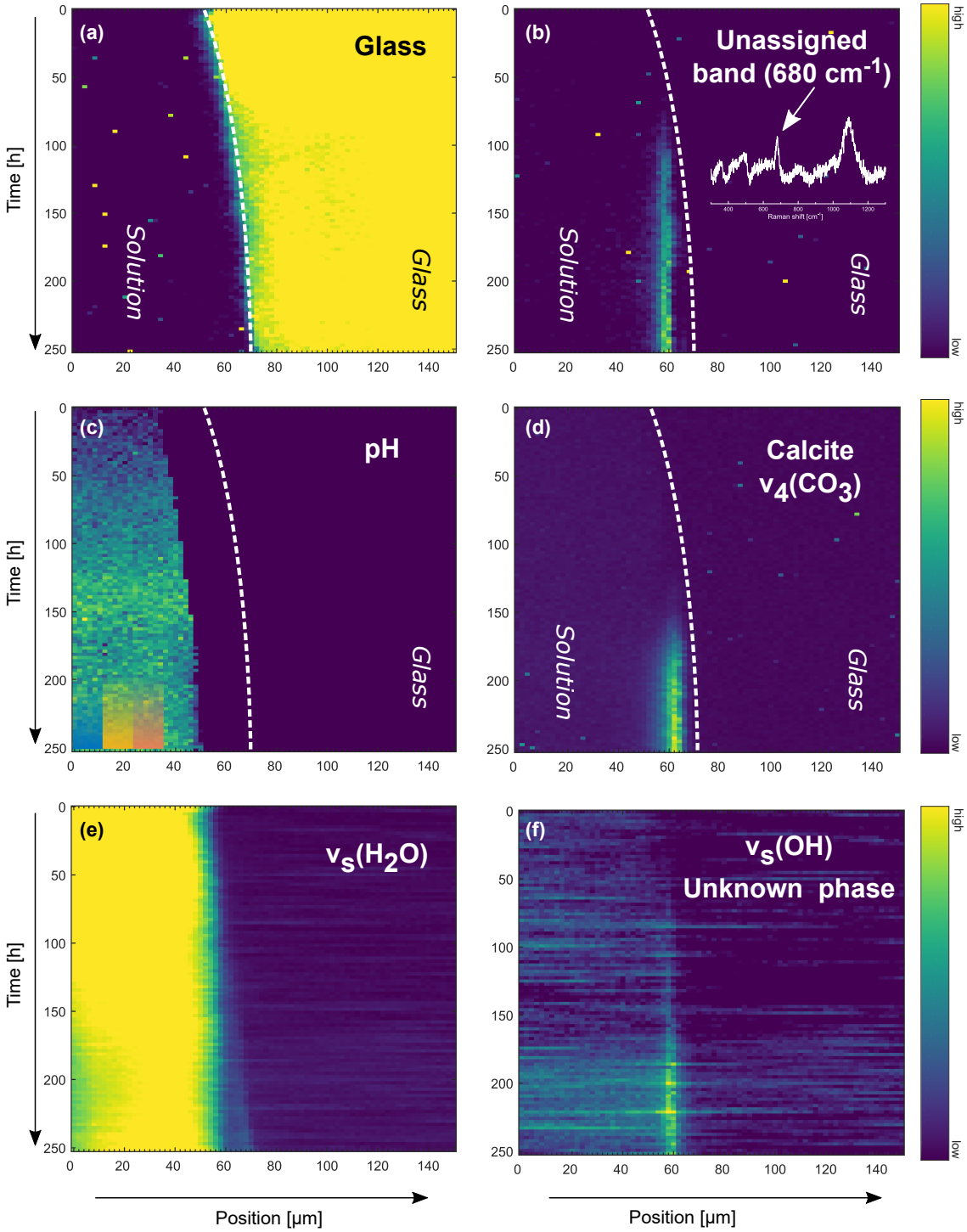

Fig. 5.14.: Distribution and chemical properties of the solution and the precipitated phases (colorcoded) as a function of time and space. **(a)**, glass; **(c)**, solution pH, calculated using the carbonate/bicarbonate ratio (cf. Section 4.4.4); **(e)**, Water, represented by the integrated intensity of $\nu_s(H_2O)$ vibration; **(d)**, Calcite ($\nu_4(CO_3)$. In **(a)** it is visible that the glass dissolves with an, on the first glance, constant rate. The data is plotted as function of time in Figure 5.15c. The pH value increases with time, but drops visibly after ~150 hours **(c)**. The regions marked with the three colors at bottom left are averaged and plotted in Figure 5.15. In **(e)** the $\nu_s(H_2O$ contour map is shown, indicating a water-rich corrosion zone. Two phases precipitated during the experiment, calcite **(d)** and a unknown phase **(b)** represent only by one weak band at ~680 cm^{-1} (Raman spectrum is plotted in inset of **(b)**). Alongside with it, a sharp band in the OH stretching region appeared **(f)**.

whereas this band is more pronounced in the red spectrum obtained at position 1. Because of the extremely high Raman scattering cross section of the calcite vibrational modes, this spectrum is strongly superimposed by the calcite bands. However, the spectra of the first precipitates of the unknown phase are free from any calcite signal, implying that the phase is not a solid solution of carbonates (e.g., witherite). Along with the unknown phase, a strong sharp band appears in the OH stretching region. The corresponding contour map is shown in Figure 5.14f and a representative spectrum is depicted in Figure 5.14d. It is certain that this band does not stem from H_2O or Si−OH groups, as the band is too sharp and the position differs significantly from the silanol group. Nonetheless, the presence of this band and its emergence together with the unassigned band at 680 cm^{-1} indicates that the unknown phase is a hydroxide. Some calcium silicate hydrates are known to give an intense band at 680 cm^{-1}. In this case, the other Raman bands are superimposed by the strong band from the CO_3 group stretching motions (Ortaboy et al., 2017). Within the framework of a master thesis the AR-Glass was corroded in a hyper alkaline carbonate solution (Gerrit Müller, 2019). *Post mortem* analysis delivered evidence for the presence of smectite (saponite), which is a OH-bearing sheet silicate that shows a main Raman band near 678 cm^{-1}. It follows that the identification of the unknown phase remains unknown at this stage.

The solution pH value in this experiment was determined using the carbonate speciation method that is described in detail in Section 4.4.4. It must be noted that the carbonate in solution is consumed by the precipitating calcite. However, as the amount of dissolved Ca ions is negligibly low relative to the carbonate and the hydrolysis reaction of the bicarbonate is extremely fast, carbonate precipitation had not to be considered in the pH calculation. The results are displayed in Figure 5.14c. The calculated initial pH value was 6.75 ± 0.1 pH units, which corresponds reasonably well with the modeled value of 6.9 at 91.0 ± 0.2 °C using the SIT database and the geochemical code PHREEQC (Parkhurst, D.L. and Appelo, C.A.J., 2013). The pH contour plot has a 20 µm thick zone at the glass surface for which no pH values were calculated due to the overlap of the $\nu_1(CO_3)$ vibration of the aqueous dissolved carbonate with the $\nu_1(CO_3)$ vibration of the calcite, which is a relatively strong Raman scatterer. Thus, the convolution of the bands would lead to a spurious decrease of the pH values near the surface of the SAL. However, visual inspection of the spectra revealed no interference by the calcite bands if a 20 µm distance is kept to the glass surface. To obtain better statistics, five values were horizontally averaged, leading to three values per image. The averaged regions are marked in the pH contour plot in the lower left corner while the evolution of the solution pH plot as a function of time is shown in Figure 5.14e. After the start of the experiment, the pH value increases at a constant rate, reflecting the release of glass constituents into the solution. Note that simultaneously with the precipitation of the calcite, the pH value of the solution drops by 0.2 units. After approximately 50 hours, a resumption of the pH increase rate is observable. The pH drop most likely reflects the consumption of dissolved cations by the precipitating calcite. As known from other experiments in this work (see experiments #4

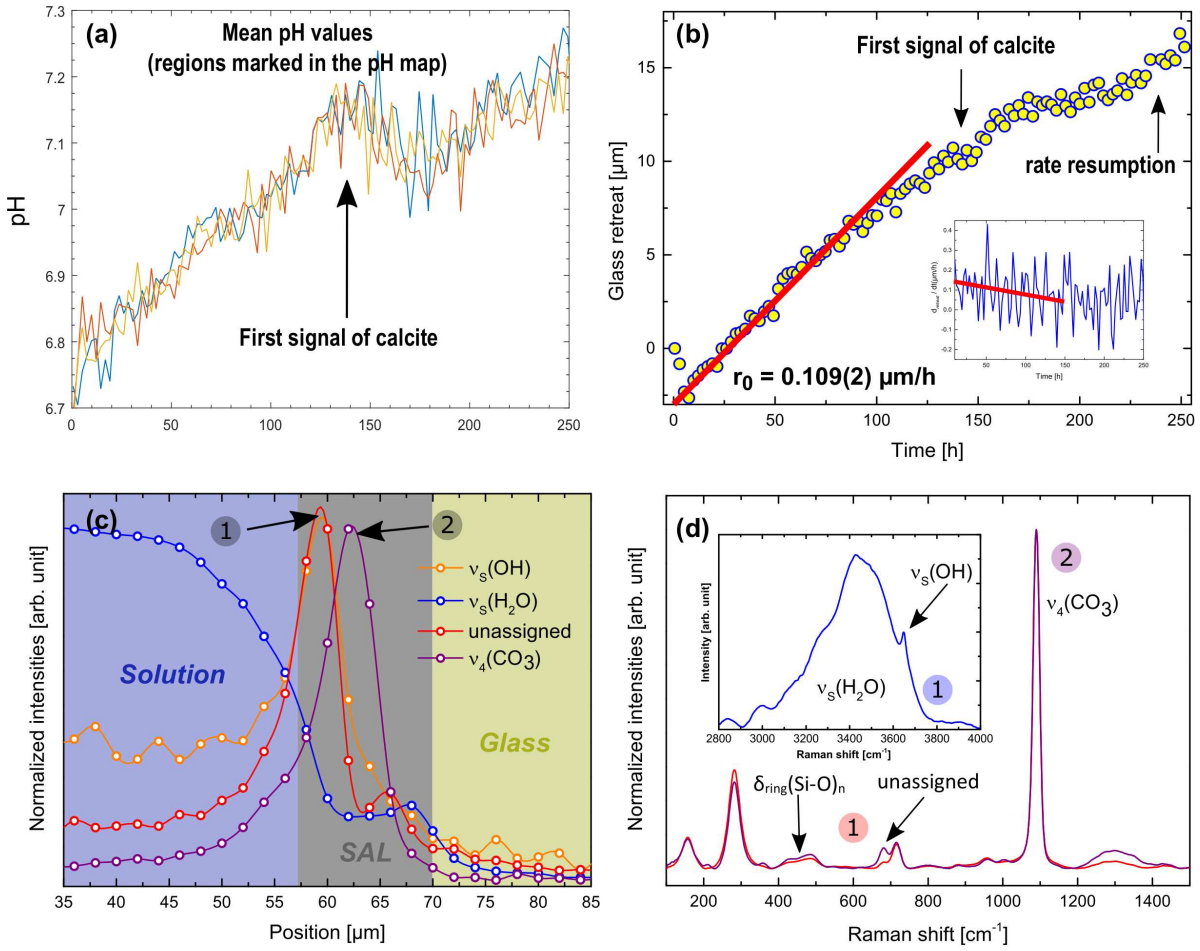

Fig. 5.15.: **(a)** Evolution of the pH value as function of time, averaged in the three regions marked in Figure 5.14c. With precipitation of calcite, a simultaneous drop in the pH value as well the corrosion rate can be observed. This is shown in **(b)** with the red dashed line representing a fit to the data between 0 and 120 hours, giving an overall rate in this timeframe of 0.109 µm/h. The inset plot shows the glass retreat rate as a function of time with a red dashed line representing a fit to the data between 0 and 150, resulting in an initial rate of 0.14(3) µm/h. In **(c)**, the position of the phases present in the experiment is shown by plotting the intensities of the Raman bands. The unknown phase, represented by an unassigned band, is located with its maximum intensity at ∼57 µm (labeled 1 in grey circle), together with the maximum of the OH stretching not stemming from the water (cf. main text). The calcite band, on the other hand, has its maximum at ∼63 µm (labeled 2 in grey circle), in the corrosion zone region in contact with the glass. The OH stretching of the water is plotted in blue, defining the corrosion zone with its decrease. At ∼67 µm the slight water-rich zone representing the interfacial fluid is visible. For the maxima positions 1 and 2, spectra are plotted in **(d)**. At ∼680 cm^{-1}, the band of the unknown phase is visible, present at position 1 but not at 2. The inset is a spectrum of the (OH) stretching region obtained at position 1 with a strong, sharp band at ∼3680 cm^{-1}, certainly not stemming from the H_2O molecule. The data in **(c-d)** is an average of the last five maps of the experiments.

and #6), a fluid boundary layer with higher pH values compared to the bulk solution develops at the dissolving glass surface. In the contour plot this zone is cut to account for the overlap of the calcite band with the carbonate band used for calculation of the pH value. However, prior to the calcite precipitation, no interference is expected and the pH values near the glass surface were determined. It is to note that, a pronounced solution boundary layer, like in the TBG experiments, cannot be observed. Therefore, the pH values were averaged at the glass surface and inside the bulk solution over 10 µm and seven images (Figure 5.16). Evidently, a slight pH gradient with a higher pH value at the dissolving glass surface is now clearly detectable

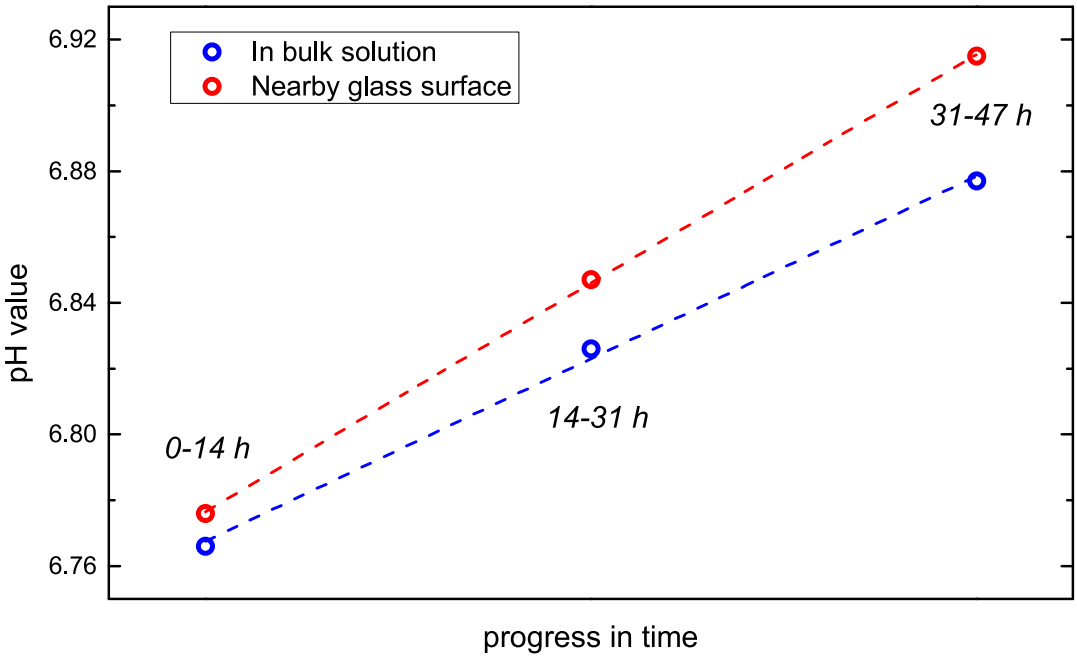

Fig. 5.16.: Averaged pH nearby the glass surface (red) and inside the bulk solution (blue). The datapoints represent an average over 10 micrometers and 7 maps. It is evident that a slight gradient has formed.

After the experiment, the dried sample was examined by electron microprobe. In Figure 5.17, a BSE image of the corrosion zone is displayed along with chemical distribution maps of the region highlighted with a yellow rectangle. On the left-hand side of the chemical distribution images, the BSE image of the same region is superimposed. The pristine glass (bright BSE contrast) is in direct contact to the plain SAL, on which a thin layer with a brighter BSE contrast is located. Both layers of the corrosion zone are arranged in a parallel fashion. The *in situ* Raman data suggests that the corrosion zone is about 10-15 micrometers thick. The BSE image reveals that the zone has, in fact, a thickness of 5 µm. The difference between the thicknesses measured with the two different methods may reflect the inferior spatial resolution of the Raman measurements, but it may also be due to the fact that not exactly the same areas are compared. The qualitative WDX analysis reveals the plain SAL to be rich in silica and strongly depleted with respect to Na, Ba and Ca. However, all these elements are still present at low concentrations. Between the plain zone and the dense rim, a small gap with a dark BSE

contrast is visible. A significant enrichment of calcium can be found inside this gap, slightly more oriented towards the SAL side, whereas in the dense rim only silicon is present. The calcium enrichment most likely is related to the calcite precipitation as observed in the Raman experiments. However, it is not possible that the gap is filled with calcite, as the BSE contrast is lower compared to the glass and calcite has a higher density. A likely explanation is that a thin layer of calcite is located on the outer part of the plain SAL and the spatial resolution of the method is not good enough to resolve it properly. For interpretation it must be considered that the EMP technique is — in this magnification – close to its spatial resolution boundaries. Furthermore, the glass consists of more elements, which were not analyzed. The *in situ* Raman data suggests that the outermost corrosion product is a calcium silicate hydrate (most likely smectite (Gerrit Müller, 2019)), followed by a calcite layer. A signal from amorphous silica was not detected in any of the acquired Raman spectra. If the dense rim represents the unknown phase, the EMP data does not confirm the theory of it being a CSH phase, as no calcium is present. The calcite, as a strong Raman scatter, dominates the whole corrosion zone and has obviously completely veiled the amorphous silica signal from the SAL. This can be inferred by looking at the dimension found in the EMP analysis, where a thin, barely visible calcite layer was found besides a thick plain SAL. Finally, it is possible that the corrosion zone has undergone major changes during the drying process.

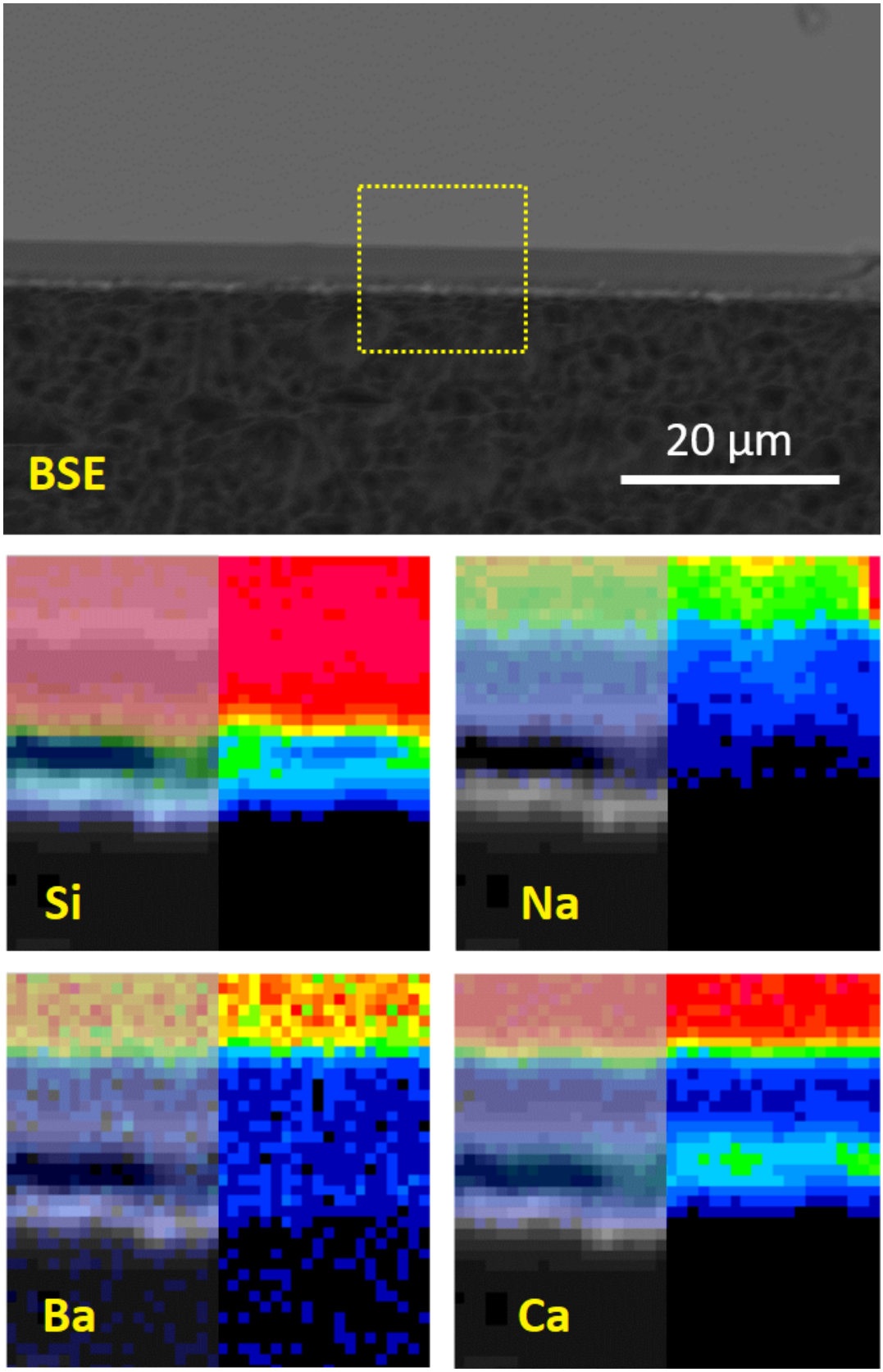

Fig. 5.17.: EMP analysis of *in situ* experiment #2. Shown are a BSE image of the corrosion zone and chemical distribution maps (Si, Na, Ba, Ca) of the region marked with a yellow rectangle. On these, the BSE image of the respective region is superimposed on the left hand side.

5.2.5. Experiment #7 and #8 - Irradiated TBG

The experiments presented in this chapter are conducted with irradiated TBG samples to contribute to the nuclear waste management discussion. The data was acquired as part of the bachelor thesis (Lönartz, 2018) and has been published in Lönartz et al. (2019). The TBG samples were irradiated in Darmstadt at beamline M1 of the UNILAC linear accelerator at the GSI Helmholtz Center for Heavy Ion Research. A gold ion beam with a total energy of 4.8 MeV per nucleon generated an incoming amount of energy on the sample surface of 4.5 MeV. The samples were irradiated with a total energy of approximately 890 MeV, while a fluency of $5x10^{12}$ ions/cm^2 was used. A penetration depth of 48 µm was calculated with the SRIM code (Ziegler et al., 2010) by Maik Lang in 2017 (blue line in Figure 5.18). This theoretical calculation is supported by a Raman line scan conducted from the surface through the damaged zone into the pristine glass revealing a frequency shift of the Q^3 band (red circles in Figure 5.18) which is in good agreement with the SRIM code calculations.

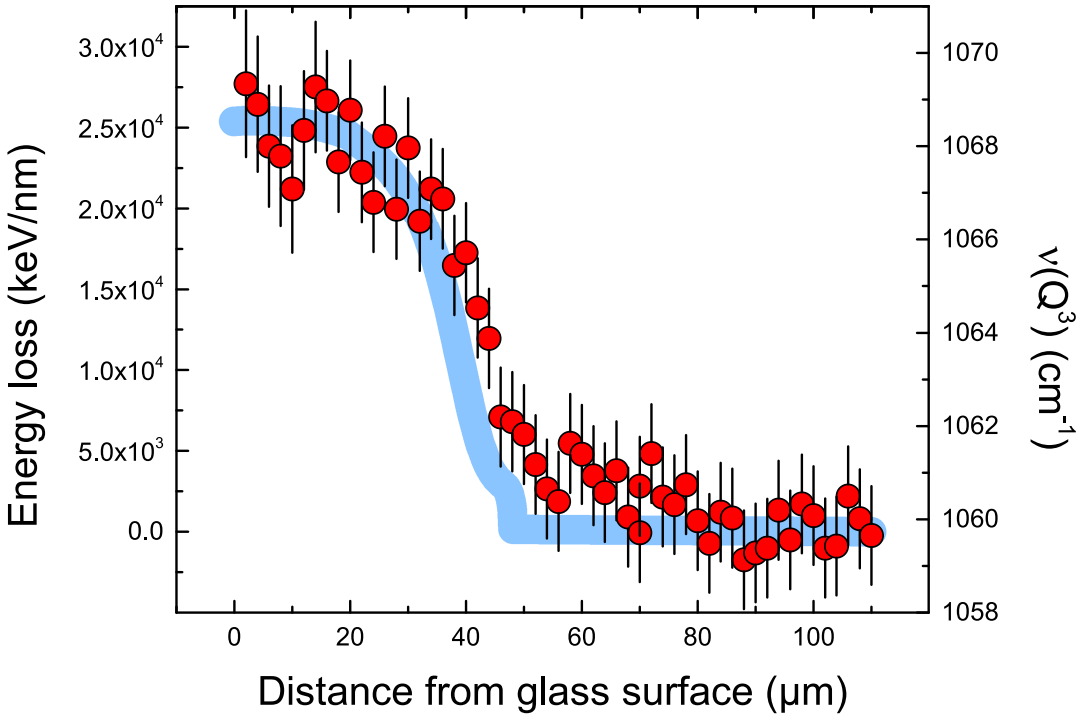

Fig. 5.18.: The energy loss of 4.8 MeV/u Au ions calculated with the SRIM code Ziegler et al. (2010) (dashed gray line) and the frequency of the Q^3 Si−O stretching mode (red circles) as a function of depth. Note the good agreement between the SRIM calculation, indicating a maximum Au penetration depth of 48 ± 5 µm, and structural changes reflected by the shift of the frequency of the Q^3 band. Figure is taken from Lönartz et al. (2019).

In Figure 5.19a, two representative average $R(v)$ Raman spectra from one of the irradiated samples are plotted. The red spectrum was obtained in the irradiated and the blue one in the non-irradiated zone. The spectra were fitted with 15 Gauss functions to assess the quantitative changes after the irradiation. However, it is noted that the least-squares fitting of silicate glass

Raman spectra is still a matter of debate Efimov (1999). A detailed discussion can be found in Lönartz et al. (2019).

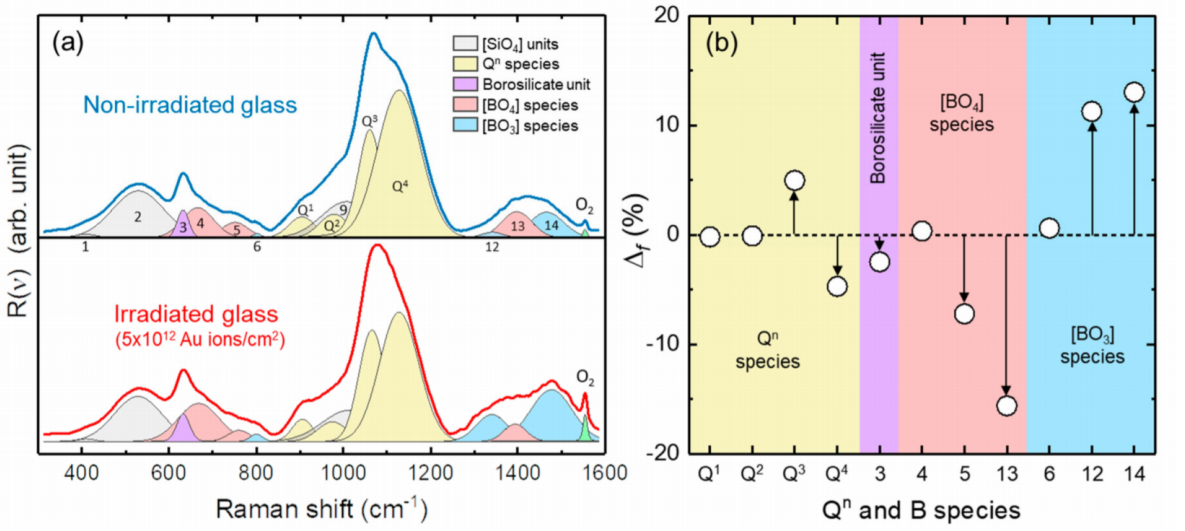

Fig. 5.19.: (a) Representative background corrected $R(v)$ Raman spectra from non-irradiated zone (blue) and irradiated (red) zone of the TBG. Both spectra are least-squares fitted with 15 Gauss functions representing Raman bands engendered by the silicate network (1, 2, 7, 8, 9, 10, 11), boron units (3, 4, 5, 6, 12, 13, 14) and O_2 (15). Stretching motions of the SiO_4 units are labeled with Q^n notation (n=number of bridging oxides). **(b)** Plotted are the differences $\Delta_f = f_(irr) - f_(non - irr)$ between the respective integrated band intensities of the irradiated ($f_(irr)$) and non-irradiated ($f_(non - irr)$) zone of the TBG sample used for the *in situ* Raman experiment. Figure is taken from Lönartz et al. (2019).

The broad peak at ~500 cm^{-1} (Figure 5.19a, band 2), stemming from the (Si−O−Si) bending and rocking modes shifts slightly to higher wavenumbers upon irradiation, most likely reflecting a decrease in the mean Si−O−Si angle due to irradiation (Mir et al., 2017). Additionally, significant changes are visible in the Q^n-species region, whereas n indicates the number of bridging oxygen atoms. The Raman spectrum of the irradiated glass reveals less Q^4 and more Q^3 species (Figure 5.19b). Altogether, the changes in the Raman spectrum indicate a depolymerization of the silicate network.

Additionally, significant changes in boron subnetwork are visible. The Danburite-like groups (Figure 5.19a, band 3), consist of two Q^4 and two BO_4 units, shows a slight decrease in the irradiated glass. This is consistent with the coupled decrease in BO_4 units and increase in BO_3 species (Figure 5.19b). Furthermore, an increase in the O_2 band intensity is visible in the irradiated glass (Figure 5.19b, band 15). It is to note that the O_2 intensity measured for the non-irradiated glass stems from the air in the beam path. These findings are in full agreement with Mir et al. (2017), who also observed the O_2 band intensity increasing after irradiation of a ternary sodium borosilicate glass with ^{129}Xe ions.

Two fluid-cell experiments were conducted for ~45 and ~75 hours with the irradiated sample, which was cut in a half. Both monoliths were corroded in a 0.5 molar Na_2CO_3 solution at a nominal temperature of 90 °C. Calculations of the temperature (cf. Section 4.4.3) resulted in

actual values of 82.6 ± 0.3 °C and 80.0 ± 0.2 °C for experiments #7 and #8, respectively. As the dissolution of the glass was comparatively fast in the experiments, the obtained intensity distributions were, in some cases, incomplete. Hence, the glass retreat was determined by fitting an exponential function to the profiles and determining the intersection with a selected value on the ordinate (cf. Section 4.4.1). The contour plots for the H_2O stretching modes and the Q^n-species region are displayed in Figure 5.20a-d. The extracted glass retreat rates for both experiments are plotted in Figure 5.20e and f, with the respective rate versus time plots displayed in the inset. Due to a software crash during experiment #8, the maps acquired in the first five hours were lost. However, mapping was conducted prior to the actual start of the experiment to find the solution/glass interface and this value could be used for the retreat plot. The contour plot of the water stretching modes has an intensity hole between roughly 20 and 80 hours, which is most likely caused by a gas bubble. In the glass retreat data, by contrast, no influence is perceptible. In both retreat plots, two rate regimes are visible. The rate is considerably faster within the first 10 hours of the respective experiment. The rate drops after ∼40 µm of the glass are dissolved, which corresponds to that part of the glass, which was damaged by the irradiation. Both rates represent the initial rate r_0, as in none of the acquired spectra a signal was found for amorphous silica. The rate for the irradiated glass (r_0^{irr}) was determined by fitting a straight line to the rate-versus-time plot. The results (5.1 ± 0.4 for experiment #7 and 5.5 ± 0.5 for experiment #8) are in good agreement with the respective results obtained derivate versus time plots. Both initial rates r_0^{irr} are considerably higher compared to all other experiments conducted in this thesis.

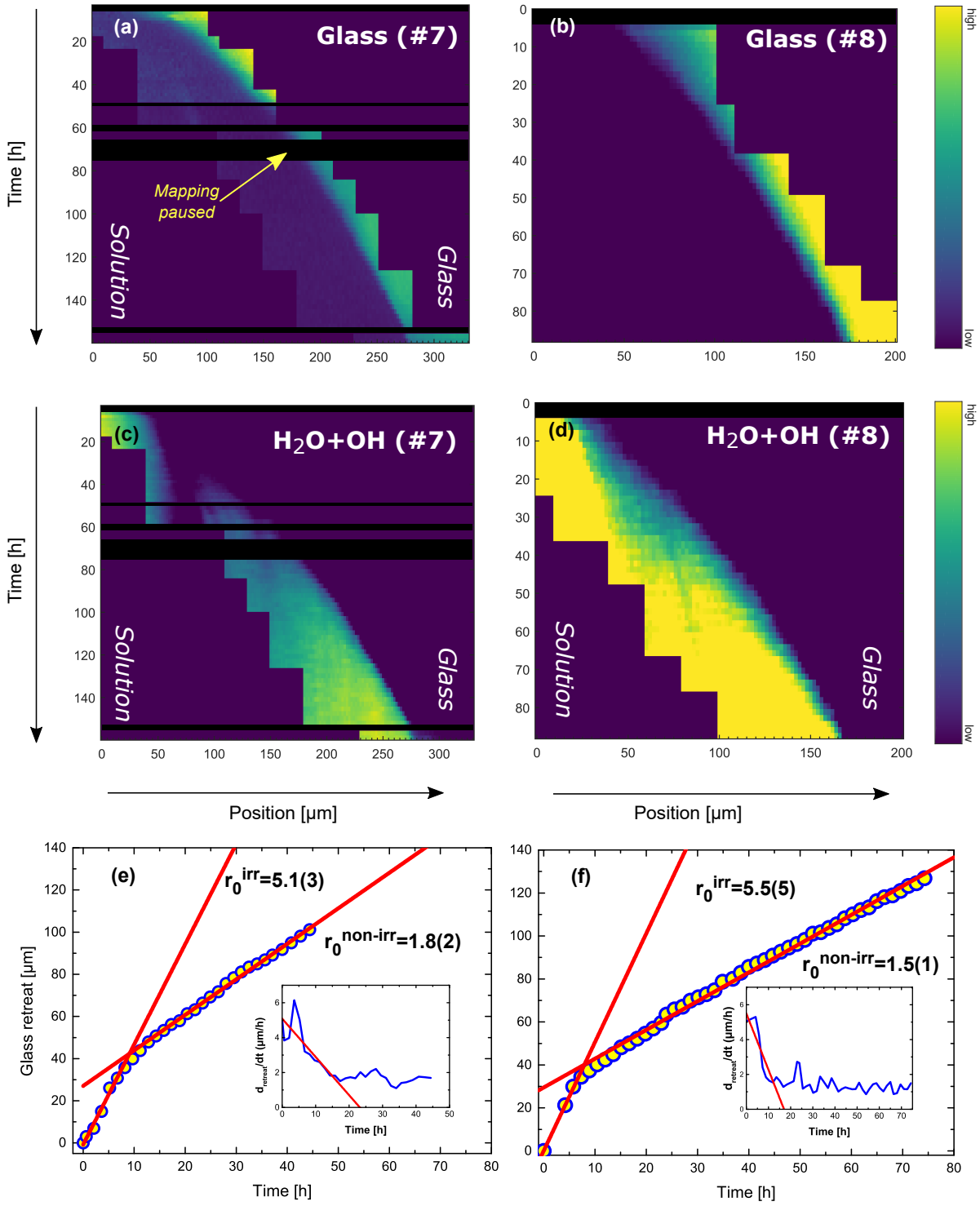

Fig. 5.20.: Raman spectra of the irradiated TBG (red) and the non-irradiated TBG (blue)**(a)**. Fraction of Q^n-species **(b)**. The increase in Q^3 and decrease in Q^4 represents the depolymerization of the glass network in the irradiated glass.

CHAPTER 6

Discussion

Some intriguing observations were made in this work with the novel fluid-cell, hyperspectral Raman imaging approach, which can all be explained by an ICDP process as underlying mechanism for glass corrosion. Theoretically postulated features like an interfacial fluid and a fluid-boundary layer were observed *in situ* for the first time. Furthermore, corrosion rates were measured with so-far unmatched temporal resolution and were found to contradict the affinity rate law by Grambow and Müller (2001). These points will be addressed in detail below, after the discussion of the method development mentioned in the introduction.

- **Corrosion rates:** Glass corrosion rates under static conditions are usually determined by a set of batch experiments and a subsequent solution analysis (e.g., Geisler et al. (2010)) or by the removal of a small amount of the solution during the experiment (e.g., Gin et al. (2013b)). For the latter method, a disturbance of the experiment is unavoidable, as fluctuations in the solution can appear and the S/V ratio is changed. If a set of batch experiments is used, the data is obtained from different samples. In this work, a method has been developed to follow the glass retreat *in situ* by confocal Raman spectroscopy, without any disturbance during the experiment. Fitting of the Raman intensity profiles with a sigmoidal function delivered glass/water or glass/SAL boundary positions with high precisions. Even for the stable AR-GLAS®, it was possible to determine the glass retreat with a high resolution. As known from experiment #6, the rate slows down from the beginning. Nevertheless, to gain an impression of the error, it is reasonable to fit a linear function to the glass retreat data after the first 100 hours, which gives an r^2 of 0.987. The root-mean-square error of this data lies at 0.4 µm, thus proving a sub-µm resolution of the relative position. The 95% prediction interval for this data is plotted below. A value from the same population hereby lies within a range of around ± 0.5 micrometers.

  In the experiments with the irradiated TBG, it was possible to determine two separate rates for the 50 µm thick damaged zone and the undamaged glass, respectively. With

other techniques, the acquisition of similar data would be impossible, as the glass dissolution was remarkably fast. In this work, several experiments were conducted under the same conditions but at different temperatures. An overview of all rates determined in this work is given in Table 6.1. In two cases, a renewal of the residual rate (stage III behavior) has been observed. In one case (experiment #6), the solution was exchanged and the rate increase can be explained by an increased silicon affinity in the bulk solution. For experiment #11, however, no extrinsic trigger, e.g., precipitated phases, is evident. All initial rates obtained for the TBG are plotted in Figure 6.2 as a function of the reciprocal temperature, i.e., in an Arrhenius diagram. The blue circles are the respective r_0 values for experiments #3, #4, #6, #7 and #8, together with the two values determined for the irradiated TBG (r_0^{irr}) in red. The blue straight line represents a linear fit to the five data points obtained for the non-irradiated TBG. The 1-sigma (68.27%) confidence interval of the fit is also given. All values lie within the three-standard deviation. The activation energy calculates to ~69 kJ/mol, which is a reasonable value for glasses. However, considering the considerable error of the slope, the obtained value is more of a ballpark figure. From the graph it is evident that the irradiated sample rates do not plot together with the other TBG samples.

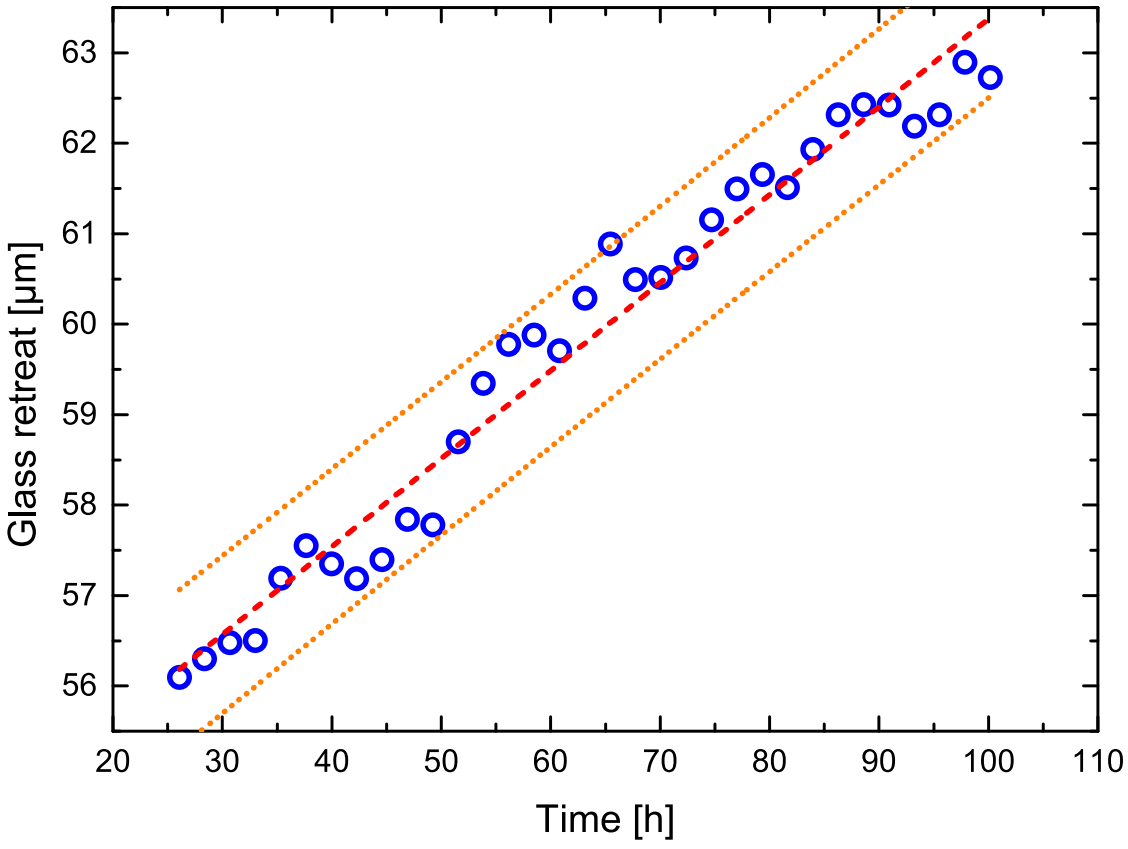

Fig. 6.1.: Linear fit to the retreat data of experiment #2 between 25 and 100 hours. The root-mean-square error of the fit is 0.4 representing the standard deviation from the linear fit.

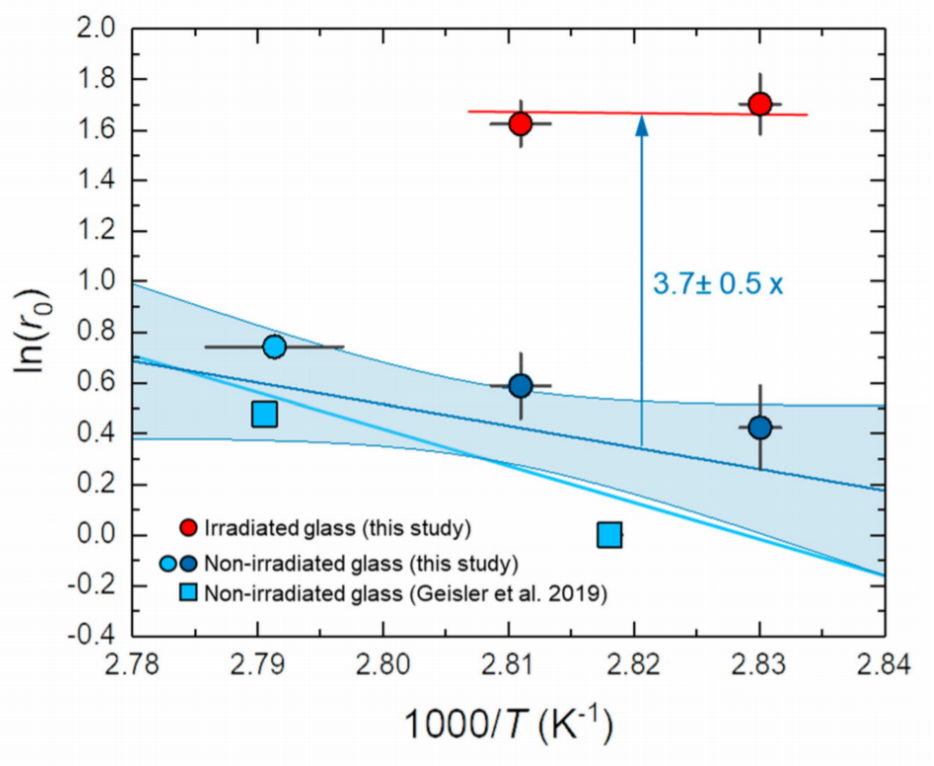

Fig. 6.2.: Arrhenius diagram for all TBG r_0 values obtained in this thesis. It is to note that the values for the irradiated zone (red) of the TBG are significantly higher compared the others (blue). The dark and light blue lines represent an unweighted and an error-weighted linear fit to the data, respectively. For the unweighted fit the 1-sigma confidence interval is also shown as the fit was used to estimate the rates and its error. The figure is taken from Lönartz et al. 2019.

Table 6.1.: Rates and errors determined in this work. For experiment #11 the nominal temperature was 90 °C.

Experiment	**T$_c$ [°C]**	r_0 **[µm/h]**	r_1 **[µm/h]**	r_2 **[µm/h]**
#1	98.7(5)		0.63(1)	
#2	91.0(2)	0.110(2)		
#3	85.1(7)	2.10(3)	0.042(5)	
#4	81.7(1)	1.00(3)	0.057(6)	
#6	85.2(2)	1.61(4)	0.006(3)	0.110(4)
#7	82.6(3)	1.8(2)		
#7^{irr}	82.6(3)	5.1(4)		
#8	80.0(2)	1.5(1)		
#8^{irr}	80.0(2)	5.5(5)		
#11		1.1(1)		0.477(6)

- **pH values:** In this work, a method was developed to calculate the solution pH value from Raman spectra. Therefore, the $\nu_5(CO_3)$-to-$\nu_1(CO_3)$ ratio of the bicarbonate solution was used, together with relative molar scattering cross sections found in the literature. In most cases, the results corresponded quite well with the PHREEQC calculations. Merely in one experiment, a dead pixel on the CCD camera made it impossible to obtain good results. Here, only a relative evaluation was possible. For future work, the idea should be extended to other speciating soluble ion systems. The main sulfate ion species, for example, changes between pH 0 and 4 from HSO_4^- to SO_{42}^- . Phosphate ion speciation actually changes over the whole pH range. Alexander Nazarenko used the Raman spectra of a 0.2 molar phosphate solution to show his students that common pH meters actually measure the proton content in solution. Spectra of the phosphate band in the pH range from 4 to 10 are plotted in Figure 6.3.

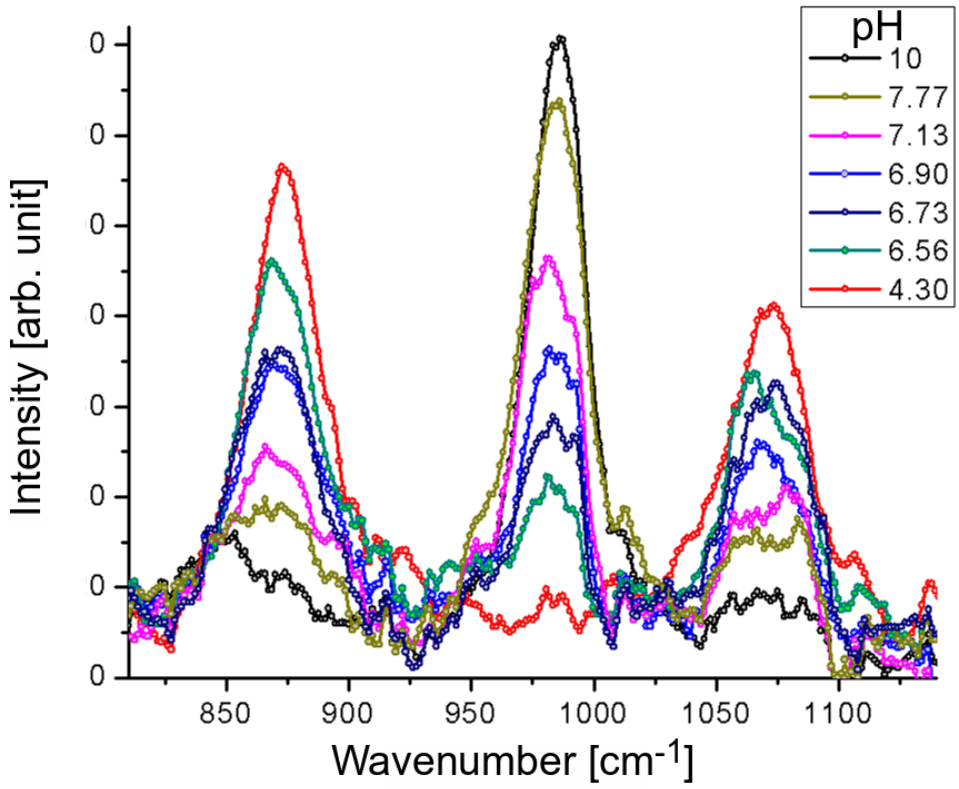

Fig. 6.3.: Raman spectra of a 0.2M phosphate solution at room temperature and different pH. The pH was adjusted by titration with sodium hydroxide. Figure modified after Nazarenko (2019). The change in pH causes a change in the phosphate speciation which is expressed in the band ratio changes.

In a study by Parruzot et al. (2018) a fiber probe was used to collect *in situ* Raman spectra from the solution in which a glass powder was corroded. The authors used the boron species $B(OH)_3$ and $B(OH)_4^-$ to calculate the solution pH with a chemometric model based on principle component analysis. In the case of confocal Raman spectroscopy the boron concentration is to low to apply the method.

- **Temperature calibration:** In this work it was shown that the calculation of the temperature in a bicarbonate solution with the frequency of the $\nu_5 HCO_3$ and a preliminary calibration is possible. Hereby, the accuracy is strongly dependent on the signal-to-noise ratio of the spectra. An average temperature was calculated for every experiment, resulting in a small error because of the large number of values. To increase the accuracy for every single spectrum, the number of spectra in a map would have to be decreased and the acquisition time increased. Temperature contour plots revealed that the solution temperature does not show considerable fluctuations over time. In most of the experiments, the maps contained three lines in 5 µm distance, to get an impression of how even the corrosion front is. In none of the experiments an uneven front was observed in the range of the spatial resolution. Consequently, it is recommended for future experiments to acquire single line scans with the same duration for one scan instead of the maps. That would provide a better signal-to-noise ratio and improve the extraction of information from the dataset.

- **Fluid-cell:** The first fluid-cell that was constructed was used for all experiments reported in this work. As some problems occurred with the setup, a new cell was designed. One problem was the sheer weight of the cell's steel body. The cell was always fixed in its position with double-sided tape, which softens due to the steel body's high temperature. That caused a shift during the settling of the cell into its final position, expressed as an offset in the contour plots and glass retreat data. The massive steel body was actually meant to guarantee an even temperature distribution. The lid was made of steel, as well, which was in contact with the solution during the experiment. On this lid, signs of oxidation were found after the experiments. Thus, an interaction with the solution and an influence on the experiment cannot be excluded. Another source of error is heating with four separated resistors, which may lead to an inhomogeneous temperature distribution. Based on these observations, the improved design includes a round resistor covering the whole bottom of the cell, which should ensure a more homogeneous temperature in the cell and a possibility to conduct *in situ* impedance spectroscopy. Furthermore, the body of the new cell is completely made of the inert material PEEK™. The scope of an ongoing PhD Thesis by Moritz Fritzsche (founded by Otto-Schott-Fonds) is to advance the *in situ* setup further. The new fluid-cell setup is capable of long-term experiments and electrical impedance spectroscopy.

With fluid-cell Raman spectroscopy it was possible, by using isotope tracer, to follow the transport of water through an existing SAL and to calculate its diffusion coefficient. The obtained results have impactions for the glass corrosion mechanism as immanent features of an ICDP process have been observed.

i **Interfacial Fluid:** An immanent feature of an ICDP process is the interfacial fluid, which is located between the SAL and the glass. In the model framework, a thin water film is required here to drive the glass dissolution and to precipitate amorphous silica from it. In all TBG experiments conducted in this work, a water-rich zone was detected *in situ* (cf. contour plots in the results section). Using *post mortem* techniques, an interfacial fluid would lead to a gap between the SAL and the glass, which has been found in many studies (Sterpenich and Libourel, 2006; Anaf, 2010; Geisler et al., 2010; Dohmen et al., 2013) and was confirmed in this work (Section 4.1.1). The formation of such a gap and associated flaking has not received much attention in the community of nuclear waste glass research, possibly because it was mistaken as a feature merely related to shrinking effects during drying of the SAL. In Figure 5.9c, a BSE image of the corrosion zone of the sample corroded in experiment #4 is shown. As described in the results section, no clear gap can be observed at the glass-SAL interface, merely an erratic cracking in this zone - most likely due to SAL drying - is visible. However, the BSE contrast of the SAL gradually decreases towards the glass, which strongly indicates an increase in porosity. To explain this finding, one must consider ripening of amorphous silica and the chemical composition of the TBG. In a TEM study by Lenting (2018), it could be shown that the gap can have an extension of only a few nanometers. The glass used for the study was the international simple glass (ISG) with a high Si fraction and a low content of readily soluble cations compared to the TBG. During the dissolution of the TBG, a comparatively low amount of Si released into the interfacial solution. When the amorphous silica precipitates in the volume formerly occupied by the glass, a silica phase with high porosity will be the result, as sodium and boron is not incorporated in the SAL in significant amounts. During the further course of the corrosion, the amorphous silica undergoes a ripening process with formation of siloxan bonds and accumulation of molecular water, resulting in a denser outer SAL (visible in Figure 5.9c). It must be noted that, due to spatial resolution limitations, Raman spectra obtained at the interfacial fluid are superimposed with glass and SAL signals. It therefore cannot be concluded from the spectra that the water content is as high as in the bulk solution. Nevertheless, the $\nu(H_2O)$ band intensity is 1.5-times higher compared to the center of the SAL. In the case of the TBG, the interfacial fluid is most likely represented by a solution with high salinity and content of silica agglomerates. Generally, the extension and composition of an interfacial fluid is strongly dependent on the glass chemistry. With Raman spectroscopy, it was not possible to determine whether the gel point had been exceeded in this zone, as no major structural reorganization was observed.

ii **Fluid Boundary Layer:** Remarkably, already at the beginning of the experiments #4 and #6, a steep pH gradient of about one pH unit had developed towards the glass surface (cf. contour plots in the results section). Even for the comparatively slow-corroding AR-GLAS® (experiment #2), the development of a slight gradient has been observed. This pH gradient marks a solution boundary layer with a width of about 50 µm at the dissolving glass surface that persisted over the entire time scale of the experiment and later extended into the SAL. The pH increase can be explained by the release of cations (especially Na^+) during the dissolution of the glass, which is coupled to an increase in the OH^- concentration to maintain charge balance. The accumulation of the Na^+ ions near the solid surface might be due to the retention of Na^+ at the surface to compensate for the negative surface charge of the glass and amorphous silica. Consequently, the pH value at the glass surface is different from the pH value of the bulk solution, thus challenging the use of bulk solution data to model glass surface reactions. Such an observation is fully in line with results from *in situ* studies on mineral replacement reactions using interferometry (Icenhower and Steefel, 2015) and microelectrodes (Ruiz-Agudo et al., 2016). These studies also revealed compositional and pH gradients at the reacting mineral surfaces during replacement reactions, reaching length scales from a few micrometers to even several hundreds of micrometers.

iii **Rate drop:** In experiments #3, #4 and #6, a rate drop was observed before or with SAL precipitation. The rate was found to have decreased from the start of the experiment on and dropped to values nearby zero as the SAL had reached a critical thickness. In the case of experiment #6, this critical thickness corresponds to 25 micrometers. The isotope tracer study provides proof that the SAL is not fully protective against water transport, which rules this out as the rate-limiting step. However, the SAL may slow down the effective transport of polymeric silica species and colloidal silica particles, as well as other elements, away from the glass dissolution front. This can lead to an enrichment of silica particles and sodium cations in the interfacial solution, which could explain the observed high pH value. The theory that the SAL is a transport barrier for silica is fully consistent with results from other isotope tracer studies that showed limitations for silica transport (Geisler et al., 2015; Gin et al., 2015; Lenting, 2018). The interfacial solution postulated here would have a high salinity. Under such conditions, silica polymers are known to aggregate to a 3D network (Iler, 1979), trapping H_2O molecules and cations. This additionally would lead to kinetic hindering of silica detachment from the glass into the interfacial fluid. Consequently, the interfacial fluid — as soon as it has formed — controls the porosity, molecular structure and chemistry of the SAL. The observed resumption of the retreat rate in experiment #6 can be explained by the reduced chemical activity of amorphous silica in the bulk solution, leading to the formation of a steeper concentration gradient towards the interfacial fluid. A rate drop was also observed in experiment #2, simultaneously with the precipitation of calcite. Based on the evolution of the water-rich zone observed in the contour plot of the

experiment, it can be assumed that the plain SAL — found in the BSE images — starts to evolve after or together with calcite precipitation. This is in accordance with the ICDP model, as the calcite forms a barrier behind which the formation of an interfacial fluid is facilitated. The observation of a plain and dense SAL here suggests a strong correlation between glass dissolution and amorphous silica precipitation. In experiment #11, the rate dropped after a ∼10 µm thick SAL had evolved. The following rate resumption can be interpreted by considering the outermost layer of the SAL as a diffusion barrier for the THAM buffer. A pile-up of buffer species at the interfacial fluid with time would change the silica particle sizes and negate the passivating effect of the SAL. Evidence for that is delivered by monitoring the THAM concentration at the interface. A decoupling of the buffer diffusion and reaction interface velocities would lead to a decrease in the Stage III rate, which can be observed in the glass retreat plot. The consequence of this finding is that experimental data obtained for glass corrosion experiments buffered with THAM and displaying SAL formation may have been interpreted incorrectly in the past.

In this work, considerable experimental evidence was found supporting the ICDP model. In fact, the precipitation of amorphous silica was detected in experiment #6 and found to have no effect on the constant rate decrease that was observed already from the beginning of the experiment. This observation contradicts the affinity rate law proposed by Grambow and Müller (2001). In this model framework, the corrosion rate should fall to zero as soon as the saturation with respect to silica has been reached in the bulk solution. It is not reasonable that in the experiment #6, amorphous silica precipitated from a silicon-undersaturated solution. However, the observation supports the finding of Icenhower and Steefel (2013), who found that even low amounts of silicon added to a corrosion experiment lead to significant deviations from the affinity rate law, which was only capable of explaining the corrosion kinetics in strongly diluted solutions.

The results presented in this work delivered indisputable proof for an ICDP process like discussed above. On the other hand Gin et al. (2018) found evidence for the interdiffusion model. Although the authors enriched the corrosion solution with ^{29}Si the one micron thick SAL (depleted with respect to boron) kept the natural isotopic abundance of the glass. This discrepancy can only explained by one hypothesis: Both models are correct and applicable - for the particular case with its particular set of parameters. Lenting et al. (2018) found an interdiffusion zone and concluded that both processes take place at the same time but a leached layer can only be found if the inward moving ICDP reaction front is slowed down to such an extend that the ID process is faster. This unifying model is capable of explaining the results of Gin et al. (2018). With the solution enriched in silica the affinity is low in the bulk solution and the breakage of siloxan bonds would be kinetically hindered like explained above for the high saline interfacial fluid. This could have led to an inhibition of the ICDP process with the formation of a leached layer engendered by the faster interdiffusion reaction.

CHAPTER 7

Conclusion and outlook

This work delivers evidence that fluid-cell Raman spectroscopy is a powerful tool to observe the corrosion of glasses in aqueous solution. It is shown that phase distributions can be observed with a high spatial and temporal resolution. A method was developed to find the glass retreat that accounts for the broadened phase boundary due to the microscope's spatial resolution. Beyond that, structural features of the solid phase can be examined as well as dissolved species within the solution. For example a parameter for silica gel was introduced (R_n) which gives the polymerization based on the larger-to-smaller Si ring ratio calculated from the Raman spectra. Additionally, carbonate ion speciation in aqueous solution was used to calculate the solution pH from Raman spectra using known scattering cross section and by calibrating the system with PHREEQC modeling results. Apart from bicarbonate, other potential pH tracers — covering the whole pH range — are identified for future work. The applicability of the fluid-cell *in situ* method is not limited to glass/water reactions, in fact, it can be extended to every other solid/liquid interaction as long as the materials are transparent. In terms of glass corrosion the method was capable of showing that crystalline phases, often interpreted as drying products, can precipitate *in situ* (e.g. calcite in experiment #2).

Additionally, light was shed on the mechanism governing silicate glass corrosion. Significant evidence is provided that the TBG glass corrodes, in bicarbonate solution, by an ICDP process. It could be shown that the drop of rate with time, commonly observed in glass corrosion studies, is not necessarily a result of the SAL being protective against water transport. In conclusion, immanent features of an ICDP process, such as the interfacial fluid and the fluid-boundary layer, have been experimentally verified for the first time. The finding, that silicate glass corrosion in aqueous solution is governed by an ICDP process is of major importance for nuclear waste disposal. Current models, predicting the long-term behavior of glasses in repository environments would not be valid anymore, as they are all based on diffusion controlled processes. However, in this work only two glasses were examined in alkaline solution. To transfer the model to other glasses, fluid-cell Raman experiments need to be conducted on

a larger timescale and in acidic solution or Milli-Q®.

In a consecutive and ongoing PhD work by Moritz Fritzsche, founded by the Otto-Schott-fond, a new generation of fluid-cells have been designed which are used for long-term experiments (6-12 months), which opens the possibility to study more refractory glasses. The new fluid-cell is equipped with two electrodes resting in the solution to conduct electrical impedance spectroscopy over the whole run of the experiment. Beyond that, the findings of this work and the theses by Christoph Lenting, Mara Lönartz and Gerrit Müller are combined to elaborate a clearly defined model framework for an ICDP process for glasses. Based on that, the development of a numerical code was the main scope of this PhD thesis. This numerical code should be capable to explaining experimental findings and represents a new approach for predicting the long-term behavior of nuclear waste glasses in repositories.

Bibliography

Aagaard, P. and Helgeson, H. C. Thermodynamic and kinetic constraints on reaction rates among minerals and aqueous solutions; i, theoretical considerations. *American Journal of Science*, 282(3):237–285, 1982. ISSN 0002-9599. doi: 10.2475/ajs.282.3.237.

Abd-Allah, R. Chemical cleaning of soiled deposits and encrustations on archaeological glass: A diagnostic and practical study. *Journal of Cultural Heritage*, 14(2):97–108, 2013. ISSN 12962074. doi: 10.1016/j.culher.2012.03.010.

Advocat, T., Crovisier, J. L., Vernaz, E., Ehret, G., and Charpentier, H. Hydrolysis of r7t7 nuclear waste glass in dilute media: Mechanisms and rate as a function of ph. *MRS Proceedings*, 212:41, 1990. ISSN 1946-4274. doi: 10.1557/PROC-212-57.

Aguiar, H., Serra, J., González, P., and León, B. Structural study of sol–gel silicate glasses by ir and raman spectroscopies. *Journal of Non-Crystalline Solids*, 355(8):475–480, 2009. ISSN 00223093. doi: 10.1016/j.jnoncrysol.2009.01.010.

Anaf, W., editor. *Study on the formation of heterogeneous structures in leached layers during the corrosion process of glass*, volume EGG 1, 2010. Association CeROArt asbl. ISBN 1784-5092.

Arab, M., Cailleteau, C., Angeli, F., Devreux, F., Girard, L., and Spalla, O. Aqueous alteration of five-oxide silicate glasses: Experimental approach and monte carlo modeling. *Journal of Non-Crystalline Solids*, 354(2-9):155–161, 2008. ISSN 00223093. doi: 10.1016/j.jnoncrysol.2007.06.095.

Barbera, G., Barone, G., Crupi, V., Longo, F., Majolino, D., Mazzoleni, P., Sabatino, G., Tanasi, D., and Venuti, V. Study of late roman and byzantine glass by the combined use of analytical techniques. *Journal of Non-Crystalline Solids*, 358(12-13):1554–1561, 2012. ISSN 00223093. doi: 10.1016/j.jnoncrysol.2012.04.013.

Bernath, P. F. *Spectra of atoms and molecules*. Oxford Univ. Press, Oxford, 2. ed. edition, 2005. ISBN 978-0-19-517759-6.

Bethge, K., Gruber, G., and Stöhlker, T. *Physik der Atome und Moleküle: Eine Einführung*. Lehrbuch Physik. Wiley-VCH, Weinheim, 2., erw. und überarb. aufl. edition, 2004. ISBN 3-527-40463-5.

Brewster, D. Xix.—on the structure and optical phenomena of ancient decomposed glass. *Transactions of the Royal Society of Edinburgh*, 23(02):193–204, 1863. ISSN 0080-4568. doi: 10.1017/S0080456800019372.

Brinker, C. J. and Scherer, G. W. *Sol-gel science: The physics and chemistry of sol-gel processing*. Academic Pr, Boston Mass. u.a., 1990. ISBN 0-12-134970-5.

Brooker, M. H., Hancock, G., Rice, B. C., and Shapter, J. Raman frequency and intensity studies of liquid h2o, h218o and d2o. *Journal of Raman Spectroscopy*, 20(10):683–694, 1989. ISSN 03770486. doi: 10.1002/jrs.1250201009.

Bunker, B. C. Molecular mechanisms for corrosion of silica and silicate glasses. *Journal of Non-Crystalline Solids*, 179:300–308, 1994. ISSN 00223093. doi: 10.1016/0022-3093(94)90708-0.

Buzgar, N. and Apopei, A. The raman study of certain carbonates. *Anal. Şt. Univ. „Al. I. Cuza" Iaşi.*, pages 97–112, 2009.

Carey, D. M. and Korenowski, G. M. Measurement of the raman spectrum of liquid water. *The Journal of Chemical Physics*, 108(7):2669–2675, 1998. ISSN 00219606. doi: 10.1063/1.475659.

Chemtob, S. M., Rossman, G. R., and Stebbins, J. F. Natural hydrous amorphous silica: Quantitation of network speciation and hydroxyl content by 29si mas nmr and vibrational spectroscopy. *American Mineralogist*, 97(1):203–211, 2012. ISSN 0003-004X. doi: 10.2138/am.2012.3921.

Cox, G. A. and Ford, B. A. The long-term corrosion of glass by ground-water. *Journal of Materials Science*, 28(20):5637–5647, 1993. ISSN 0022-2461. doi: 10.1007/BF00367840.

Crank, J. *The mathematics of diffusion*. Oxford science publications. Clarendon Press, Oxford, 2. ed., reprint edition, 1956. ISBN 0198534116.

Diedrich A. Schmid, Kazushi Miki. Structural correlations in liquid water: A new interpretation of ir spectroscopy: Structural correlations in liquid water: A new interpretation of ir spectroscopy. *The journal of physical chemistry. A*, (111(40)):10119–10122, 2007.

DIN. Glass; hydrolytic resistance of glass grains at 98 °c; method of test and classification; identical with iso 719:1985, 1989-12. URL `https://www.beuth.de/de/norm/din-iso-719/1503871`.

DIN. Glass; resistance to attack by a boiling aqueous solution of mixed alkali; method of test and classification; identical with iso 695:1991, 1994-02. URL `https://www.beuth.de/de/norm/din-iso-695/2234616`.

DIN. Testing of glass - resistance to attack by a boiling aqueous solution of hydrochloric acid - method of test and classification, 2001-03. URL `https://www.beuth.de/de/norm/din-12116/37156377`.

Dohmen, L., Lenting, C., Fonseca, R. O. C., Nagel, T., Heuser, A., Geisler, T., and Denkler, R. Pattern formation in silicate glass corrosion zones. *International Journal of Applied Glass Science*, 4(4):357–370, 2013. ISSN 20411286. doi: 10.1111/ijag.12046.

Efimov, A. M. Vibrational spectra, related properties, and structure of inorganic glasses. *Journal of Non-Crystalline Solids*, 1999(253):95–118, 1999. ISSN 00223093.

Emmons, E. D., Fallas, J. C., Kamisetty, V. K., Chien, W.-M., Covington, A. M., Chellappa, R. S., Gramsch, S. A., Hemley, R. J., and Chandra, D. High-pressure raman spectroscopy of tris(hydroxymethyl)aminomethane. *The Journal of Physical Chemistry B*, 114(17):5649–5656, 2010. ISSN 1520-6106. doi: 10.1021/jp9092892.

Everall, N. J. Confocal raman microscopy: Why the depth resolution and spatial accuracy can be much worse than you think. *Applied Spectroscopy*, 54(10):1515–1520, 2000. ISSN 0003-7028. doi: 10.1366/0003702001948439.

Fowler, J. Iii.—on the process of decay in glass, and, incidentally, on the composition and texture of glass at different periods, and the history of its manufacture. *Archaeologia*, 46 (01):65–162, 1880. ISSN 0261-3409. doi: 10.1017/S0261340900006068.

Frost, R. L. and Dickfos, M. J. Raman and infrared spectroscopic study of the anhydrous carbonate minerals shortite and barytocalcite. *Spectrochimica acta. Part A, Molecular and biomolecular spectroscopy*, 71(1):143–146, 2008. ISSN 1386-1425. doi: 10.1016/j.saa.2007.11.021.

Frugier, P., Ribet, I., and Advocat, T. Effects on composition variations on the alteration kinetics of the uox1., 2001.

Frugier, P., Martin, C., Ribet, I., Advocat, T., and Gin, S. The effect of composition on the leaching of three nuclear waste glasses: R7t7, avm and vrz. *Journal of Nuclear Materials*, 346(2-3):194–207, 2005. ISSN 00223115. doi: 10.1016/j.jnucmat.2005.06.023.

Frugier, P., Gin, S., Minet, Y., Chave, T., Bonin, B., Godon, N., Lartigue, J.-E., Jollivet, P., Ayral, A., de Windt, L., and Santarini, G. Son68 nuclear glass dissolution kinetics: Current state of knowledge and basis of the new graal model. *Journal of Nuclear Materials*, 380 (1-3):8–21, 2008. ISSN 00223115. doi: 10.1016/j.jnucmat.2008.06.044.

Galeener, F. L. Planar rings in glasses. *Solid State Communications*, 44(7):1037–1040, 1982. ISSN 00381098. doi: 10.1016/0038-1098(82)90329-5.

Geisler, T., Janssen, A., Scheiter, D., Stephan, T., Berndt, J., and Putnis, A. Aqueous corrosion of borosilicate glass under acidic conditions: A new corrosion mechanism. *Journal of Non-Crystalline Solids*, 356(28-30):1458–1465, 2010. ISSN 00223093. doi: 10.1016/j.jnoncrysol.2010.04.033.

Geisler, T., Nagel, T., Kilburn, M. R., Janssen, A., Icenhower, J. P., Fonseca, R. O., Grange, M., and Nemchin, A. A. The mechanism of borosilicate glass corrosion revisited. *Geochimica et Cosmochimica Acta*, 158:112–129, 2015. ISSN 00167037. doi: 10.1016/j.gca.2015.02.039.

Geisler, T., Dohmen, L., Lenting, C., and Fritzsche, M. B. K. Real-time in situ observations of reaction and transport phenomena during silicate glass corrosion by fluid-cell raman spectroscopy. *Nature materials*, 2019. ISSN 1476-1122. doi: 10.1038/s41563-019-0293-8.

Genga, A., Siciliano, M., Famà, L., Filippo, E., Siciliano, T., Mangone, A., Traini, A., and Laganara, C. Characterization of surface layers formed under natural environmental conditions on medieval glass from siponto (southern italy). *Materials Chemistry and Physics*, 111(2-3):480–485, 2008. ISSN 02540584. doi: 10.1016/j.matchemphys.2008.04.057.

Gerrit Müller. *Raman spectroscopic ex situ & in situ investigation of the aqueous corrosion of soda-lime silicate glasses.* Master thesis, Rheinische Friedrich-Wilhelms Universität Bonn, Bonn, 2019.

Gin, S., Guittonneau, C., Godon, N., Neff, D., Rebiscoul, D., Cabié, M., and Mostefaoui, S. Nuclear glass durability: New insight into alteration layer properties. *The Journal of Physical Chemistry C*, 115(38):18696–18706, 2011. ISSN 1932-7447. doi: 10.1021/jp205477q.

Gin, S., Frugier, P., Jollivet, P., Bruguier, F., and Curti, E. New insight into the residual rate of borosilicate glasses: Effect of s/v and glass composition. *International Journal of Applied Glass Science*, 4(4):371–382, 2013a. ISSN 20411286. doi: 10.1111/ijag.12048.

Gin, S., Ryan, J. V., Schreiber, D. K., Neeway, J., and Cabié, M. Contribution of atom-probe tomography to a better understanding of glass alteration mechanisms: Application to a nuclear glass specimen altered 25years in a granitic environment. *Chemical Geology*, 349-350:99–109, 2013b. ISSN 00092541. doi: 10.1016/j.chemgeo.2013.04.001.

Gin, S., Jollivet, P., Fournier, M., Angeli, F., Frugier, P., and Charpentier, T. Origin and consequences of silicate glass passivation by surface layers. *Nature communications*, 6:6360, 2015. doi: 10.1038/ncomms7360.

Gin, S., Neill, L., Fournier, M., Frugier, P., Ducasse, T., Tribet, M., Abdelouas, A., Parruzot, B., Neeway, J., and Wall, N. The controversial role of inter-diffusion in glass alteration. *Chemical Geology*, 440:115–123, 2016. ISSN 00092541. doi: 10.1016/j.chemgeo.2016.07.014.

Gin, S., Jollivet, P., Barba Rossa, G., Tribet, M., Mougnaud, S., Collin, M., Fournier, M., Cadel, E., Cabie, M., and Dupuy, L. Atom-probe tomography, tem and tof-sims study of borosilicate glass alteration rim: A multiscale approach to investigating rate-limiting mechanisms. *Geochimica et Cosmochimica Acta*, 202:57–76, 2017. ISSN 00167037. doi: 10.1016/j.gca.2016.12.029.

Gin, S., Collin, M., Jollivet, P., Fournier, M., Minet, Y., Dupuy, L., Mahadevan, T., Kerisit, S., and Du, J. Dynamics of self-reorganization explains passivation of silicate glasses. *Nature communications*, 9(1):2169, 2018. doi: 10.1038/s41467-018-04511-2.

Grambow, B. A general rate equation for nuclear waste glass corrosion. *MRS Proceedings*, 44: 566, 1984. ISSN 1946-4274. doi: 10.1557/PROC-44-15.

Grambow, B. Nuclear waste glasses - how durable? *Elements*, 2(6):357–364, 2006. ISSN 1811-5209. doi: 10.2113/gselements.2.6.357.

Grambow, B. and Müller, R. First-order dissolution rate law and the role of surface layers in glass performance assessment. *Journal of Nuclear Materials*, 298(1-2):112–124, 2001. ISSN 00223115. doi: 10.1016/S0022-3115(01)00619-5.

Grambow, B. and Strachan, D. M. A comparison of the performance of nuclear waste glasses by modeling. *MRS Proceedings*, 112, 1987. ISSN 1946-4274. doi: 10.1557/PROC-112-713.

Gruber, A. Scanning confocal optical microscopy and magnetic resonance on single defect centers. *Science*, 276(5321):2012–2014, 1997. ISSN 00368075. doi: 10.1126/science.276.5321.2012.

Gunasekaran, S., Anbalagan, G., and Pandi, S. Raman and infrared spectra of carbonates of calcite structure. *Journal of Raman Spectroscopy*, 37(9):892–899, 2006. ISSN 03770486. doi: 10.1002/jrs.1518.

Hänsel, H., Neumann, W., Albrecht, F., and Frübing, P. *Moleküle und Festkörper: Mit 27 Tabellen*, volume / Horst Hänsel; Werner Neumann ; Bd. 4 of *Spektrum Lehrbuch*. Spektrum Akad. Verl., Heidelberg, studienausg edition, 2000. ISBN 3827410371.

Hellmann, R., Wirth, R., Daval, D., Barnes, J.-P., Penisson, J.-M., Tisserand, D., Epicier, T., Florin, B., and Hervig, R. L. Unifying natural and laboratory chemical weathering with interfacial dissolution–reprecipitation: A study based on the nanometer-scale chemistry of fluid–silicate interfaces. *Chemical Geology*, 294-295:203–216, 2012. ISSN 00092541. doi: 10.1016/j.chemgeo.2011.12.002.

Hellmann, R., Cotte, S., Cadel, E., Malladi, S., Karlsson, L. S., Lozano-Perez, S., Cabié, M., and Seyeux, A. Nanometre-scale evidence for interfacial dissolution-reprecipitation control of silicate glass corrosion. *Nature materials*, 14(3):307–311, 2015. ISSN 1476-1122. doi: 10.1038/nmat4172.

Herzberg, G. *Infrared and Raman spectra of polyatomic molecules*, volume / by Gerhard Herzberg ; Vol. 2 of *Molecular spectra and molecular structure*. Krieger, Malabar, Fla., 1945. ISBN 0894642693.

Howell, N. K., Arteaga, G., Nakai, S., and Li-Chan, E. C. Y. Raman spectral analysis in the c−h stretching region of proteins and amino acids for investigation of hydrophobic interactions. *Journal of Agricultural and Food Chemistry*, 47(3):924–933, 1999. ISSN 0021-8561. doi: 10.1021/jf981074l.

Icenhower, J. P. and Steefel, C. I. Experimentally determined dissolution kinetics of son68 glass at 90°c over a silica saturation interval: Evidence against a linear rate law. *Journal of Nuclear Materials*, 439(1-3):137–147, 2013. ISSN 00223115. doi: 10.1016/j.jnucmat.2013.04.008.

Icenhower, J. P. and Steefel, C. I. Dissolution rate of borosilicate glass son68: A method of quantification based upon interferometry and implications for experimental and natural weathering rates of glass. *Geochimica et Cosmochimica Acta*, 157:147–163, 2015. ISSN 00167037. doi: 10.1016/j.gca.2015.02.037.

Iler, R. K. *The chemistry of silica: Solubility, polymerization, colloid and surface properties, and biochemistry*. A Wiley-Interscience publication. Wiley, New York, NY, 1979. ISBN 9780471024040. URL `http://www.loc.gov/catdir/bios/wiley041/78023960.html`.

Jégou, C., Gin, S., and Larché, F. Alteration kinetics of a simplified nuclear glass in an aqueous medium: Effects of solution chemistry and of protective gel properties on diminishing the alteration rate. *Journal of Nuclear Materials*, 280(2):216–229, 2000. ISSN 00223115. doi: 10.1016/S0022-3115(00)00039-8.

Kilymis, D., Faivre, A., Michel, T., Peuget, S., Delaye, J.-M., Delrieu, J., Ramonda, M., and Ispas, S. Raman spectra of indented pristine and irradiated sodium borosilicate glasses. *Journal of Non-Crystalline Solids*, 464:5–13, 2017. ISSN 00223093. doi: 10.1016/j.jnoncrysol.2017.03.012.

King, H. E., Plumper, O., Geisler, T., and Putnis, A. Experimental investigations into the silicification of olivine: Implications for the reaction mechanism and acid neutralization. *American Mineralogist*, 96(10):1503–1511, 2011. ISSN 0003-004X. doi: 10.2138/am.2011.3779.

Krassimir Garbev. *Struktur, Eigenschaften und quantitative Rietveldanalyse von hydrothermal kristallisierten Calciumsilikathydraten (C-S-H-Phasen)*, volume FZKA 6877 of *Wissenschaftliche Berichte*. Karlsruhe, 2004.

Krol, D. M. and van Lierop, J. G. Raman study of the water adsorption on monolithic silica gels. *Journal of Non-Crystalline Solids*, 68(1):163–166, 1984. ISSN 00223093. doi: 10.1016/0022-3093(84)90045-0.

Kuznetsova, Y., Neumann, A., and Brueck, S. R. Imaging interferometric microscopy–approaching the linear systems limits of optical resolution. *Optics Express*, 15(11):6651, 2007. ISSN 1094-4087. doi: 10.1364/OE.15.006651.

Lenting, C. *Glass corrosion: Towards a unifying mechanistic model*. Dissertation, Rheinische Friedrich-Wilhelms Universität Bonn, Bonn, 2018.

Lenting, C., Plümper, O., Kilburn, M., Guagliardo, P., Klinkenberg, M., and Geisler, T. Towards a unifying mechanistic model for silicate glass corrosion. *npj Materials Degradation*, 2(1):28, 2018. ISSN 2397-2106. doi: 10.1038/s41529-018-0048-z. URL `https://www.nature.com/articles/s41529-018-0048-z.pdf`.

Liesegang, M., Milke, R., Kranz, C., and Neusser, G. Silica nanoparticle aggregation in calcite replacement reactions. *Scientific reports*, 7(1):14550, 2017. doi: 10.1038/s41598-017-06458-8.

Liu, Y. and Heer, J. Somewhere over the rainbow. In Mandryk, R., Hancock, M., Perry, M., and Cox, A., editors, *Proceedings of the 2018 CHI Conference on Human Factors in Computing Systems - CHI '18*, pages 1–12, New York, New York, USA, 2018. ACM Press. ISBN 9781450356206. doi: 10.1145/3173574.3174172.

Lombardo, T., Gentaz, L., Verney-Carron, A., Chabas, A., Loisel, C., Neff, D., and Leroy, E. Characterisation of complex alteration layers in medieval glasses. *Corrosion Science*, 72: 10–19, 2013. ISSN 0010938X. doi: 10.1016/j.corsci.2013.02.004.

Lönartz, M. I., Dohmen, L., Lenting, C., Trautmann, C., Lang, M., and Geisler, T. The effect of heavy ion irradiation on the forward dissolution rate of borosilicate glasses studied in situ and real time by fluid-cell raman spectroscopy. *Materials (Basel, Switzerland)*, 12(9), 2019. ISSN 1996-1944. doi: 10.3390/ma12091480.

Long, D. A. *Raman spectroscopy*. McGraw-Hill, New York NY u.a., 1977. ISBN 0-07-038675-7.

Longinelli, A., Silvestri, A., Molin, G., and Salviulo, G. 1.8 ka old glass from the roman ship julia felix : glass–water oxygen isotope exchange. *Chemical Geology*, 211(3-4):335–342, 2004. ISSN 00092541. doi: 10.1016/j.chemgeo.2004.07.003.

Ma, T., Jivkov, A. P., Li, W., Liang, W., Wang, Y., Xu, H., and Han, X. A mechanistic model for long-term nuclear waste glass dissolution integrating chemical affinity and interfacial diffusion barrier. *Journal of Nuclear Materials*, 486:70–85, 2017. ISSN 00223115. doi: 10.1016/j.jnucmat.2017.01.001.

Macquet, C. and Thomassin, J. H. Archaeological glasses as modelling of the behavior of buried nuclear waste glass. *Applied Clay Science*, 7(1-3):17–31, 1992. ISSN 01691317. doi: 10.1016/0169-1317(92)90025-I.

Malchow, P., Johanns, K. E., Möncke, D., Korte-Kerzel, S., Wondraczek, L., and Durst, K. Composition and cooling-rate dependence of plastic deformation, densification, and cracking in sodium borosilicate glasses during pyramidal indentation. *Journal of Non-Crystalline Solids*, 419:97–109, 2015. ISSN 00223093. doi: 10.1016/j.jnoncrysol.2015.03.020.

Malfait, W. J., Zakaznova-Herzog, V. P., and Halter, W. E. Amorphous materials: Properties, structure, and durability: Quantitative raman spectroscopy: Speciation of na-silicate glasses and melts. *American Mineralogist*, 93(10):1505–1518, 2008. ISSN 0003-004X. doi: 10.2138/am.2008.2783.

Mercado-Depierre, S., Fournier, M., Gin, S., and Angeli, F. Influence of zeolite precipitation on borosilicate glass alteration under hyperalkaline conditions. *Journal of Nuclear Materials*, 491:67–82, 2017. ISSN 00223115. doi: 10.1016/j.jnucmat.2017.04.043.

Mills, R. Self-diffusion in normal and heavy water in the range 1-45.deg. *The Journal of Physical Chemistry*, 77(5):685–688, 1973. ISSN 0022-3654. doi: 10.1021/j100624a025.

Mir, A. H., Monnet, I., Boizot, B., Jégou, C., and Peuget, S. Electron and electron-ion sequential irradiation of borosilicate glasses: Impact of the pre-existing defects. *Journal of Nuclear Materials*, 2017(489):91–98, 2017. ISSN 00223115.

Nazarenko, A. Quantitative measurements of protonation reactions in solutions, 2019. URL `http://staff.buffalostate.edu/nazareay/jcej/2.htm`.

Neuville, D. R. Viscosity, structure and mixing in (ca, na) silicate melts. *Chemical Geology*, 229(1-3):28–41, 2006. ISSN 00092541. doi: 10.1016/j.chemgeo.2006.01.008.

Newton, R. The enigma of the layered crusts on some weathered glasses, a chronological account of the investigations. *Archaeometry*, 13(1):1–9, 1971. ISSN 0003-813X. doi: 10.1111/j.1475-4754.1971.tb00024.x.

NIST. Basic atomic spectroscopic data - strong lines of neon (ne), 2018.

Ohkubo, T., Gin, S., Collin, M., and Iwadate, Y. Molecular dynamics simulation of water confinement in disordered aluminosilicate subnanopores. *Scientific reports*, 8(1):3761, 2018. doi: 10.1038/s41598-018-22015-3.

Ortaboy, S., Li, J., Geng, G., Myers, R. J., Monteiro, P. J. M., Maboudian, R., and Carraro, C. Effects of co 2 and temperature on the structure and chemistry of c–(a–)s–h investigated by raman spectroscopy. *RSC Adv*, 7(77):48925–48933, 2017. ISSN 2046-2069. doi: 10.1039/C7RA07266J.

Osipov, A. A., Osipova, L. M., and Eremyashev, V. E. Structure of alkali borosilicate glasses and melts according to raman spectroscopy data. *Glass Physics and Chemistry*, 39(2): 105–112, 2013. doi: 10.1134/S1087659613020119.

Parkhurst, D.L. and Appelo, C.A.J. *Description of Input and Examples for PHREEQC Version 3—A Computer Program for Speciation, Batch-Reaction, One-Dimensional Transport, and Inverse Geochemical Calculations*, volume 6 of *Techniques and Methods*. 2013. URL `https://pubs.usgs.gov/tm/06/a43/`.

Parruzot, B., Ryan, J. V., Lines, A. M., Bryan, S. A., Neeway, J. J., Chatterjee, S., Lukins, C. D., and Casella, A. J. Method for the in situ measurement of ph and alteration extent for aluminoborosilicate glasses using raman spectroscopy. *Analytical chemistry*, 90(20):11812–11819, 2018. doi: 10.1021/acs.analchem.8b00960.

Pasquarello, A. and Car, R. Identification of raman defect lines as signatures of ring structures in vitreous silica. *Physical Review Letters*, 80(23):5145–5147, 1998. ISSN 0031-9007. doi: 10.1103/PhysRevLett.80.5145.

Pastorczak, M., Kozanecki, M., and Ulanski, J. Raman resonance effect in liquid water. *The journal of physical chemistry. A*, 112(43):10705–10707, 2008. doi: 10.1021/jp805369p.

Pezzotti, G., Puppulin, L., La Rosa, A., Boffelli, M., Zhu, W., McEntire, B. J., Hosogi, S., Nakahari, T., and Marunaka, Y. Effect of ph and monovalent cations on the raman spectrum of water: Basics revisited and application to measure concentration gradients at water/solid interface in si3n4 biomaterial. *Chemical Physics*, 463:120–136, 2015. ISSN 03010104. doi: 10.1016/j.chemphys.2015.10.010.

Phillips, J. C. Microscopic origin of anomalously narrow raman lines in network glasses. *Journal of Non-Crystalline Solids*, 63(3):347–355, 1984. ISSN 00223093. doi: 10.1016/0022-3093(84)90102-9.

Prochazka, R. Natural corrosion of the uranium-colored historical glasses. *Journal of Non-Crystalline Solids*, 353(18-21):2052–2056, 2007. ISSN 00223093. doi: 10.1016/j.jnoncrysol.2007.01.069.

Putnis, A. Mineral replacement reactions: From macroscopic observations to microscopic mechanisms. *Mineralogical Magazine*, 66(5):689–708, 2002. ISSN 14718022. doi: 10.1180/0026461026650056.

Putnis, A. Materials science. why mineral interfaces matter. *Science (New York, N.Y.)*, 343 (6178):1441–1442, 2014. doi: 10.1126/science.1250884.

Putnis, C. V. Direct observations of pseudomorphism: Compositional and textural evolution at a fluid-solid interface. *American Mineralogist*, 90(11-12):1909–1912, 2005. ISSN 0003-004X. doi: 10.2138/am.2005.1990.

Putnis, C. V. and Ruiz-Agudo, E. The mineral-water interface: Where minerals react with the environment. *Elements*, 9(3):177–182, 2013. ISSN 1811-5209. doi: 10.2113/gselements.9.3.177.

Rey, R., Møller, K. B., and Hynes, J. T. Hydrogen bond dynamics in water and ultrafast infrared spectroscopy. *The Journal of Physical Chemistry A*, 106(50):11993–11996, 2002. ISSN 1089-5639. doi: 10.1021/jp026419o.

Rudolph, W. W., Irmer, G., and Königsberger, E. Speciation studies in aqueous hco3(-)-co3(2-) solutions. a combined raman spectroscopic and thermodynamic study. *Dalton transactions (Cambridge, England : 2003)*, 2008(7):900–908, 2008. ISSN 1477-9226. doi: 10.1039/b713254a.

Ruiz-Agudo, E., King, H. E., Patiño-López, L. D., Putnis, C. V., Geisler, T., Rodriguez-Navarro, C., and Putnis, A. Control of silicate weathering by interface-coupled dissolution-precipitation processes at the mineral-solution interface. *Geology*, 44(7):567–570, 2016. ISSN 0091-7613. doi: 10.1130/G37856.1.

Rupertus, V., Hladik, B., Rothhaar, U., and Scheumann, V. A quick test to monitor the delamination propensity of glass containers. *PDA journal of pharmaceutical science and technology*, 68(4):373–380, 2014. doi: 10.5731/pdajpst.2014.00990.

Saloman, E. B. and Sansonetti, C. J. Wavelengths, energy level classifications, and energy levels for the spectrum of neutral neon. *Journal of Physical and Chemical Reference Data*, 33(4):1113–1158, 2004. ISSN 0047-2689. doi: 10.1063/1.1797771.

Schalm, O. and Anaf, W. Laminated altered layers in historical glass: Density variations of silica nanoparticle random packings as explanation for the observed lamellae. *Journal of Non-Crystalline Solids*, 442:1–16, 2016. ISSN 00223093. doi: 10.1016/j.jnoncrysol.2016.03.019.

Silvestri, A., Molin, G., and Salviulo, G. Archaeological glass alteration products in marine and land-based environments: morphological, chemical and microtextural characterization. *Journal of Non-Crystalline Solids*, 351(16-17):1338–1349, 2005. ISSN 00223093. doi: 10.1016/j.jnoncrysol.2005.03.013.

Smith, N. and van der Walt, S. A better default colormap for matplotlib, 2015. URL `https://bids.github.io/colormap/`.

Spiekermann, G., Steele-MacInnis, M., Schmidt, C., and Jahn, S. Vibrational mode frequencies of silica species in sio2-h2o liquids and glasses from ab initio molecular dynamics. *The Journal of chemical physics*, 136(15):154501, 2012. ISSN 1089-7690. doi: 10.1063/1.3703667.

Stavrou, E., Palles, D., Kamitsos, E. I., Lipovskii, A., Tagantsev, D., Svirko, Y., and Honkanen, S. Vibrational study of thermally ion-exchanged sodium aluminoborosilicate glasses. *Journal of Non-Crystalline Solids*, 401:232–236, 2014. ISSN 00223093. doi: 10.1016/j.jnoncrysol.2013.12.017.

Sterpenich, J. Crystal-chemistry of alteration products of vitrified wastes: implications on the retention of polluting elements. *Waste management (New York, N.Y.)*, 28(1):120–132, 2008. ISSN 0956-053X. doi: 10.1016/j.wasman.2006.11.004.

Sterpenich, J. and Libourel, G. Using stained glass windows to understand the durability of toxic waste matrices. *Chemical Geology*, 174(1-3):181–193, 2001. ISSN 00092541. doi: 10.1016/S0009-2541(00)00315-6.

Sterpenich, J. and Libourel, G. Water diffusion in silicate glasses under natural weathering conditions: Evidence from buried medieval stained glasses. *Journal of Non-Crystalline Solids*, 352(50-51):5446–5451, 2006. ISSN 00223093. doi: 10.1016/j.jnoncrysol.2006.08.041.

Stolen, R. H. Water and its relation to broken bond defects in fused silica. *The Journal of Chemical Physics*, 64(6):2623, 1976. ISSN 00219606. doi: 10.1063/1.432516.

Sun, Q. Raman spectroscopic study of the effects of dissolved nacl on water structure. *Vibrational Spectroscopy*, 62:110–114, 2012. ISSN 09242031. doi: 10.1016/j.vibspec.2012.05.007.

Utton, C. A., Hand, R. J., Bingham, P. A., Hyatt, N. C., Swanton, S. W., and Williams, S. J. Dissolution of vitrified wastes in a high-ph calcium-rich solution. *Journal of Nuclear Materials*, 435(1-3):112–122, 2013. ISSN 00223115. doi: 10.1016/j.jnucmat.2012.12.032.

Verney-Carron, A., Gin, S., and Libourel, G. A fractured roman glass block altered for 1800 years in seawater: Analogy with nuclear waste glass in a deep geological repository. *Geochimica et Cosmochimica Acta*, 72(22):5372–5385, 2008. ISSN 00167037. doi: 10.1016/j.gca.2008.08.018.

Walrafen, G. E., Krishnan, P. N., and Freiman, S. W. Raman investigation of optical fibers under high tensile stress. *Journal of Applied Physics*, 52(4):2832–2836, 1981. ISSN 0021-8979. doi: 10.1063/1.329013.

Wang, X., Conway, W., Burns, R., McCann, N., and Maeder, M. Comprehensive study of the hydration and dehydration reactions of carbon dioxide in aqueous solution. *The journal of physical chemistry. A*, 114(4):1734–1740, 2010. doi: 10.1021/jp909019u.

Wang, Y., Jove-Colon, C. F., and Kuhlman, K. L. Nonlinear dynamics and instability of aqueous dissolution of silicate glasses and minerals. *Scientific reports*, 6:30256, 2016. doi: 10.1038/srep30256.

Winterstein-Beckmann, A., Möncke, D., Palles, D., Kamitsos, E. I., and Wondraczek, L. A raman-spectroscopic study of indentation-induced structural changes in technical alkali-borosilicate glasses with varying silicate network connectivity. *Journal of Non-Crystalline Solids*, 405:196–206, 2014. ISSN 00223093. doi: 10.1016/j.jnoncrysol.2014.09.020.

Yadav, A. K. and Singh, P. A review of the structures of oxide glasses by raman spectroscopy. *RSC Adv*, 5(83):67583–67609, 2015. ISSN 2046-2069. doi: 10.1039/C5RA13043C.

Ziegler, J. F., Ziegler, M. D., and Biersack, J. P. Srim – the stopping and range of ions in matter (2010). *Nuclear Instruments and Methods in Physics Research Section B: Beam Interactions with Materials and Atoms*, 268(11-12):1818–1823, 2010. ISSN 0168583X. doi: 10.1016/j.nimb.2010.02.091.

Zotov, N. and Keppler, H. In-situ raman spectra of dissolved silica species in aqueous fluids to 900 °c and 14 kbar. *American Mineralogist*, 85(3-4):600–604, 2000. ISSN 0003-004X. doi: 10.2138/am-2000-0423.

Zotov, N. and Keppler, H. Silica speciation in aqueous fluids at high pressures and high temperatures. *Chemical Geology*, 184(1-2):71–82, 2002. ISSN 00092541. doi: 10.1016/S0009-2541(01)00353-9.

List of Figures

List of Tables

Danksagung

Mein größter Dank gilt Thorsten Geisler, der mit seiner eigenen Begeisterung für das Thema und seinen vielen guten Ideen diese Arbeit möglich gemacht hat. Stets nahm er sich Zeit und war nie unerreichbar wenn ich fachliche Fragen hatte oder ein Brainstorming nötig war.

Ebenfalls nicht möglich gewesen wäre diese Arbeit ohne die finanzielle Unterstützung der SCHOTT AG. Finanziert wurde das Projekt zu jeweils halben Teilen von der BU Tubing in Mitterteich und dem technischen Service Analytik in Mainz. In den beiden Einheiten waren Reiner Eichholz (BU T) und Markus Kuhr (TSA) für das Projekt verantwortlich. Beide hatten immer ein offenes Ohr wenn es Probleme zu lösen galt und waren auch maßgeblich an der fachlichen Lenkung des Projektes beteiligt. Dasselbe gilt für Peter Nass aus der Forschung und Entwicklung, der immer an fachlichen Diskussionen beteiligt war und begeisterter Forscher ist. Ebenfalls von RD war Michael Schwall für viele Fragen für mich erreichbar und auch er war stets begeistert und brachte viele Ideen in das Projekt mit ein. Bei Simone Ritter möchte ich mich für die Hilfe bei den Versuchsschmelzen bedanken. Bei TSA war vor allem Thomas Korb für mich Ansprechpartner und ohne ihn wäre diese Arbeit ebenfalls nicht zustande gekommen. Er half mir bei der Planung der Reaktionszellen, brachte viele Ideen für das Messsetup mit ein und fand immer irgendwo genau das Teil, dass ich gerade brauchte. Auch bei Ralph Seuwen, Markus Stieglitz und Silke Krause möchte ich mich bedanken, die mich sofort in ihre Arbeitsgruppe aufgenommen haben und mich bis heute an ihrem Raman-Spektrometer messen lassen. Werner Bauer hat die erste Version der Reaktionszelle bei TSA in der feinmechanischen Werkstatt gebaut und auch die oft sehr aufwendige Probenpräparation wurde hier gemacht, wobei mein Dank an alle Mitarbeiter der Präparation geht.

An der Universität Bonn möchte ich mich vor allem bei Christoph Lenting und Kerstin Stange bedanken. Christoph hat das erste in situ Experiment durchgeführt, auf dem diese Arbeit basiert und Kerstin war für mich Ansprechpartnerin für alle Raman-Fragen. Beide haben mir immer fachlich und freundschaftlich beigestanden. Bei Mara Lönartz und Gerrit Müller, deren Abschlussarbeiten ich begleiten durfte möchte ich mich für tolle Diskussionen und Ihren daraus resultierenden Beitrag zu dieser Arbeit bedanken. Das gilt auch für Moritz Fritzsche, der eine aufbauende Dissertation schreibt, die über den Otto-Schott-Fond finanziert wird. Henrik Blanchard und Dieter Lülsdorf haben die zweite Version der Reaktionszelle mit mir geplant und gebaut. Für fachliche Diskussion und andere Unterstützung bedanke ich mich bei Karoline Brückel, Frank Tomaschek, Markus Lagos, Raul Fonseca und natürlich bei Robin Strack. Für das Korrekturlesen danke ich Valerie Brückel, Ralph Seuwen und Angela Thiebes.

Meine Eltern, meine Großeltern und meine Schwester haben mich mein ganzes Leben lang unterstützt und waren immer für mich da. Dasselbe gilt für Angie. Ich freue mich unendlich auf unseren gemeinsamen Sohn.

APPENDIX A

Appendix

A. Matlab scripts

YAVRG.M

```
% Makes average over y values (3 in this case)
function avrg=YAVRG(data)

for x = 1: size(data, 2)
        for y = 1: (size(data, 1)./ylines)
        avrg(y,x)=(data((y-1)*3+1,x)+data((y-1)*3+2,x)+data((y-1)*3+3,x))./3;
        end
end

clear('i','k', 'ylines')
end
```

CONTOURPLOTS.M

```
% Plots data as contour plot with colorcode viridis.
data=pHdata;

fig1=figure;
im1=imagesc(x, t, data); % Put x and y values matrix here
colormap(viridis)
caxis([300 800]);
caxis([min(data(:)).*1.2 max(data(:)).*1]);

colorbar;
%colorbar.Ticks=[7.0 7.2 7.4 7.6 7.8 8.0 8.2 8.4];
%colorbar.TickLabel=[7.0 7.2 7.4 7.6 7.8 8.0 8.2 8.4];
ax=gca;
ax.XMinorTick='on';

ax.Title.String='pH';
ax.XLabel.String='Position [µmm]';
ax.YLabel.String='Time [h]';
ax.XTick=[0 20 40 60 80 100 120 140 160 180 200];
ax.XTickLabel=[0 20 40 60 80 100 120 140 160 180 200];

% Print pdf in same dimensions like figure
fig1=gcf;
set(fig1,'Units','Inches');
pos = get(fig1,'Position');
set(fig1,'PaperPositionMode','Auto','PaperUnits','Inches','PaperSize',[pos(3), pos(4)])
```

```
clear('ax','data','im1','pos')
export_fig B4-temperature.png -transparent -r800
```

CUTGLASS.M

```
% Cuts all values from the map which are larger than matrix (retreat values)
function result=CG(data, retreat, xval)

for i = 1: size(data, 1) % row
        for k = 1: size(data, 2) % column
        result(i,k)= data(i,k);
                if xval(k) > retreat(i)
                result(i,k)=0;
                end
        end
end
end
```

TIMEGAPS.M

```
% Filling of all not mapped times (time gaps) with zeros, to obtain correct y axis labeling.
function result=ZeitMap(data, time)
z=0;
div=0;
for y = 1: size(data, 1)
        div=round(time(y)./0.1);
        for i = 1: div
                z=z+1;
                result(z,:)=data(y,:);
        end
end
clear('y','data','i','div')
end
```

EXPFIT.M

```
% Fit whole dataset of intensity distribution curves with exponential function. Datapoints
are plotted with blue dots, exponential fits with crimson lines and the hight of the y value
which is determined for alle curves as a red dashed line. In this example the cut values for the
```

```
95% confidence intervals are caluculated and plotted.

workv = ans;
h1=figure;
ytocut=35000; %Intensity value at which the y value for the exponential fit will be determined.
hold on

for i=1: size(workv, 2) %i=Number of Intensity destribution curves
        Cut=getlength(workv, i);
        yTemp=workv(Cut(1):Cut(2),i);
        xTemp=xd(Cut(1):Cut(2));
        len=size(xTemp, 1)-5;

        t = ~isnan(yTemp);
        [f,gof,opt]= fit( xTemp(t), yTemp(t), 'exp2', 'StartPoint', [650 -0.0301 0.0036 0.1965],
'Lower', [100 -10 -10 0], 'Upper', [1000 1 100 1]);

        level = tcdf(-1,gof.dfe);
        temp=confint(f, level);
        z=coeffvalues(f);


        fplot(f, [0 140])
        plot(xTemp, yTemp,'b.','MarkerSize',5)
        objective = @(x) f(x) - ytocut;

        result(i, 3)=fzero(objective, xTemp(len));
        result(i, 5)=gof.rsquare;

        result(i, 1)=i;
        result(i, 5)=gof.rsquare;

        objective = @(x) temp(1,1)*exp(temp(1,2)*(x))+ temp(1,3)*exp(temp(1,4)*(x)) - yto-
cut; result(i, 2)=fzero(objective, xTemp(len));

        objective = @(x) temp(2,1)*exp(temp(2,2)*(x))+ temp(2,3)*exp(temp(2,4)*(x)) - yto-
cut; result(i, 4)=fzero(objective, xTemp(len));

        result(i,6)=result(i,2)-result(i,4);

        fplot(@(x) temp(1,1)*exp(temp(1,2)*(x))+temp(1,3)*exp(temp(1,4)*(x)),[0 140])

        children = get(gca, 'children');
        children(4).Color= lr;
        children(2).Color= lo;
        children(2).LineStyle= '–';
        children(1).Color= lo;
```

```
        children(1).LineStyle= '–';

        inter=predint(f,xTemp,0.95,'functional','off');
        plot(xTemp,inter(:,1),'Color', lo ,'LineStyle','–')
        plot(xTemp,inter(:,2),'Color', lo ,'LineStyle','–')

end

line([0 140],[ytocut ytocut],'Color','red','LineStyle','–')
```

B. *Post mortem* analysis results

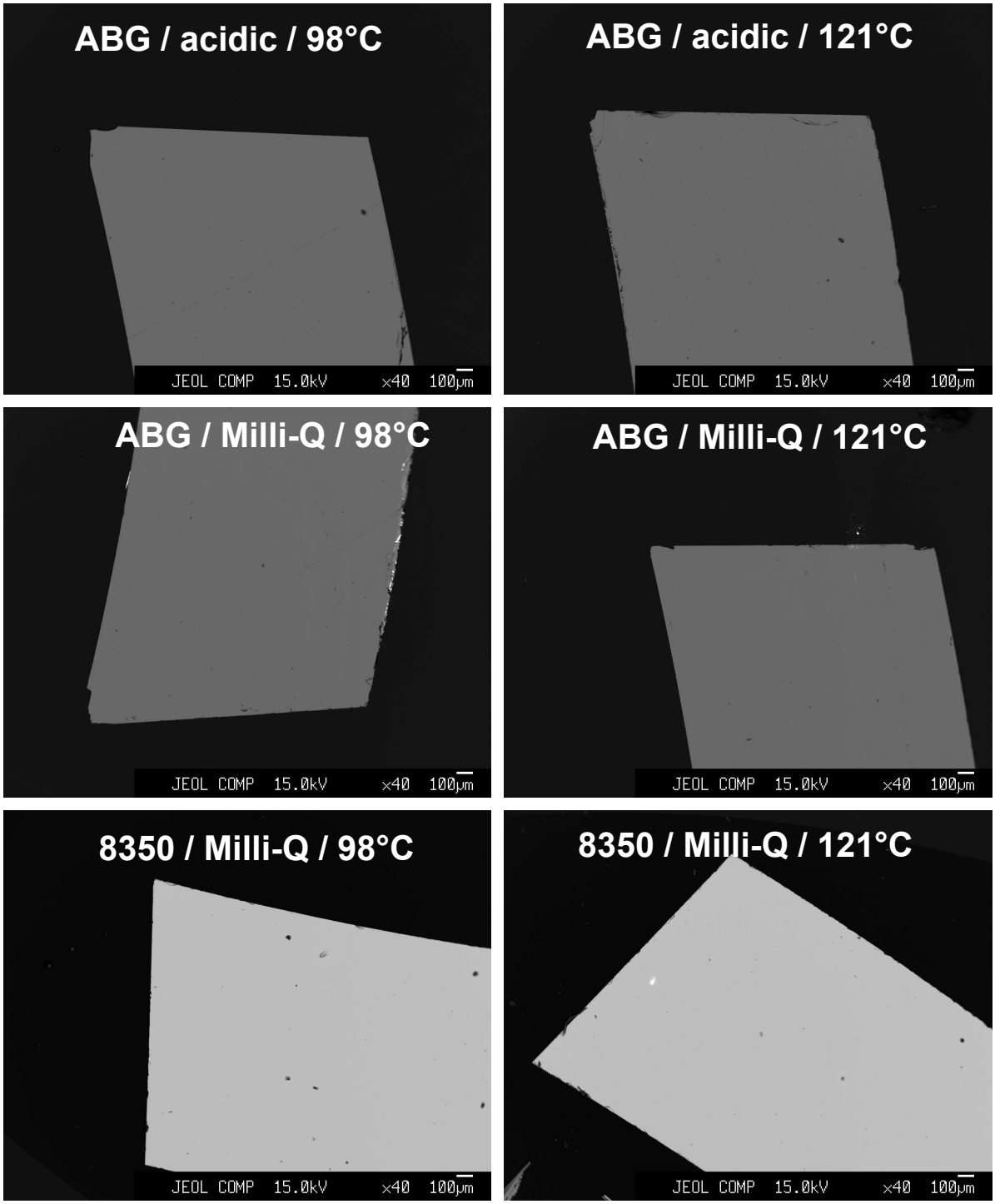

Fig. B.1.: BSE images of corroded industrial glasses. Glass tube segments of AR-GLAS®(8350) and ABG were corroded in acidic (concentrated HCl) solution and Milli-Q®. The respective solution and All samples were corroded for 28 days, the other information is given in the images. It is evident, that no considerable corrosion zone has formed.

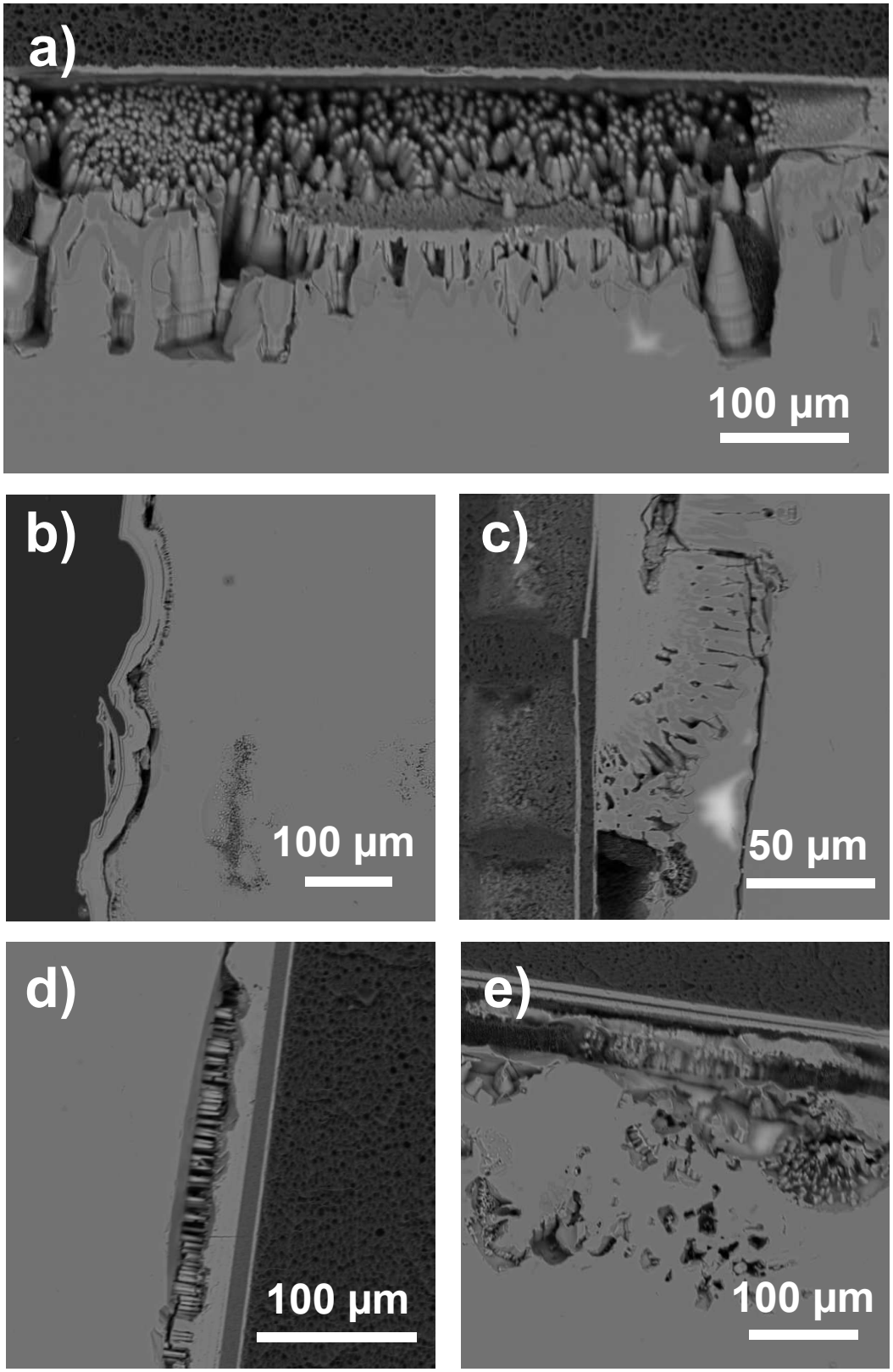

Fig. B.2.: EMP analysis of Milli-Q® batch experiments. **(a,b)** TBG samples corroded for days 21 at 121°C and **(c)** 35 days at 98°C. AR-GLAS® corroded for 21 days at 98°C **(d)** and 121°C **(e)**. Stalagmite or pillar-shaped structures have been observed at the dried samples. It remains open whether or not these structures are build up during the experiment or are a result of the drying process.

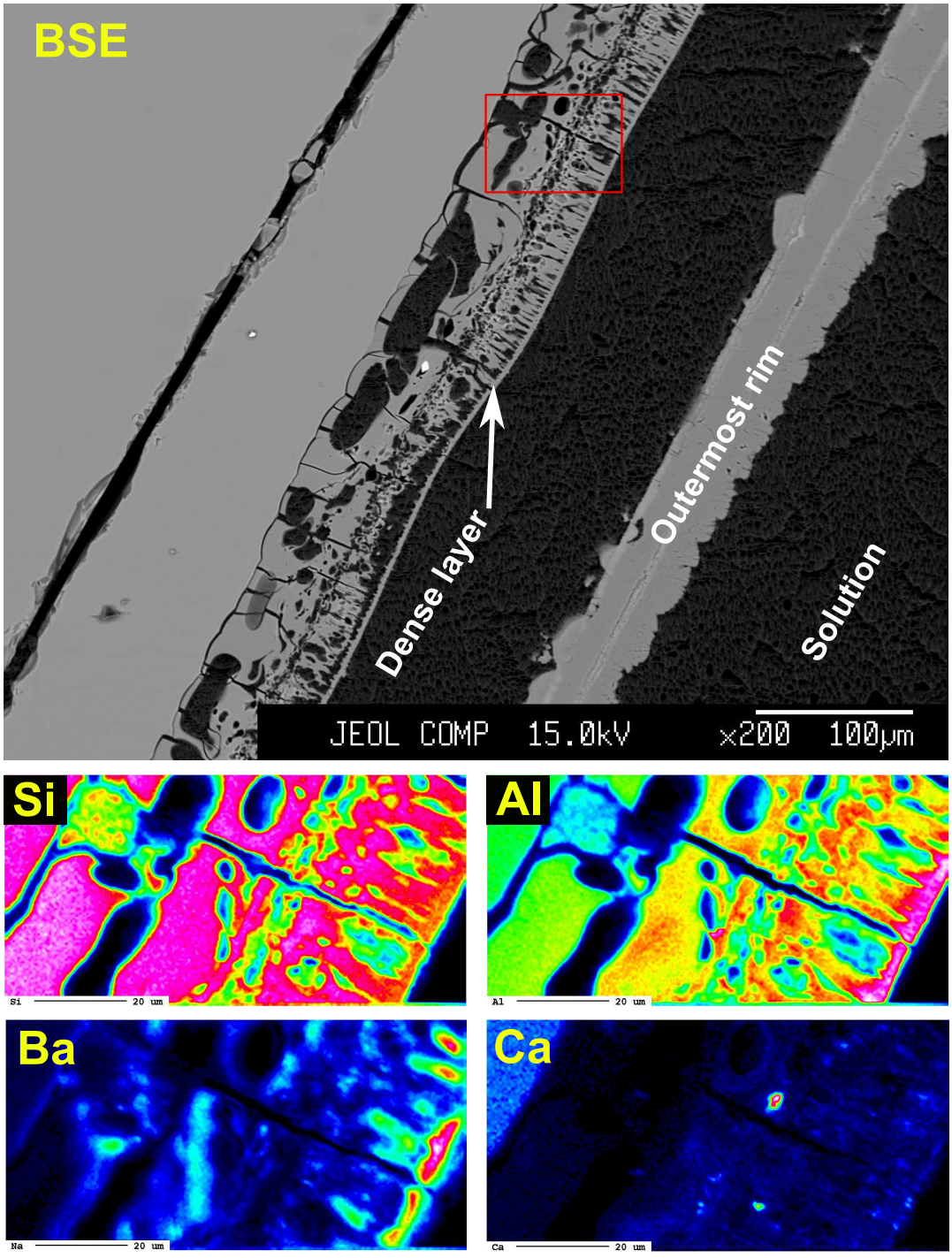

Fig. B.3.: EMP analysis of a ABG sample corroded in basic solution for 4 weeks at 121°C. Qualitative chemical distribution maps along with a BSE image are displayed. In contact with the glass, divided by a small gap, a plain corrosion zone is visible. This zone depleted with respect to calcium and barium, whereas silicon and aluminum are still present. It is followed by the palisade-shaped structure and a thin dense rim, which barium is strongly enriched.

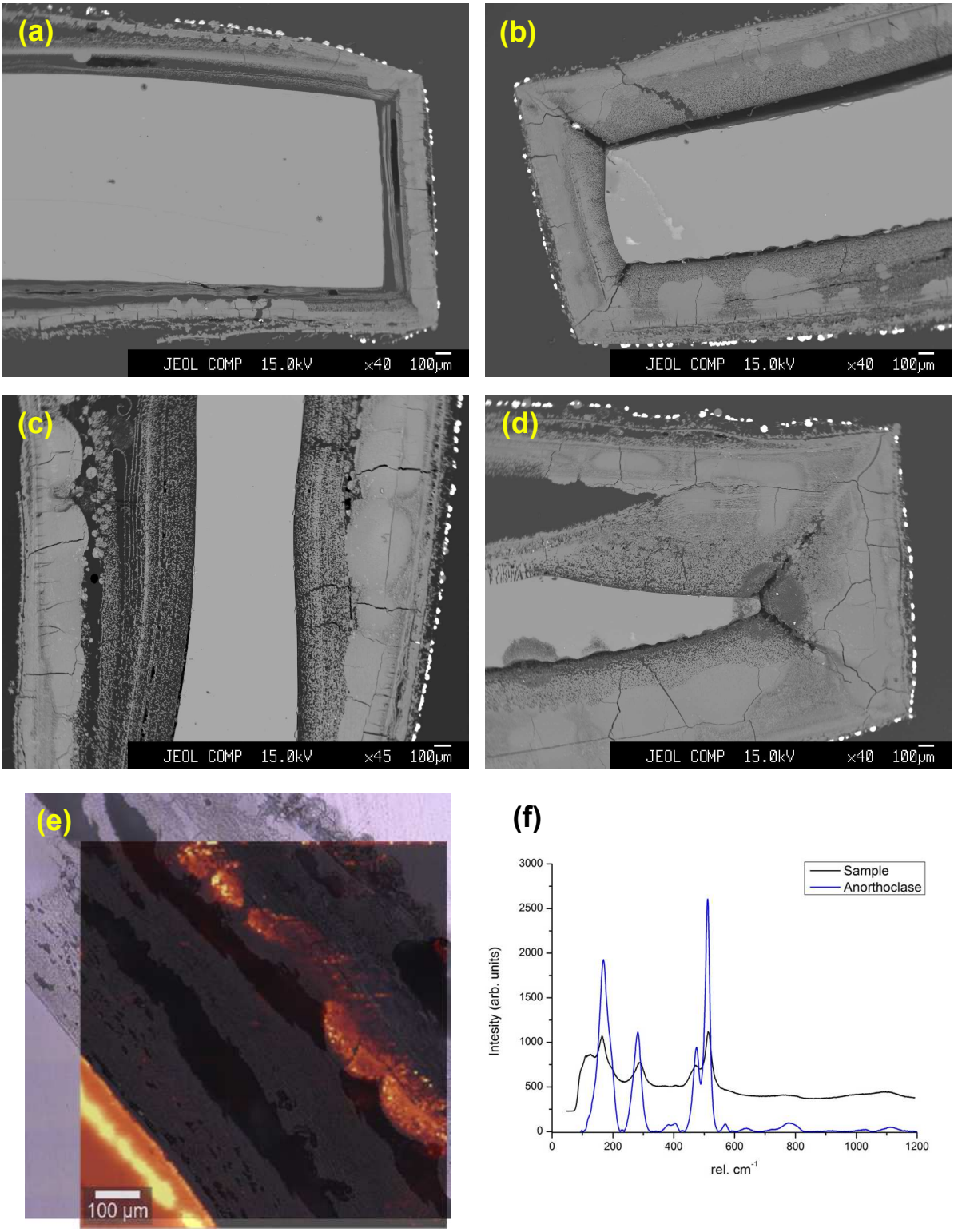

Fig. B.4.: BSE images and Raman results of AR-GLAS® corroded in alkaline solution (cf. Method section) at 98°C. The samples experiments lasted for 14 **(a)**, 21 **(b)**, 28 **(c)** and 35 days **(d)**. The light microscopic image of the sample corroded for 28 days **(e)** is superimposed with the Raman intensity distribution map of the integrated anorthoclase main band at ∼500 cm^{-1}. A representative spectrum is shown in (f) along with a reference spectrum.